

CATALYSIS: ELUCIDATING KINETICS AND TRENDS USING DFT AND
EXPERIMENTS

By

STEVEN V. NYSTROM

A DISSERTATION PRESENTED TO THE GRADUATE SCHOOL
OF THE UNIVERSITY OF FLORIDA IN PARTIAL FULFILLMENT
OF THE REQUIREMENTS FOR THE DEGREE OF
DOCTOR OF PHILOSOPHY

UNIVERSITY OF FLORIDA

2020

© 2020 Steven V. Nystrom

I dedicate this dissertation to my mom in honor of all the hard work and time she spent raising me, and to Tiffany for always being there for me.

ACKNOWLEDGMENTS

I would like to thank my advisor, Dr. David Hibbitts, for his insights and guidance through my PhD studies. Furthermore, I would like to graciously acknowledge helpful discussions with my fellow lab PhD lab mates, Abdulrahman Almithn, Alex Hoffman, Pavlo Kravchenko, and Mykela DeLuca, as well as the others who assisted in lab work, Mariya Kulagina, and Manish Godara. I am also grateful for the GSF fellowship and the NSF GOALI grant for funding (AWD04912), and for computational resources provided by XSEDE Science Gateways program (CTS160041) and from University of Florida Research Computing.

TABLE OF CONTENTS

	<u>page</u>
ACKNOWLEDGMENTS.....	4
LIST OF TABLES.....	7
LIST OF FIGURES.....	8
LIST OF ABBREVIATIONS.....	11
ABSTRACT	12
CHAPTER	
1 INTRODUCTION TO CATALYSIS.....	14
2 TUNING BRØNSTED ACID STRENGTH BY ALTERING SITE PROXIMITY AND INVESTIGATING METHANOL DEHYDRATION IN CHA FRAMEWORKS....	17
Introduction	18
Acid Strength.....	18
Reactivity.....	24
Computational Methods and the Artifacts of Periodic Charged Calculations	30
Results & Discussion	39
Predicting the Acid Strength of Isolated Acid Sites in CHA	39
Effects of Acid Site Proximity on Acid Strength	45
The Sphere of Influence of Acid Sites	61
Proximity of Sites with Varying Si:Al Ratio.....	64
Altering the State of Proximal Acid Sites	66
Inhibition of Methanol Dehydration Rates on Small-Pore Zeolites.....	72
DFT Assessments of Prevalent Methanol Dehydration Reaction Pathways	76
Conclusion	82
3 ReO _x PROMOTIONAL EFFECTS ON BIMETALLIC CATALYSTS FOR THE PURPOSE OF HYDROGOENOLYSIS.....	85
Introduction	86
Methods	92
Catalyst Synthesis.....	92
Pt / C	92
Pt - ReO _x / C	93
Au / CeO ₂	93
Au - Re / CeO ₂	94
Reactions	95
Parr 300 mL reactions.....	95
Parr 50 mL reactions.....	97

Continuous flow reactor	98
Characterization and Analysis	99
H ₂ chemisorption.....	99
HPLC analysis	100
GC-MS analysis	100
GC analysis.....	102
Results and Discussion.....	103
Catalyst Characterization – H ₂ Chemisorption	103
Glycerol Hydrogenolysis.....	103
Effects of ReOx promotion on hydrogenolysis catalysts (Pt)	103
Effects of ReOx promotion on poor hydrogenation catalysts (Au).....	109
Ethanol Hydrogenolysis.....	109
Effects of ReOx promotion on hydrogenolysis catalysts (Pt)	109
Effects of ReOx promotion on poor hydrogenation catalysts (Au).....	111
Continuous flow reactor, ethanol (g) reagent	112
Water phase effects on alcohol conversion	113
Conclusion.....	114
Future Works	115
4 NO_x REDUCTION USING ATOMICALLY DISPERSED RHODIUM ON OXIDE SURFACES FOR POTENTIAL AUTOMOTIVE CATALYTIC CONVENTER APPLICATIONS.....	117
Introduction	117
Methods	119
Results & Discussion	121
Surface Formation Energies.....	121
CO and NO Adsorption Energies	122
CO and NO Exchange Energies.....	125
Frequencies.....	127
Conclusion	128
Future Works	128
Reactions	128
Hydroxyl Groups.....	128
Defect and Step Edge Sites	129
APPENDIX	
A SUPPORTING INFORMATION FOR CHAPTER 2	130
B SUPPORTING INFORMATION FOR CHAPTER 3	141
C SUPPORTING INFORMATION FOR CHAPTER 4	143
LIST OF REFERENCES	145
BIOGRAPHICAL SKETCH.....	164

LIST OF TABLES

<u>Table</u>	<u>page</u>
2-1 Electronic energies (E_0), enthalpies (H), and free energies (G) for DPE, DHE, NH ₃ BE of isolated Brønsted acids in CHA.....	42
2-2 Acid sites can be weakened, unaffected, or strengthened when a seond site is placed in varying positions as a bare proton or with NH ₃ adsorbed.	72
3-1 The four catalysts of interest with their metal loading content and uncertainties. The strong isotherm of H ₂ chemisorption was used to find H ₂ uptake, dispersion (assuming 2:1 adsorption per site), and particle size.....	103
3-2 Selectivities and initial rates at 10% conversion for glycerol (1 wt. %) hydrogenolysis on Pt/C with 2 replicates as well as glycerol (aq.) alone in the reactor and with the carbon Norit support.....	106
3-3 Selectivities and initial rates at 10% conversion for glycerol (1 wt. %) hydrogenolysis on PtReO _x /C with 2 replicates.	107
4-1 Surface formation energies (in kJ mol ⁻¹ Å ⁻¹) for the following facets and terminations for the four oxides that converged.....	122
4-2 The binding energies exchange energies/ enthalpies (kJ mol ⁻¹) for CO and NO adsorbed on a Rh surface at 573 K and 1 bar.....	126
4-3 The vibrational frequencies for the various vibration on Al ₂ O ₃ (010)	127

LIST OF FIGURES

<u>Figure</u>	<u>page</u>
1-1 The zeolite chabazite with a single Al heteroatom replacement creating a Brønsted acid site.....	15
2-1 Structures of intermediates and transition states (marked as #) for the associative (top path) and dissociative (bottom path) mechanisms of Brønsted acid-catalyzed methanol dehydration to DME.....	27
2-2 The CHA framework.....	34
2-3 Ring structures and angles for CHA.....	36
2-4 The correlation between supercell size and DPE	39
2-5 The most stable orientation of the proton..	41
2-6 The relationship between energies for isolated acid sites.	43
2-7 The most stable orientations of adsorbed NH ₃ on the isolated site..	45
2-8 Most and least stable proton locations in the CHA framework.	47
2-9 Relative E_0 for protons on the four O atoms of isolated sites and the sixteen arrangements of protons for all 23 site-pairs..	48
2-10 Arithmetic averages for all states averaged across the 23 site-pairs.....	49
2-11 The DPE in kJ mol ⁻¹ for the isolated acid site and all site-pairs where the second site is protonated.....	51
2-12 Proton positions for paired acid site and their conjugate bases.....	52
2-13 The most stable conjugate bases for site-pairs.	54
2-14 A diagram illustrating the effect of relative framework location on ensemble DPE values for site pairs.	55
2-15 Ensemble average DPE in kJ mol ⁻¹ as a function of the ensemble average distance in Å between the H of the second site and the nearest O of the deprotonated A site.	56
2-16 The relationship between energies.....	58
2-17 The adsorbed ammonia various sites.....	60

2-18	Ensemble average values for energies as a function of the distance between Al T-sites in the CHA supercell.....	63
2-19	Fraction of sites at a variety of Si:Al ratios with random Al distribution in CHA with nearest Al between 3 and 16 Å away.....	65
2-20	The relationship between DPE when the second site is protonated (HZ) or when ammonia has adsorbed onto the second site (NH ₄ Z).....	69
2-21	The anions of the site-pairs with NH ₃ adsorbed to the second site.....	69
2-22	Experimental and theoretical methanol dehydration rates.....	74
2-23	Fractional methanol conversion (415 K) on a H-CHA	77
2-24	Reaction coordinate diagram showing DFT-calculated free energies.....	78
2-25	The most favorable transition state found in CHA.	79
2-26	DFT-predicted rates.....	82
3-1	Transesterification of triglycerides in the presence of methanol to form methyl esters and glycerol	88
3-2	Proposed transition state for a single step conversion from glycerol	90
3-3	Proposed mechanism for the formation of 1,3-PDO resulting from the hydrogenolysis of glycerol	91
3-4	The schematic drawing of the reactor, with all relevant parts labeled.....	96
2-3	The flow and instrumentation setup for the packed bed flow reactor.....	99
3-6	Concentration of glycerol as a function of time on a Pt catalyst. The horizontal dotted line is 10% conversion based on the reagent depletion, the vertical dotted line is the time for 10% conversion, the solid line are guidelines through the data points, and the yellow line is the slope/rate.	105
3-7	Selectivity as a function of conversion.....	105
3-8	Reaction scheme for glycerol hydrogenolysis, comparing the rates and selectivities at 10% conversion for the 3 catalyst Pt, PtReO _x , and AuReO _x	108
3-9	Reaction scheme for ethanol, comparing the rates and selectivities at 10% conversion for the three catalysts: Pt, PtReO _x , and AuReO _x , in the liquid phase and the gas phase	112
4-1	The structures and energies for Rh	124

4-2	The spread of electronic (E_0) and free energies (G) as well as enthalpy (H) for CO binding energy	125
4-3	The unique NO binding configurations with their relative E_0 , Gibbs free energy calculated in kJ mol^{-1} at 573 K and 1 bar.	125
4-4	The binding energies and the exchange correlation energies for CO and NO with the structure of the most stable state presented.	126

LIST OF ABBREVIATIONS

12PD	1,2-Propanediol
13PD	1,3-Propanediol
1Pro	1-Propanol
2Pro	2-Propanol
CHA	The Chabazite zeolite
DFT	Density Functional Theory
DHE	Dehydrogenation Energy
DME	Dimethyl ether
DPE	Deprotonation Energy
EG	Ethylene Glycol
G	Gibbs free energy
Gly	Glycerol
H	Enthalpy
MR	Member-ring
MTH	Methanol to Hydrocarbons
MTO	Methanol to Olefins
NH ₃ BE	Ammonia Binding Energy
POM	Polyoxometalates
T-site	Tetrahedral site
TWC	Three-way catalyst

Abstract of Dissertation Presented to the Graduate School
of the University of Florida in Partial Fulfillment of the
Requirements for the Degree of Doctor of Philosophy

CATALYSIS: ELUCIDATING KINETICS AND TRENDS USING DFT AND
EXPERIMENTS

By

Steven Nystrom

May 2020

Chair: David Hibbitts
Major: Chemical Engineering

This study examines three main topics; the effect that proximal acid sites in chabazite (CHA) have on acid strength and kinetics, the effects of ReO_x promotion on precious metal catalysts, and the efficacy of single metal atoms (Rh) in automotive catalytic converters. First, we show that Brønsted acid strengths—as predicted by dispersion-corrected periodic density functional theory (DFT) calculations of deprotonation energy (DPE), dehydrogenation energy (DHE), and NH_3 binding energy (NH_3 BE)—are affected by site proximity in proton-form zeolites and that adsorbates on one acid site alter the strength of nearby acids. Placing a second acid in the 6MR of CHA decreased DPE and NH_3 BE values for the first site by $> 10 \text{ kJ mol}^{-1}$ but acid site pairs across 8MR structures interact very little when the second acid is bare as residual protons cannot stabilize a conjugate base across such large distances.

Transitioning to Brønsted acids on metal surfaces using glycerol and ethanol as reagents, Pt (5 wt. %) and Pt- ReO_x (5 wt. % of both metals) were impregnated on activated carbon (Norit SG-1), additionally, Au (1 wt. %) and Au- ReO_x (1 wt. %, 0.3 wt. %) were prepared on CeO_2 supports. Aqueous phase reactions are carried out in a batch reactor (1 wt. % alcohol, 473 K, 4.0 MPa H_2). For glycerol reactions on Pt-based

systems, the ReO_x promoter increased rates by a factor of ~20 (normalized by Pt-surface atoms). These selectivity and rate shifts indicate that ReO_x facilitates C–O activation and enables C–O activation at secondary positions of the C_3 backbone while decreasing C–C cleavage. The AuReO_x increased rate reactions by a factor of 2 but created unsaturated compounds. Lastly, DFT is used to elucidate how atomically dispersed metals such as Rh on Al_2O_3 , TiO_2 , and CeO_2 effect the NO_x reduction and CO oxidation. NO binds (-327 kJ mol^{-1}) stronger than CO (-240 kJ mol^{-1}) to Rh and the exchange energies to go from NO–Rh–CO to NO–Rh–NO are negligible (-5 kJ mol^{-1}).

CHAPTER 1

INTRODUCTION TO CATALYSIS

The increased demand of energy for both transportation, residential, and commercial use is being facilitated by a growing population especially as large nations, like India and China, become modernized, using dramatically more energy. India is expecting to use 106 megawatts of energy by 2030, and China is predicted to require about the same.¹ Increases in CO₂ emissions, as well as other greenhouse gases like methane from fracking, and various emissions are accelerating climate change. Climate change is and will continue to have devastating results on the planet.^{1–3} Fortunately, many people and scientific communities see this imminent threat and are working on novel ways to combat this issue. In particular, the fields of catalysis and biomass conversion may be able to aid us in getting to a more carbon neutral energy system and eventually become carbon negative.

Catalysis has been revolutionizing approaches to many societal problems for over a century; for example, the Haber-Bosch process allowed industrial-scale nitrogen fixation for products like fertilizers and explosives.⁴ The Fischer-Tropsch process was discovered in Germany in 1925 by flowing syngas over an Fe/Co catalyst to create fuel.⁵ Catalysis makes many of the plastics, products, and energy from fossil fuels through coal gasification and cracking crude oil.

Upgrading species with a low number of carbon atoms, such as methanol, to various products with higher carbon content, like ethylene via methanol-to-olefins (MTO) routes or octane via methanol-to-gasoline (MTG) routes is becoming more necessary as societal environmental pressures mount.^{6–8} Brønsted acid sites can facilitate these various methanol-to-hydrocarbon (MTH) reactions such MTO and MTG, and more

specifically Brønsted acids in structures like zeolites, polyoxometalate clusters (POMs) or even acid-promoted metal catalysts.^{9–12} The confining voids of zeolites accelerate reactions by stabilizing reactive intermediates and transition states through dispersive and H-bonding interactions.^{13–16} Furthermore, zeolites can replace some of their Si for metals creating acid sites, more specifically CHA can facilitate Al in its framework creating Brønsted acid sites which help in the C–O chemistry. Methanol dehydration—converting two methanols into dimethyl ether and water—is a great probe reaction in DFT which allows C–O bond activation to be studied on alcohols without the configurational intensity of larger alcohol species. The proximity of the acid sites effects the acid strength, thus the rates of reactions and prevailing mechanisms, as sites become closer to a ‘paired’ configuration the rates increase in small pore zeolites.^{17–20}

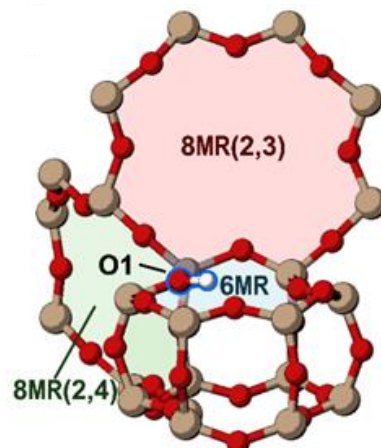


Figure 1-1. The zeolite chabazite with a single Al heteroatom replacement creating a Brønsted acid site. Adapted with permissions from²¹

Brønsted acids can also form on metal surfaces and not just in zeolites; ReO_x promoted metals have also been shown to act as Brønsted acids.^{22–25} Hydrogenolysis—using hydrogen to cleave C–C and C–O bonds—is a promising reaction to obtain higher market value products. Biomass conversion entails a large range of concepts from burning, to gasification, to cleaving hydrocarbon off fats; however, overall they

contain oxygenated species, requiring knowledge of C–O and C–C bond cleavages to upgrade these species to fuel, commodity products like plastics, or could be stored underground.^{1,26–29}

Emissions for industry and vehicles can be altered by metal supported catalysts to reduce emissions from gas powered engines, converting the outlet gas stream consisting of CO, NO_x, C_xH_y, etc. to mostly CO₂, N₂, and H₂O, such as in the 3-way automotive catalytic converter. Although the 3-way catalytic converter has been optimized throughout the years, it still suffers from performance issues at start up when the temperatures are not high enough to start the reactions.^{30,31} Novel single metal atom catalysts may be able to assist in the NO_x reduction and CO oxidation at these conditions while simultaneously requiring less metal to be used in the catalytic converter.^{32–36}

Here, we explore the CHA zeolite using DFT to elucidate how paired acid sites affect parameters such as acid strength, reaction barriers, and inhibition in the methanol dehydration reaction. We then look at Brønsted acids on metal surfaces experimentally demonstrating ReO_x ‘s and waters’ promotional effect on Pt and Au catalysts for the reactions of polyols. Lastly, DFT will be used to reveal how NO_x reduction and CO oxidation occur on atomically dispersed Rh on γ-Al₂O₃, TiO₂ (anatase and rutile), and CeO₂ surfaces.

CHAPTER 2

TUNING BRØNSTED ACID STRENGTH BY ALTERING SITE PROXIMITY AND
INVESTIGATING METHANOL DEHYDRATION IN CHA FRAMEWORKS

(Reprinted (adapted) with permission from:

Mechanistic origins of the high-pressure inhibition of methanol dehydration rates in small-pore acidic zeolites, J. of Cat., V380, Dec '19, Pg. 161; and

Tuning Brønsted Acid Strength by Altering Site Proximity in CHA Framework Zeolites, ACS Cat., 2018, 8, 9, 7842-7860, Copyright 2019 ACS)

This study examines how Brønsted acid strengths—as predicted by dispersion-corrected periodic DFT calculations of deprotonation energy (DPE), dehydrogenation energy (DHE), and NH₃ binding energy (NH₃ BE)—are affected by site proximity in proton-form zeolites and how adsorbates on one acid site alter the strength of nearby acids. Protons can bind to four distinct O atoms around the single crystallographically-unique T-site of CHA and all such locations were examined as bare and NH₃-occupied sites. Protons prefer to bind to O1 atoms and orient within the plane of six-member ring (6MR) structures of CHA. NH₄⁺ cations show a strong preference for binding in 8MR windows; 6MR structures are too small to solvate them. These preferences govern proximity effects on acid strength, studied here by probing the strength of a Brønsted acid site while a second site is placed in 23 locations separated by 1–3 T-sites. Placing a second acid in the 6MR of CHA decreased DPE and NH₃ BE values for the first site by > 10 kJ mol⁻¹ because the proton of the second site stabilized the deprotonated site across the 6MR. Acid site pairs across 8MR structures interact very little when the second acid is bare as residual protons do not prefer to orient within 8MR. One location of the second acid stabilized the adsorbed proton without stabilizing the deprotonated state, resulting in a significantly weaker acid. All these effects are altered when the second site is instead occupied by an adsorbed NH₃, which acts as a proxy for strongly-bound reactive intermediates and cationic transition states. The strength of the first site

is significantly weakened (DPE and NH₃ BE increases of > 20 kJ mol⁻¹) when a second site is NH₃-occupied and placed in the 6MR because such structures are too small to effectively solvate NH₄⁺ cations. Acid sites are strengthened, however, when second sites are NH₃-occupied and placed across 8MR windows, because they are appropriately-sized to solvate the NH₄⁺ cations that simultaneously interact with both deprotonated sites. The alteration of acid strength by acid site proximity therefore depends on their specific arrangement (not merely Al–Al distances), the structural motifs present (such as 6MR structures which allow protons, but not NH₄⁺, to stabilize proximal conjugate base anions), and whether proximal sites are vacant or occupied, which determines the distances over which cationic-anionic stabilizations of deprotonated sites can take place. Lastly, turnover rates of Brønsted acid-catalyzed methanol dehydration to dimethyl ether become inhibited at high methanol pressures (>10 kPa, 415 K) on small-pore zeolites (CHA, AEI, LTA, LEV), irrespective of the distribution of framework Al and their attendant H⁺ sites, but not on medium-pore or large-pore zeolites. High pressure kinetic inhibition occurs concomitantly with the stabilization of higher-order methanol clusters (e.g., trimers, tetramers) verified by experimental and DFT studies. This combined experimental and theoretical investigation provides precise mechanistic interpretation of the high-pressure inhibition of methanol dehydration turnover rates on small-pore Brønsted acid zeolites.

Introduction

Acid Strength

Zeolites play a pivotal role in many industrially and academically relevant chemical processes,³⁷ such as catalytic cracking in the petrochemical industry,³⁸ methanol-to-hydrocarbons (MTH),^{6–8} and separations processes.^{39–41} Zeolites are

microporous, crystalline aluminosilicates; over 200 frameworks have been synthesized^{42–44} and another 350,000 frameworks have been theorized with formation energies within 30 kJ mol⁻¹ of α -quartz, indicating stabilities within the range of synthesized materials.^{45,46} The micropores which traverse zeolite crystals create diverse environments of varying void dimensions that impact reactivity and selectivity through size-exclusion of reagents and transition states and differently confine and solvate reagents and transition states within the voids through non-covalent interactions.^{14,17,47–}

⁴⁹ Trivalent heteroatoms (Al^{3+} , Ga^{3+} , Fe^{3+} , B^{3+}) may substitute Si^{4+} at tetrahedral sites (T-sites) within the framework and create a net anionic charge that can be balanced by protons (H^+) located on adjacent O atoms, forming Brønsted acid sites. The energy required to fully separate the proton and form an anionic conjugate base is the deprotonation energy (DPE), a theoretical metric of the strength of an acid. Acid-catalyzed reactions typically result in charge separation of the acid site are therefore dependent on the DPE (acid strength) for reactions catalyzed by proton-form zeolites^{16,47,50} and other well-defined solid-acid catalysts like polyoxometalates (POM)^{51–}

⁵⁴ or even acid-promoted metal catalysts.^{22,25,55–58}

DPE is strongly influenced by the identity of the heteroatom in zeolite materials,^{47,59} while the topology of the surrounding framework is believed to weakly effect DPE,¹⁶ indicating that the observed effects of zeolite frameworks on reaction rates and selectivities are a consequence of their distinct local topographical environments rather than their acid strength—a subject of continued debate.^{13,14,17,48,49,60–65} It was demonstrated on the zeolites MFI, BEA, FER, MOR, CHA, and FAU that after accounting for DFT charge artifacts (discussed later) and after

normalization, DPEs are largely independent of local topology. For instance, when ensemble averaging the DPEs (discussed further in the Methods section) across the various zeolites and comparing those values against their Al framework density. DPE is largely independent of topology and the difference in acid strength in the various zeolites can be attributed to the Al framework density.^{13,47}

The special density of Brønsted acid sites within aluminosilicate zeolites depends on the Si:Al ratio and the density of tetrahedral sites (framework density), and as the Brønsted acid site density increases, sites may be formed within close proximity to one another. New synthesis techniques are aimed at controlling the relative location and proximity of Brønsted acid sites within zeolite framework.^{19,20,66–70} The difference in acid strength and catalytic behavior between isolated acid sites and proximal sites is controversial, and these distinctions have been hampered by the inability to separate effects of bulk composition (Si:Al ratios) from the arrangement of Al sites in isolated or proximal configurations. Recently, synthesis and characterization techniques have been developed for many zeolites, including H-SSZ-13 (CHA framework), that control the fraction of Al sites within close proximity to one another by varying the ratio of two structure directing agents (N,N,N-trimethyl-1-adamantylammonium and Na⁺) without changing the Si:Al ratio.^{19,66,71,72} These ‘paired’ sites can then be counted using Co²⁺ titration methods that detect pairs of Al atoms within the same 6-member ring (6MR) of the CHA framework arranged in Al—O—(Si—O)_x—Al configurations with 1–2 linking Si atoms ($x = 1,2$).⁶⁶ The arrangement of paired Al within 6MR structures of H-SSZ-13 is critical in the NO_x reduction on Cu-exchanged materials.^{73–76} Synthesis techniques which vary Al distribution at constant Si:Al ratios and titrations which can count the

number of paired sites enable kinetic measurements to determine the effects of Al site pairing on chemical reactions.

Rates of reactions often correlate strongly with DPE,^{16,22,47,48,50} which is a purely theoretical assessment of acid strength given by calculating the reaction energy of heterolytically cleaving the O–H bond of the Brønsted acid:



where Z is the zeolite framework providing an O atom as the point-of-attachment for the proton and the energy of the anionic conjugate base (Z^-) is therefore required; periodic boundary conditions in density functional theory (DFT) result in dipole-dipole interactions between neighboring unit cells, which are exacerbated in charged calculations as these have large dipole moments between the location of the anion and the uniform compensating background charge.⁷⁷ To overcome these issues, prior work has examined non-periodic cluster models of zeolites,^{59,78–80} which do not suffer from dipole-dipole interactions between neighboring unit cells, but may not capture the effects of the framework. Similarly, hybrid methods coupling quantum and molecular mechanics (QM-MM) models use QM methods on a small active site regime and MM methods on the surrounding framework.^{81–85} Recent work has calculated DPE for isolated acid sites in 6 zeolite frameworks using fully periodic DFT methods and that work attempts to correct for periodic charge artifacts by recognizing a near-linear dependence between the DFT-calculated DPE values and the framework density of the framework, indicating that the charge artifacts may involve the framework density or perhaps—more simply—the size of the unit cell.¹⁶ Previous work has noted that protons on proximal acid sites in an Al-rich framework can form intraframework H-bonds, which

stabilize the Brønsted sites, or protons can destabilize one another via unfavorable electronic interactions, decreasing DPE.⁸⁶ Here, we will examine the effects of unit cell size and anion position on artifacts created by charged calculations in periodic DFT and demonstrate that the spatial density of the anion must be kept constant when comparing DPE values. In cases where it cannot be kept constant (comparing DPE across multiple frameworks), the anion density can be used as a more accurate correction factor than the framework density previously applied.¹⁶

To mitigate flaws inherent in charged periodic calculations, dehydrogenation energy (DHE) can be calculated in conjunction with DPE, which is the energy to homolytically cleave the O–H bond. DHE in this instance is the same as the bond dissociation energy (BDE):



The difference in energy between the DPE and DHE is the sum of the ionization energy of a H atom ($\text{H}\cdot \rightarrow \text{H}^+ + \text{e}^-$) and the electron affinity (EA) of zeolite framework ($\text{Z}\cdot + \text{e}^- \rightarrow \text{Z}^-$), which may depend on the local framework topology and composition (i.e., presence of another nearby Brønsted acid site).

Finally, acid strength can also be probed by the adsorption of a base, such as ammonia (NH_3), both experimentally and theoretically.^{76,82,87–90} Theoretical base adsorption analysis is beneficial because charged calculations are avoided (like DHE and unlike DPE) while the O–H bond is heterolytically cleaved (like DPE and unlike DHE). However, the binding energy resulting from NH_3 adsorption and subsequent formation of NH_4^+ (NH_3 BE) will also be influenced by the surrounding cage topology through dispersive and H-bonding interactions;^{87,89,91–93} therefore, NH_3 BE is not a

“pure” metric of acid strength, but measures a mixture of acid strength and confinement effects. For this reason, NH₃ TPD studies which aim to discriminate shifts in acid strength by shifts in desorption temperatures will give convoluted results.^{1,19,66} Because NH₃ BE is influenced by the surrounding framework, however, it more accurately reflects the chemical behavior of reacting species, as shown in previous work for Brønsted acid-catalyzed reactions.²² Concurrent analysis of DPE, DHE, and NH₃ BE on H-form zeolites allows for a thorough description of the strength of Brønsted acids in these frameworks. Although Lewis acidity is applicable for some zeolites, Al substituted CHA only acts as a Brønsted acid.

Here, we investigate acid strength in H-form CHA (H-SSZ-13) using DPE, DHE, and NH₃ BE using fully periodic DFT models for isolated Brønsted sites—with one acid site per unit cell—and for unit cells with multiple acid sites in 23 arrangements covering a wide range of Al–Al distances. For these configurations with multiple acid sites, we calculate the DPE, DHE, and NH₃ BE of an acid site while varying the location of a ‘second’ site in the multi-site configuration. We also examine the effects of coverage by recalculating DPE, DHE, and NH₃ BE for all Al-site arrangements while the second acid site is occupied by NH₃. Our results indicate that acid sites noticeably interact with one another at distances < 9 Å (up to ~3 linking Si T-sites away), and that within these distances, proximal acid sites may be stronger or weaker acids than isolated sites (evidenced by DPE, DHE, and NH₃ BE), depending on the exact arrangement of atoms. Critically, the ‘paired’ sites within the 6MRs are stronger acids than isolated sites because the proton on the second acid site H-bonds with the conjugate base formed upon deprotonation of the first site and these are the same ‘paired’ sites that dehydrate

methanol at faster rates in CHA;¹⁹ their enhanced acid strength provides a possible explanation for the observed rate enhancement. Acids are weakened by a second site when together they occupy nearby positions in the framework but the proton on a second site cannot stabilize the conjugate base of a deprotonated site. The coverage of these sites also impacts their acid strength, as enhancement in acid strength is greatest when the second acid site is a bare proton (and thus capable of H-bonding with the conjugate base of the first acid site), while the acid strength changes if the second acid site is occupied by an adsorbate, as they often are during catalytic reactions. This study therefore establishes the guiding principles necessary to tune acid strength through the formation of AI arrangements within interacting distances and can be used to guide the synthesis of such materials in CHA and other zeolite frameworks.

Reactivity

It has been stated several times now that reaction rates are influenced by acid strength and that the local topology does not influence DPE; however, the local topology plays a significant role in the formation and selectivity of species in a variety of other reactions. The product selectivity of MTO can be altered by manipulating the reaction conditions (e.g., temperature, methanol pressure)⁹⁴, but also through judicious choice of the zeolite framework.^{94,95} Olefin selectivity is sensitive to the size of the confining environment; thus, zeolites containing larger cage-defining rings show increased selectivity to larger olefins.⁹⁶ Similarly, zeolite topology affects catalyst lifetime during MTO processes, and 10-membered ring (10-MR) zeolite frameworks with similar aperture sizes have lifetimes that differ by a factor of ~10.^{97,98} The conversion of methanol into olefins proceeds through a “hydrocarbon pool” mechanism, wherein methanol is hydrated at H⁺ sites to form methoxy intermediates that subsequently react

with confined polymethylated aromatics to generate new C–C bonds.^{94,95,99} Surface-bound methoxy groups ($\text{CH}_3\text{--Z}$), formed via methanol dehydration, have also been implicated in the initiation of C–C bond formation, at low turnover numbers, via carbonylation with either carbon monoxide or formaldehyde present either as impurities or formed during reaction.^{50,99,100} The dehydration of methanol to dimethyl ether (DME) also occurs selectively at low-temperatures (<453 K) without olefin formation^{14,47}, and measurement of methanol dehydration rate constants has enabled investigating the individual influences of on confinement effects and acid strength in zeolite catalysts.^{47,48,72} A probe reaction, methanol dehydration to dimethyl ether (DME) (Figure 2-1), has been examined on these materials, and the results demonstrate that paired sites in CHA have proton-normalized rate constants (first- and zero-order) that are approximately an order of magnitude larger than isolated sites.¹⁹ The exact cause of this enhancement is unknown; the second acid site in the paired configuration could *i*) alter the local confinement effects by effectively reducing the local cage diameter (particularly if that second site has an adsorbate), *ii*) stabilize cationic transition states formed at the first acid site via H-bonding (with methanol or water) or electrostatic interactions, or *iii*) alter the acid strength of the first acid site through electronic effects (electron affinity of the conjugate base) or by H-bonding with the conjugate base. Here, we will examine the influence of acid site proximity on acid strength.

In MFI, for example, zero-order and first-order kinetics for methanol to DME rate constants decreased when the DPE was increased by altering the hetero atom (Al^{3+} , Ga^{3+} , Fe^{3+} , B^{3+}). Figure 2-2 demonstrates the first order reaction rate trends inversely with DPE for both zeolite MFI and POMs. This can be attributed to the decreased

stability of the ion-pair transition states relative to their pre-cursor state as the acid strength is weakened; remembering an increase in DPE is a decrease in acid strength.⁴⁷

Low-temperature (<453 K) dehydration of methanol to DME on solid Brønsted acids can proceed via two different mechanisms, referred to as the associative (concerted) or dissociative (sequential) mechanisms (Figure 2-1).^{19,47,48,72,101} The first step in both mechanisms is quasi-equilibrated adsorption of a gas-phase methanol at a bare proton. In the associative mechanism, protonated methanol dimers form via quasi-equilibrated adsorption of a second gas-phase methanol, and then eliminate DME and water in a kinetically relevant dehydration step (Figure 2-1, top). The dissociative mechanism (Figure 2-1, bottom), in contrast, involves kinetically relevant equilibrated adsorption of a second gas-phase methanol, and then eliminate DME and water in a kinetically relevant dehydration step (Figure 2-1, top). The dissociative mechanism (Figure 2-1, bottom), in contrast, involves kinetically relevant dehydration of methanol monomers to eliminate water and form a surface-bound methoxy intermediate. Surface methoxy intermediates then undergo nucleophilic attack by a second gas-phase methanol in a quasi-equilibrated step to form DME. DME formation rates via the dissociative mechanism are thus inhibited by the formation of protonated methanol dimers⁴⁷, while methanol-water complexes can inhibit both pathways (Figure 2-1, left).

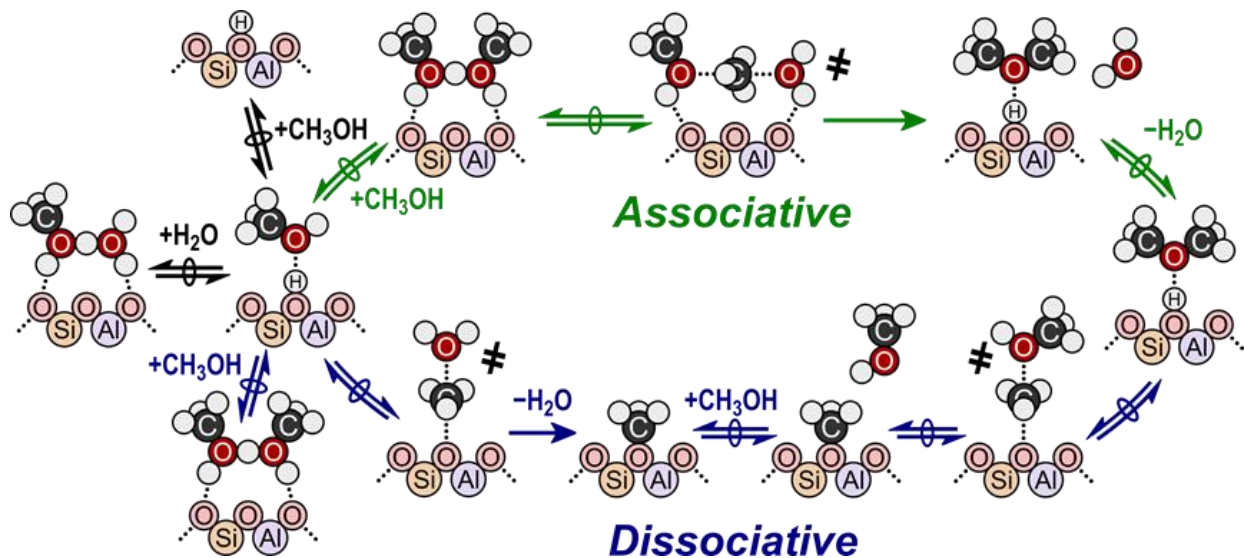


Figure 2-1. Structures of intermediates and transition states (marked as #) for the associative (top path) and dissociative (bottom path) mechanisms of Brønsted acid-catalyzed methanol dehydration to DME.

Measured reaction kinetics (433 K) and DFT calculations indicate that methanol dehydration to DME proceeds via the associative mechanism at Brønsted acid sites of POMs supported on amorphous SiO₂⁴⁷, and at such sites confined within medium-pore and large-pore zeolites (FAU, SFH, BEA, MOR, MTW, MFI, and MTT, 0.5–1.2 nm diameter voids).^{48,66,72,101} Turnover rates of methanol dehydration (433 K, per H⁺) on these catalysts follow a Langmuirian dependence on methanol partial pressure (0.05–20 kPa), transitioning from a first-order to zero-order kinetic regime at high methanol pressures. Additionally, in situ IR spectra measured on MFI zeolites (433 K, 0.1–16 kPa CH₃OH) do not show bare protons or surface methoxy intermediates, consistent with the associative mechanism¹⁰¹ and suggesting that all sites are covered by methanol monomers or higher order clusters during reaction. Turnover rates (per H⁺, 415 K) measured on small pore CHA zeolites (Si/Al = 15) containing isolated H⁺ sites also appear to proceed via the associative mechanism, based on analogous observations from kinetic and in situ IR data (0.05–20 kPa CH₃OH, 415 K).^{21,101} In situ IR spectra

(0.05–20 kPa CH₃OH, 415 K) of CHA zeolites of similar composition (Si/Al = 15) containing paired H⁺ sites (2 Al per 6-MR), however, show surface methoxy present at coverages that increase with the fraction of paired H⁺ sites²¹, suggesting that the dissociative dehydration mechanism may proceed at paired H⁺ sites in CHA. Furthermore, turnover rates (per H⁺) on CHA increase with the fractions of H⁺ sites in paired configurations^{21,102}, suggesting interactions occur between proximal Brønsted acid sites during catalysis. Deprotonation energies, a theoretical metric of acid strength that scales with methanol dehydration turnover rates on heterogeneous Brønsted acid catalysts^{48,103–107}, are lower for bare acid sites present in paired (up to 19 kJ mol⁻¹ decrease) than in isolated configurations of CHA¹⁰⁸, indicating that nearby protons may interact with deprotonated conjugate base sites to increase acid strength. The precise mechanistic roles of paired and isolated H⁺ site ensembles in CHA, however, are convoluted by inhibition of methanol dehydration rates at high methanol pressures (415 K, >10 kPa CH₃OH)²¹, a phenomenon not observed on medium-pore and large-pore zeolites.^{72,101}

The inhibition of certain alkanol dehydration mechanisms has been previously reported for C₂–C₄ alkanols over solid acid catalysts. Bimolecular dehydration rates of ethanol to form diethyl ether (MFI, FER, MOR; 368–409 K, >6 kPa C₂H₅OH)¹⁰⁹ and propanol dehydration to dipropyl ether (MFI, 413–443 K, <4 kPa C₃H₇OH)⁷⁴ asymptotically approach a zero-order dependence and are not inhibited at higher alkanol partial pressures, similar to reports of methanol dehydration rates on medium-pore and large-pore zeolites.⁷² Ethanol and propanol, unlike methanol, are also able to undergo unimolecular dehydration to form the corresponding alkene. Ethanol

dehydration to ethene is inhibited on MOR zeolites (368–409 K, <6 kPa C₂H₅OH) because additional ethanol molecules adsorb at ethanol monomers and must desorb prior to ethene formation transition states.¹⁰⁹ Similar observations have also been reported for unimolecular dehydration of propanol to propene (MFI, 413–443 K, <4 kPa C₃H₇OH)⁷⁴ and butanol to butene (W-POM/SiO₂, 343 K, <1 kPa C₄H₉OH)¹¹⁰ because the coordination of a second alkanol or water forms dimeric intermediates that are spectators in alkene formation routes. These observations indicate that unimolecular alkanol dehydration to the corresponding alkene (<443 K, C₂-C₄ alkanols) is inhibited by coordination of a second alkanol molecule to form higher molecularity intermediates that behave as spectators, but that such intermediates can condense to eliminate the corresponding dialkyl ether and water at rates (<443 K, C₁-C₄ alkanols) that approach a zero-order kinetic regime at high alkanol partial pressures.

Thus, the high-pressure inhibition of bimolecular methanol dehydration rates (415 K) in small-pore CHA zeolites presents a sharp contrast to the inhibition of only unimolecular alkanol dehydration in medium-pore and large-pore zeolites, and the precise mechanistic origin of this inhibition has remained imprecisely understood. In our prior work, such high-pressure rate inhibition was accounted for by including an elementary step for the formation of an unreactive methanol trimer via quasi-equilibrated adsorption of a methanol at a protonated dimer, to derive an ad hoc rate equation that allowed estimating first-order and zero-order rate constants from experimentally measured rate data on CHA zeolites.²¹ Here, we further investigate the formation and stability of different methanol species at isolated H⁺ sites in CHA zeolites during methanol dehydration catalysis using a combination of kinetic, spectroscopic,

and theoretical probes. High-pressure inhibition of methanol dehydration rates (per H⁺) becomes attenuated at elevated reaction temperatures (>450 K), which coincides with the disappearance of IR vibrational bands characteristic of methanol trimers and larger clusters (~3370 cm⁻¹) detected by in situ IR spectra (343–473 K, 10 kPa CH₃OH). Methanol adsorption isotherms indicate that the onset of dehydration rate inhibition (415 K, per H⁺) occurs at coverages corresponding to >2 CH₃OH per H⁺ site, consistent with IR spectra (0.01–3 CH₃OH/H⁺; 293 K) that show the appearance of methanol clusters at coverages of >0.7 CH₃OH per H⁺ site and that increase in intensity with increasing methanol coverage. Density functional theory (DFT) is used to calculate the Gibbs free energies of various methanol complexes (1–12 CH₃OH per proton) confined within CHA as a function of temperature and methanol pressure, which indicate that methanol trimers are preferentially stabilized in CHA at methanol pressures corresponding to the onset of kinetic inhibition observed experimentally (>10 kPa, 415 K). Apparent free energy barriers for methanol dehydration are calculated considering up to four methanol-derived species on an H⁺ site, in which spectating methanol species are found to insert between reacting species and framework O atoms. DFT-predicted methanol dehydration rates (415 K) are compared with experimental data to determine plausible reaction mechanisms and highlight the critical influence of the zeolite framework on stabilizing reactive and inhibitory intermediates in methanol conversion pathways.

Computational Methods and the Artifacts of Periodic Charged Calculations

Fully periodic density functional theory (DFT) implemented in the Vienna ab initio simulation package (VASP)^{111–114} determined the structures and energies for all states. Calculations were electronically converged to an energy difference between iterations of $< 1.0 \times 10^{-6}$ eV and structurally converged such that the maximum force on any atom

was < 0.01 eV Å $^{-1}$, for acid strength calculations unless otherwise noted. All subsequent calculations for reaction energies had their structures optimized in two steps to improve computational efficiency. Structures were optimized in the first step using a wavefunction convergence criteria such that energy variations between iterations were $< 10^{-4}$ eV and forces were computed with a fast Fourier transform (FFT) grid of $1.5 \times$ the energy cutoff (PREC=.NORMAL. in VASP); structures were relaxed until the maximum force on any atom was < 0.05 eV Å $^{-1}$. These settings may result in inaccurate forces near the minimum; as such, structures are then re-optimized with wavefunctions converged to within 10^{-6} eV and forces computed with an FFT grid 2x the energy cutoff (PREC=.ACCURATE. in VASP). This two-step optimization scheme has been shown to increase computational efficiency by a factor of ~3 for zeolite-based calculations that are sampled at the Γ point⁴².

Calculations were carried out with a plane wave energy cut-off of 400 eV, to form basis set of projector-augmented-waves (PAW),^{115,116} the revised Perdew-Burke-Ernzerhof (RPBE) exchange-correlation functional¹¹⁷ was used along with the DFT-D3 with Becke-Johnson dampening to calculate dispersive forces and energies.¹¹⁸ The BEEF functional^{119,120} and PBE functional¹²¹ with D3BJ were used to verify that trends in acid strength did not vary with choice of GGA by calculating DPE values with each functional; trends were in good agreement across all functionals (see Appendix A, Figure A-7). The Brillouin zone was sampled at the Γ -point. Calculations for radical species were performed with spin polarization to account for unpaired electrons.

The CHA structure was acquired from the international zeolite association (IZA) database¹²² (cell parameters $a = b = 1.3675$ nm, $c = 1.6675$ nm and $\alpha = \beta = 90^\circ$, $\gamma =$

120°); CHA contains one crystallographically unique T-site (36 total in the unit cell) and is shown in Figure 2-2 with a naming scheme for sites in the unit cell and identification of the four crystallographically unique O atoms attached to all T-sites. The framework has six distinct rings adjacent to each site: a 6-MR, two 8-MRs (one containing O₂ and O₃ atoms—8MR(2,3)—and one containing O₂ and O₄ atoms—8MR(2,4)), and three 4MRs. The CHA structure was optimized, and no significant structural deviations were observed compared to the IZA structure.

Zeolites are flexible materials and are prone to restructuring during DFT calculations, as recently emphasized for the MFI framework.¹²³ Therefore, the unit cell parameters of the CHA unit cell were optimized with an energy cutoff of 800 eV without constraints (ISIF = 3 in VASP) to ensure that these initial unit cell parameters would not result in restructuring. These unit cell parameter optimizations yielded a <1 % change in each unit cell parameter; therefore, the initial IZA structure was used in all subsequent calculations. Furthermore, annealing of the CHA structure was simulated with ab initio molecular dynamics (AIMD) in VASP to confirm that restructuring does not occur with the PBE exchange-correlation functional and D3BJ correction. The CHA structure was heated from 200 K to 800 K over 3 ps, held at 800 K for 3 ps, and cooled from 800 K to 100 K over 15 ps, each with a timestep of 3 fs. The resulting annealed CHA structure was subsequently optimized using the same convergence criteria described above. This annealed and optimized CHA structure differed by <1 kJ mol⁻¹ in energy from the directly optimized CHA structure from the IZA database. Moreover, the two structures differed by a negligible distance. These negligible changes in energy and structure indicate that the CHA structure supplied by IZA is sufficiently stable for kinetic studies.

DPE values were calculated as the difference in energy between the isolated charged species and the Brønsted acid site:

$$DPE = E_{Z^-} + E_{H^+} - E_{HZ} \quad (2-3)$$

and DHE were calculated using neutral separated species:

$$DHE = E_{Z^*} + E_{H^*} - E_{HZ} \quad (2-4)$$

NH_3 BE calculations were obtained by the energy difference of the NH_3 -bound state (which always formed a cationic NH_4^+ species) and the proton-form zeolite:

$$E_{\text{NH}_3(\text{ads})} = E_{Z-\text{NH}_4} - E_{HZ} - E_{\text{NH}_3} \quad (2-5)$$

The most stable structures and energies for each protonated state (HZ) were found by systematically placing the hydrogen on each of the four O atoms attached to an Al T-site. Optimization calculations were performed in which the H was positioned 0.104 nm from each O and the out-of-plane angle of the H atom (Figure 2-3 a–b) was varied from 0–330° in 30° intervals. This orientation sampling ensures that the most stable position of the H is obtained for each O atom location. Adsorbed proton species can rapidly move from one O atom to another via proton shuttling oxygenate species (e.g., NH_3 , H_2O , CH_3OH , CH_3OCH_3);^{48,124} therefore, a Boltzmann weighting at 415 K is used produce an ensemble average energy for the protonated zeolite, $\langle E_{HZ} \rangle$, which accounts for this equilibration:

$$\langle E_{HZ} \rangle = \frac{\sum_{i=1}^4 E_{HZ,i} \exp(-E_{HZ,i}/k_b T)}{\sum_{i=1}^4 \exp(-E_{HZ,i}/k_b T)} \quad (2-6)$$

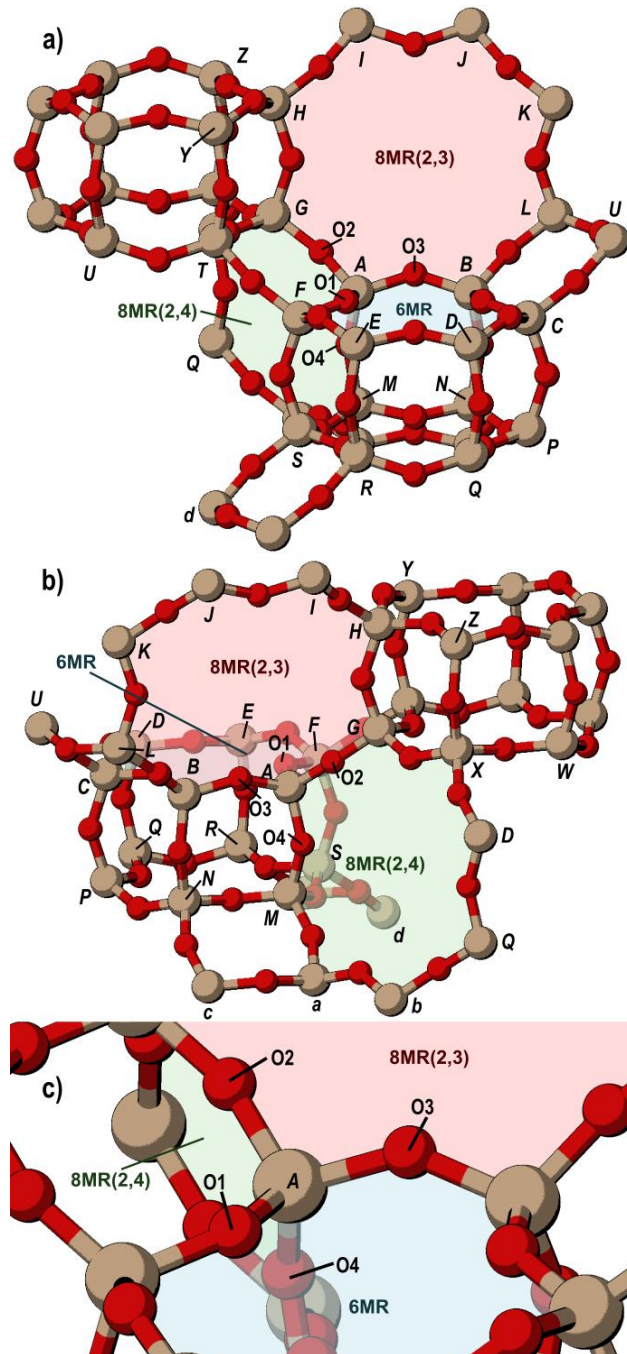


Figure 2-2. The CHA framework; a) and b) show two views in which all T-site designations used in this study are labeled. Also shown and labeled are the 6MR and both 8MR. c) shows the four crystallographically unique O atoms and their location around the 'first' T-site (designated here as site A). The rings labeled are according to the O atoms attached to the A site in each ring.

The arithmetic average of these states ($\overline{E_{HZ}}$) is also used in this work to describe the preferential siting of H on various O atoms and to describe averages across T-site

locations, whose framework locations are not equilibrated. Ammonium ions (NH_4^+) were placed near each O atom of the negatively charged framework and their orientation systematically altered in search of the lowest energy configuration of the adsorbate. The out-of-plane angle of NH_4^+ was varied using methods like those used to rotate a proton around the O to which it was bound and NH_4^+ was also rotated in 30° increments around the N–H bond oriented at the deprotonated O atom (Figure 2-3 c–d).

Vibrational frequencies were determined by a fixed displacement method (two displacements) and used to calculate zero-point vibration energies (ZPVE) and temperature-corrected enthalpies (H) and free energies (G) at 415 K to determine if deprotonation potential energies (E) yielded significantly different trends than deprotonation enthalpies (H) or free energies (G). Frequency calculations froze all framework Si and O atoms that were not bound to the Al atom. The enthalpy and free

$$H = E_0 + ZPVE + H_{vib} + H_{rot} + H_{trans} \quad (2 - 7)$$

$$G = E_0 + ZPVE + G_{vib} + G_{rot} + G_{trans} \quad (2 - 8)$$

energy were calculated at 415 K and 1 bar CH_3OH (standard pressure), the formulas for which are derived from statistical mechanics formalisms (see Appendix A-1 for details).¹²⁵ All motions for guest species within the zeolite framework are considered vibrations, such that translational and rotational H and G are zero for non-gas phase species, which are treated as ideal gases with appropriate equations used from statistical mechanics formalisms. Enthalpies and entropies (S) derived from calculations were used to predict equilibrium constants of adsorption (K) from 300–500 K, in order to predict adsorption behavior of methanol in CHA and to predict equilibrium and rate constants for DFT-predicted rates. Low-frequency vibrational modes disproportionately

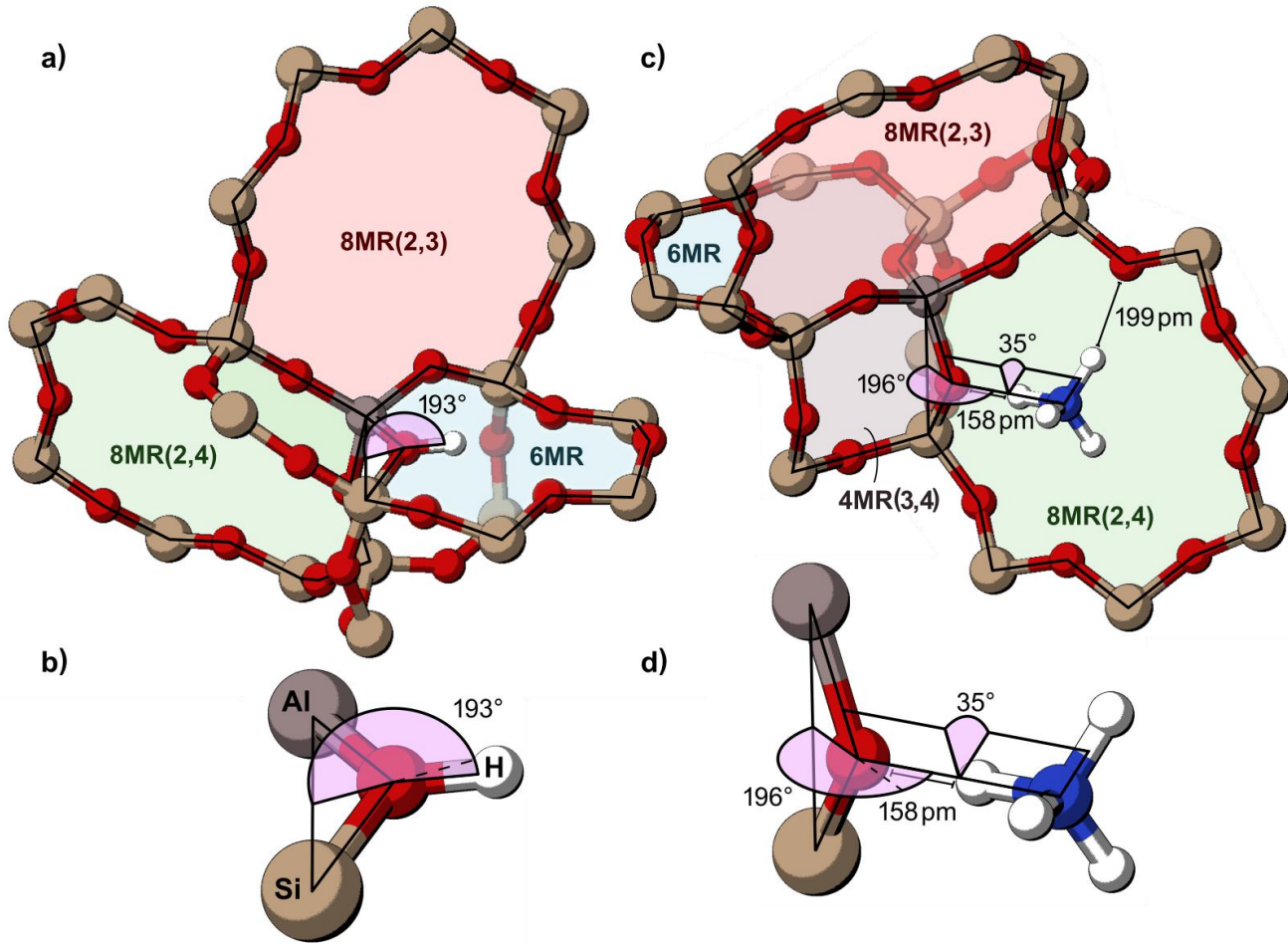


Figure 2-3. Ring structures and angles for CHA, **a)** and **b)** show the out-of-plane angle of a proton bound to the O1 atom of the T-site A. The most stable proton-form structure is depicted in which proton rests in the 6MR of CHA. **c)** and **d)** show the out of plane angle of NH₄⁺ interacting with the O4 atom of T-site A and show the Al–O–N–H torsional angle. The most stable NH₄⁺-form structure is depicted in which the NH₄⁺ rests in the 8MR comprised of O2 and O4 atoms (8MR(2,4)).

contribute to entropy estimates; as such, frequencies below 60 cm⁻¹ were replaced by 60 cm⁻¹ (with the exception of the negative frequency in transition states), as in previous work.^{126,127}

Proximity effects on acid strength were probed by replacing Si atoms 1–3 linking T-sites away from one another to generate Al–(Si–O)_x–Al sites (x = 1,2,3). Concurrent

variations of the out-of-plane angles of both Brønsted sites would require 144 optimization calculations for the 12 angles probed on each site; these 144 configurational calculations were performed on the *AD* site-pair to test their necessity. The preferred out-of-plane H angle for all O atoms on both sites were similar ($< 5^\circ$ and $< 2 \text{ kJ mol}^{-1}$ difference) to those that were found for a H on each O of isolated sites. Therefore, the initial proton positions on O atoms of second sites were altered to match the relative positions obtained for isolated sites prior to optimization. There are four symmetrically unique O atoms (and thus H binding locations) for each T-site, and therefore 16 unique placements in total for both protons on a site-pair. Deprotonation or dehydrogenation can occur on either site, but H atoms were removed only from the first site (the *A* site) because all T-sites are equivalent in CHA. Similar protocols were used to initialize and optimize structures with NH₃ adsorbed to either site or both sites to calculate NH₃ BE values or to calculate the effects of NH₃ adsorption to the second site on the acid strength of the first site.

We examined the effects of unit cell size by combining multiple primitive CHA unit cells into $n \times 1 \times 1$ supercells ($n \leq 6$). Structures were optimized until the maximum force on any atom was $< 0.05 \text{ eV } \text{\AA}^{-1}$ for all calculations performed in CHA supercells. These supercells can be modeled with a constant number of Brønsted acid sites (1) by varying the Si:Al ratio (from 35:1 to 215:1). DPE values for this series increased linearly from 1567 to 1641 kJ mol⁻¹ (Figure 2-4), indicating that either the Al or anion density has a significant impact on DPE values or the artifacts associated with DPE calculations. Supercells were also generated with a constant acid site density and Si:Al ratio (35:1) and only the central site in the supercell deprotonated to test the effect of

anion density, and DPE values for this series also increased linearly from 1567 to 1637 kJ mol⁻¹ as the supercell increased from a primitive cell to a 6×1×1 supercell. This indicated that the anion density must play a role in the artifacts associated with DPE calculations. The overlap of the series with a constant number of acids and the constant Si:Al ratio indicate that the Si:Al ratio has no effect on acid strength at these large ratios ($\geq 35:1$) suggesting these sites are ‘isolated’ from one another. Finally, supercells were generated with a constant Si:Al ratio (35) and all sites within the supercell were simultaneously deprotonated to maintain a constant anion density. The resulting DPE values (normalized per proton) were independent of the size of the supercell, demonstrating that the anion density must be kept constant or used as a correction factor for DPE calculations to compare cells of different sizes (Figure 2-4). This is distinct from previous work¹⁶ that indicated framework density impacted DPE artifacts, however, their application of that correction was successful because framework density correlates strongly with unit cell volume for primitive zeolite unit cells. The supercell calculations done here, however, have identical framework densities, indicating that the true parameter that must be used in these corrections is the density of the anion, which is inversely related to the unit cell volume for DPE calculations involving one deprotonation event. Future work will calculate DPE values in primitive unit cells and variously sized supercells of other zeolite frameworks to determine if the effects of anion density (slope of lines in Figure 2-4) are similar for other materials, in which case one can accurately compare DPE across different frameworks by correcting the anion density effects.

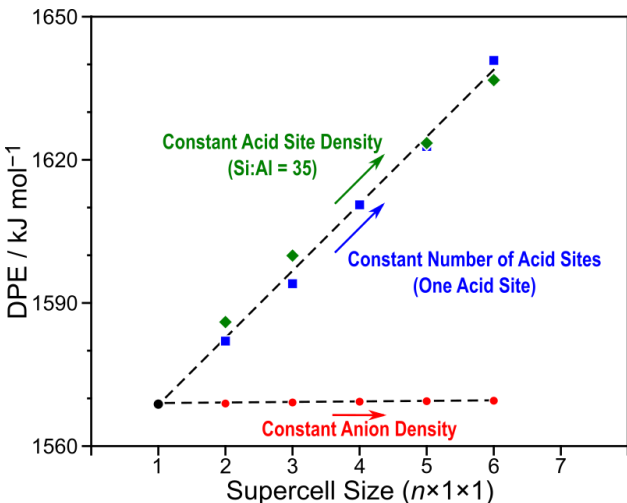


Figure 2-4. The correlation between supercell size and DPE with a constant acid site density (◆, green), number of acid sites (■, blue), and anion density (●, red). Varying anion density (by holding the number of acid sites or the acid site density constant) leads to artifacts in DPE calculations which correlate linearly with this anion density, while DPE remains constant with constant anion density despite changes in supercell size.

Lastly, transition state searches were initiated using the nudged elastic band (NEB) method with 16 intermediate images for each elementary step and converged such that the forces on each atom were $< 0.5 \text{ eV } \text{\AA}^{-1}$.^{13,128} Transition states were then refined starting from these NEB results using the Dimer method⁶¹, where structures were converged using the same criteria as those used for optimizations (energy variation between iterations $< 10^{-6} \text{ eV}$, max force per atom $< 0.05 \text{ eV } \text{\AA}^{-1}$).

Results & Discussion

Predicting the Acid Strength of Isolated Acid Sites in CHA

The CHA framework has four crystallographically unique O atoms (O1–O4, Figure 2-2 c) and each of these O atoms are members of three distinct ring structures. The O1 atom, for example, is a part of the 6MR, the 4MR(1,2) and the 4MR(1,4) where the numbers in parentheses for the 4MRs indicate the O atoms from the A site existing in those distinct ring structures. Varying the out-of-plane angle of the proton around the

O1 atom (Figure 2-3) shows minima (stable structures) when the proton is oriented in the plane of one of those rings and the global minima (most stable structure) orients the proton within the 6MR (Figures 2-5 a and 2-8 a), perhaps because of the relative inflexibility of 4MR structures. The proton weakly H-bonds to other O atoms within the 6MR when bound to O1, as indicated by H–O distances of 2.45 and 2.80 Å. Protons bound to O2, O3, and O4 also prefer to orient within the rings associated with those O atoms. The most stable overall proton location is on O1 (oriented in the 6-MR), followed in order of decreasing stability by O4, O3, and O2 where it resides in 8MR(2,4), 8MR(2,3) and 8MR(2,3), respectively, with electronic energies relative to the most stable O1 configuration of 2, 3, and 10 kJ mol⁻¹, (Figure 2-5). Reorientations of protons across all O atoms indicate that protons are significantly less stable in 4MR orientation than in 6MR or 8MR orientations, indicating that significant strain may be induced when orienting a proton inside a 4MR. Protons readily bind to O1, O3, and O4 atoms in CHA as those energies are within 3 kJ mol⁻¹ of one another (within the limits of DFT accuracy), and are less likely to reside on O2 atoms, and this is consistent with previously calculated values using periodic DFT (with the PBE exchange-correlation functional).¹⁶

The proton is most stable on O1, and therefore the DPE for O1 is the highest of all four O atoms (1572 kJ mol⁻¹; Table 1-1); it is the least acidic HZ state. The proton located on O2 is the most acidic HZ state and has the lowest DPE (1562 kJ mol⁻¹). Energy calculations on the conjugate base can suffer from charge artifacts inherent in DFT⁷⁷ but there is only one conjugate base structure in the isolated acid site making

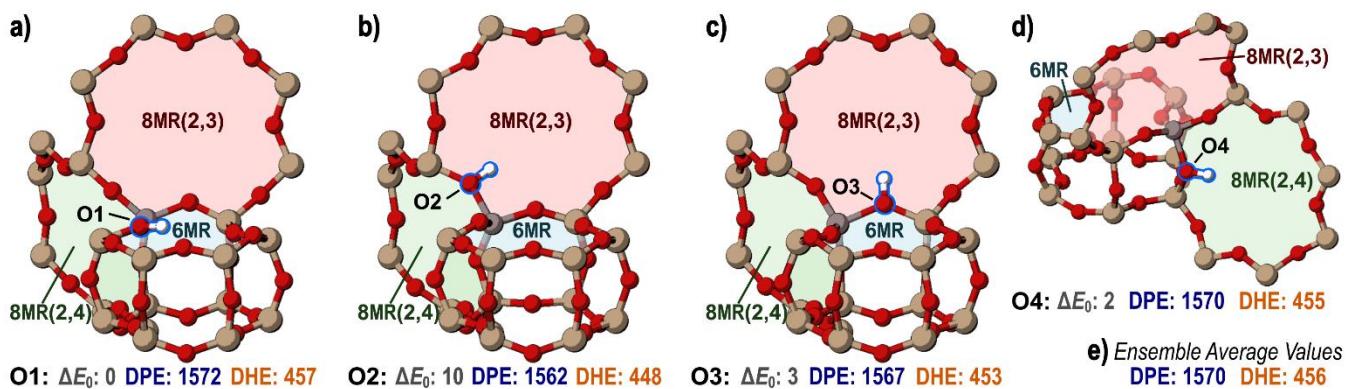


Figure 2-5. The most stable orientation of the proton on **a)** O1, **b)** O2, **c)** O3, and **d)** O4 in the CHA unit cell with only one isolated Brønsted acid site. **e)** lists the ensemble average values of the isolated site for DPE and DHE. The electronic potential energy (ΔE_0) of each state relative to the protonated O1 state is shown, in addition to DPE (Eq. 3) and DHE (Eq. 4), in kJ mol^{-1} .

these charge artifacts identical for all 4 HZ states and should not affect identified trends.

Previous DFT studies (using PBE) found similarly that H bound to O2 is a stronger acid than the others (O1, O3, O4), which have similar DPE values.¹⁶ In experimental environments, protons rapidly move between different oxygens via proton shuttling species (e.g., H_2O , CH_3OH , NH_3) and form an equilibrated set of proton-form structures.¹²⁴ The energy of this equilibrated set of structures can be obtained via ensemble averages (eq. 1-6), which weigh the stability of each HZ state by its relative energy along a Boltzmann distribution. The ensemble average DPE value across the four O atom positions for an isolated Brønsted acid site (at 415 K) is 1570 kJ mol^{-1} , close to the DPE of the least acidic HZ states on O1, O3, and O4 ($1567\text{--}1572 \text{ kJ mol}^{-1}$) because the proton resides on one of these three O atoms 97% of the time according to a Boltzmann distribution of the four relative energies. Therefore, although a proton bound to O2 has the lowest (most acidic) DPE of 1562 kJ mol^{-1} , it becomes catalytically

irrelevant because of its relative instability compared to a proton bound to O1, O3, or O4.

Table 2-1. Electronic energies (E_0), enthalpies (H), and free energies (G) for DPE, DHE, NH_3 BE of isolated Brønsted acids in CHA

	DPE			DHE			NH ₃ BE		
	E kJ mol ⁻¹	H kJ mol ⁻¹	G kJ mol ⁻¹	E kJ mol ⁻¹	H kJ mol ⁻¹	G kJ mol ⁻¹	E kJ mol ⁻¹	H kJ mol ⁻¹	G kJ mol ⁻¹
O1-41	1572	1540	1545	457	424	425	-129	-118	-59
O2-60	1562	1531	1536	448	415	415	-152	-141	-83
O3-77	1567	1536	1541	453	420	421	-156	-146	-85
O4-96	1570	1538	1543	455	422	423	-158	-147	-85
Arithmetic Avg.	1568	1536	1541	453	420	421	-149	-138	-78
Ensemble Avg.	1570	1539	1544	456	422	424	-156	-146	-84

DHE on an isolated site follows the same trend as DPE and is highest on O1 (457 kJ mol⁻¹) and lowest on O2 (451 kJ mol⁻¹). Figure 2-6 a shows a perfect linear correlation between DPE and DHE for these isolated acid site structures in the CHA unit cell. DPE and DHE are related by:

$$DPE = DHE + EA + (E_{H^+} - E_{H^*}) \quad (2 - 9)$$

The electronic affinity (EA) of the H-depleted framework is the difference in energy of the heterolytically and homolytically cleaved conjugate base:

$$EA = (E_{Z^-} - E_{Z^*}) \quad (2 - 10)$$

The EA is constant for these structures because the location and number of the Al atoms present are not being varied. The ionization energy of hydrogen is the difference in energy between the gas-phase H radical and gas-phase proton, which is also constant. Including these constants yields the linear relation for the isolated acid:

$$DPE = DHE + 1115 \quad (\text{kJ mol}^{-1}) \quad (2 - 11)$$

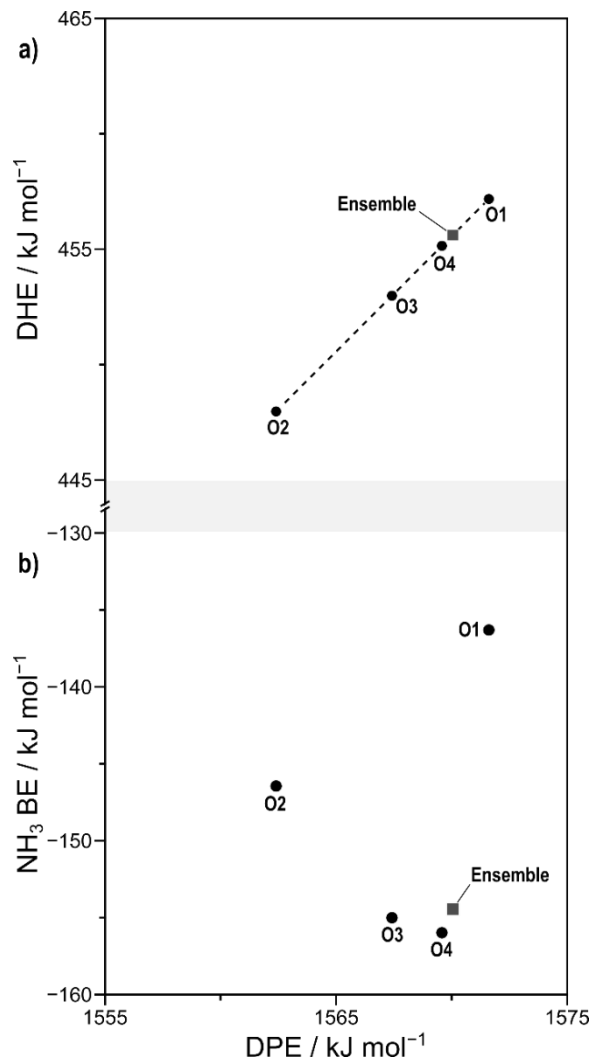


Figure 2-6. The relationship between **a)** DPE and DHE and **b)** DPE and NH₃ BE for isolated acid sites. Circles represent values for individual O atoms and gray squares represent ensemble average values.

Vibrational frequencies for the O–H and Al–O bonds do not significantly depend on the O atom to which the proton is bound. Therefore, zero-point vibrational energies and temperature-corrected vibrational enthalpies and free energies are essentially identical for the four O atom configurations of the isolated acid site, such that DPE and DHE values based on electronic energies are perfectly correlated with enthalpy- or free energy-based values (see Appendix A Figure A-8). Because the relative values of

relevant acid strength metrics are not affected by these correction terms, we will report DPE and DHE values in terms of electronic energies throughout the remainder of this work.

Ammonia binding energies (NH_3 BE) measure a mixture of acid strength and confinement effects because the resulting NH_4^+ cation interacts with the local framework. The shift in confinement effects between a proton and an NH_4^+ cation can alter the preferred orientation of species and confound the relationship between NH_3 BE and acid strength in NH_3 TPD analysis and theoretical assessments.^{76,82,87–92} The most stable orientation of the NH_4^+ near an isolated acid site is in the 8MR(2,4) interacting with the O4 atom of the acid site (-158 kJ mol^{-1}) and H-bonding with other framework O atoms (Figures 2-5 c and 2-11 d). The NH_4^+ cation also resides in 8MR structures when interacting with the O3 (-156 kJ mol^{-1}) and O2 (-152 kJ mol^{-1}) atoms (Figure 1-9). The O1 atom, however, is not in an 8MR, and when the NH_4^+ cation interacts with that site the binding energy is significantly less exothermic (-134 kJ mol^{-1}) as the resulting NH_4^+ cation resides in the relatively large CHA cage (0.74 nm) rather than in a relatively small 8MR window (0.37 nm). NH_4^+ cations fit well within both 8MR windows of CHA, but are too large to fit within the smaller 6MR structures, and thus sit above the 6MR when interacting with O1. Ammonia is also unlikely to reside inside the di-6MR structure, because the NH_4^+ cation causes significant framework strain, leading to weak binding energies (-100 kJ mol^{-1}). The high stability of the protonated O1 state and poor solvation of the NH_4^+ cation by the CHA cage lead to a less favorable binding of NH_3 to O1 (-134 kJ mol^{-1}) compared to the other binding configurations (O2, O3, O4) where NH_3 BE values negatively correlate with DPE or DHE values (Figure 2-6 b), such that

weaker acid sites bind NH₃ more strongly, in contrast to expectations. In real systems, however, the position of the proton and NH₄⁺ cation are determined by a Boltzmann distribution of the relative stabilities of these species around the Al atom (Eq. 2-6) and thus the ensemble average DPE (1570 kJ mol⁻¹), DHE (456 kJ mol⁻¹), and NH₃ BE (-156 kJ mol⁻¹) are more indicative of catalytic performance than calculations specific to each O atom. These ensemble average predictions of acid strength for isolated Al sites will now be contrasted against similar predictions for sites that have a second Brønsted acid site within 1–3 ‘linking’ Si T-sites (Figure 2-2).

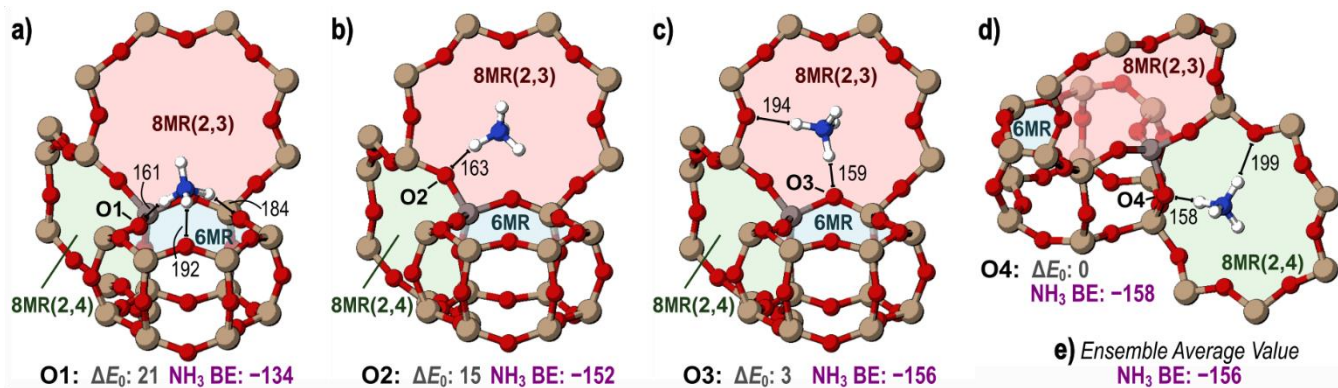


Figure 2-7. The most stable orientations of adsorbed NH₃ on a) O1, b) O2, c) O3, and d) O4 of the isolated site. e) shows the ensemble average value for NH₃ BE on the isolated site. Interactions between framework O atoms and the NH₄⁺ are labeled with their lengths in pm and the NH₃ BE and electronic potential energy (ΔE_0) of each state relative to the most stable orientation of bound NH₃ on O4 are shown in kJ mol⁻¹.

Effects of Acid Site Proximity on Acid Strength

A second Brønsted acid site was created at 23 T-site locations around the A site (Figure 2-2) to determine the effects of proximal sites on acid strength. These additional sites were chosen such that they were separated from the A site by 1–3 T-sites. Protons of each acid site can bind to any one of four O atoms, resulting in 16 total proton configurations for each of 23 proximal acid site-pairs.

The most stable arrangement of a pair of Brønsted acid sites has Al atoms in the *A* and *T* positions which coexist in the 4MR(1,2) (Figure 2-2) and with protons on the O1 atoms of each acid site (Figures 2-12a, 2-13). In this work, we will denote such an arrangement as *A*:O1, *T*:O1 indicating the location of the two Al atoms (as denoted in Figure 2-2) and the O atoms to which each proton is bound. The least stable arrangement of a pair of protons is 92 kJ mol⁻¹ less stable than *A*:O1, *T*:O1 and also involves Al atoms in the *A* and *T* positions, with protons on the O2 and O1 atoms of the *A* and *T* sites, respectively (*A*:O2, *T*:O1). Protons preferentially bind to O1 atoms of both acid sites in 7 cases of the 23 arrangements of Al site pairs (Figure 2-9); in the remaining arrangements, one proton prefers to bind to an O1 atom while the other binds to either the O3 or O4 atom. The preference of protons to bind to O1 atoms, followed closely by O3 and O4 atoms, is observed for isolated sites (in previous section) and this trend persists for proximal acid sites. Taking an arithmetic average of the potential energies relative to the most stable state (*A*:O1, *T*:O1) the sixteen different configurations across 23 arrangements of two Al atoms indicates that protons are most stable on the O1 atoms of proximal sites (average relative *E* of 39 kJ mol⁻¹), and least stable when on O2 atoms (56 kJ mol⁻¹), following trends consistent with those observed for isolated acids (Figure 2-10 a).

Materials with greater amounts of acid sites-pairs within the same 6MR (pairs AC, AD, and AE) can be selectively synthesized^{19,66} and such sites can be titrated with Co²⁺ cations such that their kinetic relevance can be independently determined from isolated sites.¹⁹ Preferred proton arrangements on these sites (AC, AD, AE) involve one proton on O1 and oriented into the 6MR; however, two protons cannot favorably coexist

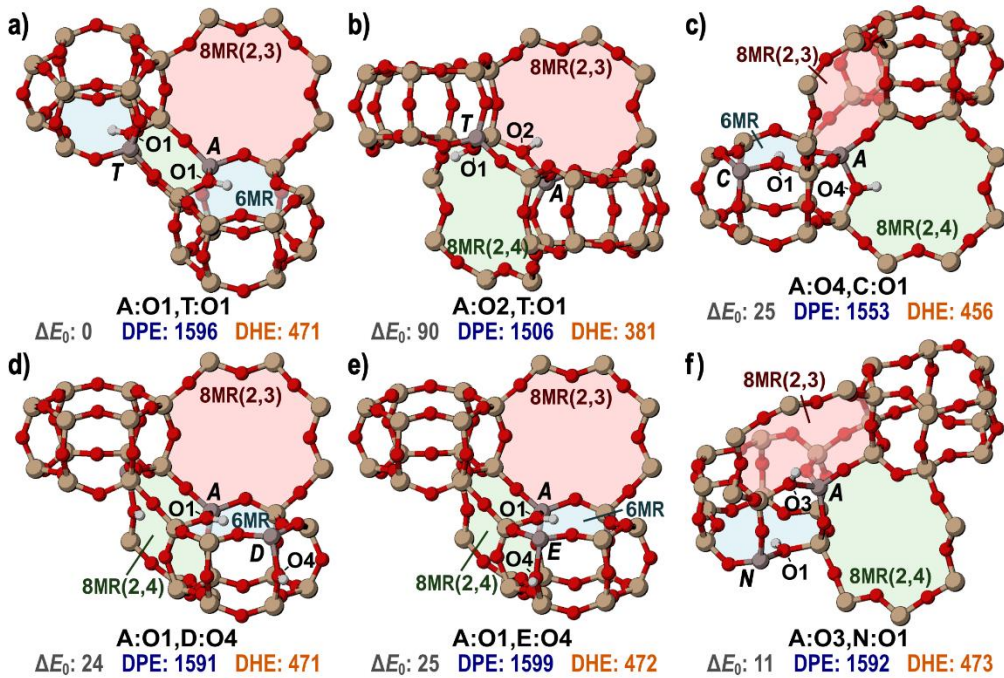


Figure 2-8. Most and least stable proton locations **a)** The most stable protonated state for two Al atoms at the *A* and *T* sites (both protons on O1 atoms of each site) and **b)** the least stable protonated state for the *A* and *T* sites (protons on O2 and O1) in the CHA framework. The most stable configurations of the **c)** *A* and *C*, **d)** *A* and *D*, **e)** *A* and *E*, and **f)** *A* and *N* sites are also shown. The energy of each structure is shown below relative to the A:O1, T:O1 configuration (ΔE_0) with their associated DPE and DHE values in kJ mol^{-1} .

within the same 6MR, causing one of the two protons to bind to either an O3 or O4, as shown in Figures 2-12 c–e and 2-13. These sites (AC, AD, AE) show no remarkable stability or instability compared to other Al atom arrangements (Figure 2-9), indicating that synthesis protocols which increase the likelihood of forming multiple Al atoms within the same CHA cage could form other proximal acid site arrangements, motivating the large number of sites examined in this work and highlighting the need for improved titration and spectroscopic techniques to detect and count such sites.

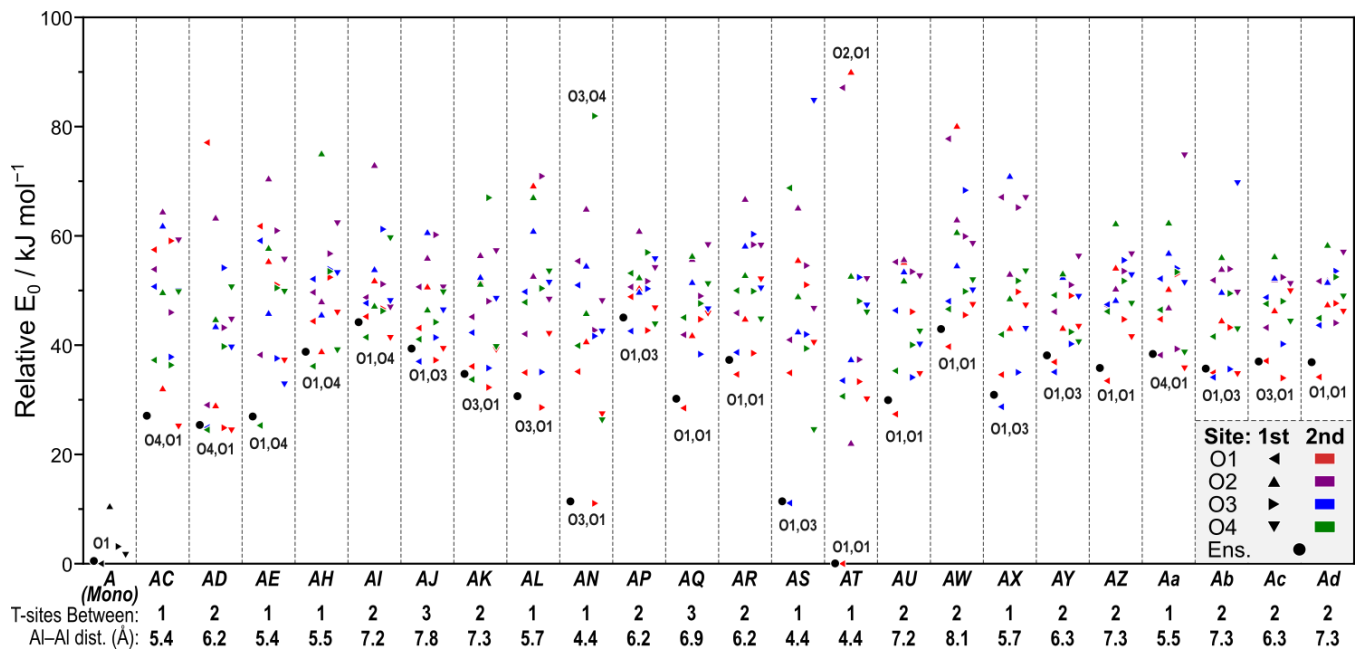


Figure 2-9. Relative E_0 for protons on the four O atoms of isolated sites and the sixteen arrangements of protons for all 23 site-pairs are shown in kJ mol^{-1} .

The distance between Al atoms and the number of Si T-sites linking those sites are shown below. Triangle direction indicates the location of the H on the A site: O1 (◀), O2 (▲), O3 (▶), and O4 (▼). Triangle color indicates the location of the H on the second acid site: O1 (red), O2 (purple), O3 (blue), and O4 (green). The ensemble average energy for each site-pair is also shown by a black circle (●). The most stable configuration of protons is labeled for each site-pair, where the location of the proton on the A site is listed first.

The acid strength of the first site (position A) is estimated by calculating DPE, DHE, and NH_3 BE for all arrangements of protons and bases. The acid strength of the second site is not explicitly calculated because of equivalent nature of all T-sites in the CHA framework. Deprotonation (or dehydrogenation) of the A site leaves that site bare in an anionic (or neutral) form, while the second site has a proton bound to one of its four O atoms. The most stable arrangement of a pair of protons, as discussed, is the A:O1, T:O1 configuration (Figure 2-8 a), and the A site proton has a DPE value of 1596 kJ mol^{-1} , or 28 kJ mol^{-1} higher than that of an isolated site (1568 kJ mol^{-1}), indicating it is a weaker acid; the least stable configuration of protons is the A:O2, T:O1

arrangement (Figure 2-8 b) and this results in a strong acid at the *A* site with a DPE value of 1506 kJ mol⁻¹. The stability of the protons and subsequent conjugate base dictate the stability of the proton arrangement.

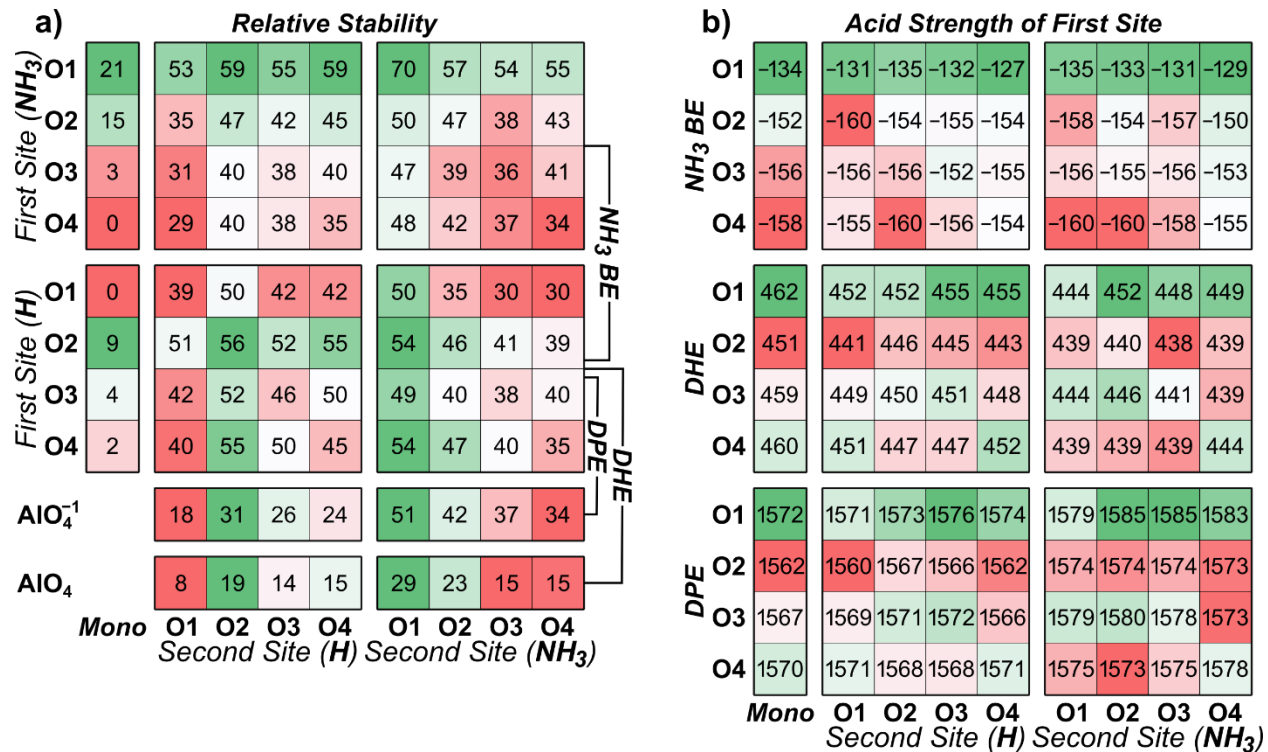


Figure 2-10. Arithmetic averages for **a)** the relative stabilities of the isolated states and of all states averaged across the 23 site-pairs and **b)** the values of acid strength measurements for the isolated states and their values for all states averaged across the 23 site-pairs in kJ mol⁻¹.

The proton configurations with the largest and smallest DPE values are both on the *AN* pair, in configurations *A*:O3, *N*:O2 and *A*:O3, *N*:O4 with DPE values of 1602 and 1498 kJ mol⁻¹, respectively (Figure 2-11). The *A* and *N* sites share a 4MR and are just 4.4 Å apart, and the protons repel one another in the *A*:O3, *N*:O4 configuration, destabilizing the proton on the *A* site (Figure 2-12a), and decreasing DPE. After deprotonation of the *A* site, the proton remaining on the O4 of the *N* site rotates and forms a strong H-bond (1.36 Å) to the O4 atom of the *A* site, resulting in a very stable

conjugate base—the second most stable observed in this work across 92 structures, despite the structural strain induced to accommodate this H-bond configuration (Figure 2-12 b; Appendix A Figure A-1 shows the relative energies of the conjugate base forms). A similar phenomenon occurs on the AS site-pair, where the proton on O1 of the A site is repelled by the proton on O4 of the S site, and the subsequent conjugate base rotates to form a strong H-bond with O4 of the A site, 1.39 Å in length, leading to a strongly-acidic arrangement, despite the removal of a proton on O1 of the A site and the strain on the framework to accommodate the H-bond (Figure 2-12 c–d). The repulsion of the proton pair and subsequent proton-sharing in the conjugate base creates the strong acid at the A site, with a DPE value 70 kJ mol⁻¹ lower than that of an isolated acid site. For most locations of the proximal acid site, the proton-sharing between sites that occurs in the formation of the conjugate base at AN and AS site-pairs cannot occur because larger distances between sites or—in the case of the AT site-pair—the energy required to strain the framework for a shared proton exceeds the benefit of the stabilizing effect of the nearby proton, and absent strong interactions between sites, conjugate bases are generally most stable when the remaining proton is on O1 of the second site, mimicking the stabilities of the isolated proton locations. Figure 2-10 a demonstrates that relative energies of protons on the four O atoms of isolated sites are good predictors for the preference of both proton locations in proximal acid sites and of the second proton location in conjugate base structures when these values are averaged across the 23 locations of the proximal acid site. A strong acid is one with a weakly bound proton and a stable conjugate base, as such, the lowest average DPE value is predicted when the proton to be removed begins on O2 of the A site and the

second proton is on O1 of the proximal site; whereas relatively weak A site acids are present on the O1 of the A site with the second proton on O3 of the proximal site as shown in Figure 2-10 b. These trends indicate how the relative stability of the proton varies across O locations in isolated, proximal, and conjugate base forms, but because of the mobility of these protons, these values are not directly representative of observed acid strength.

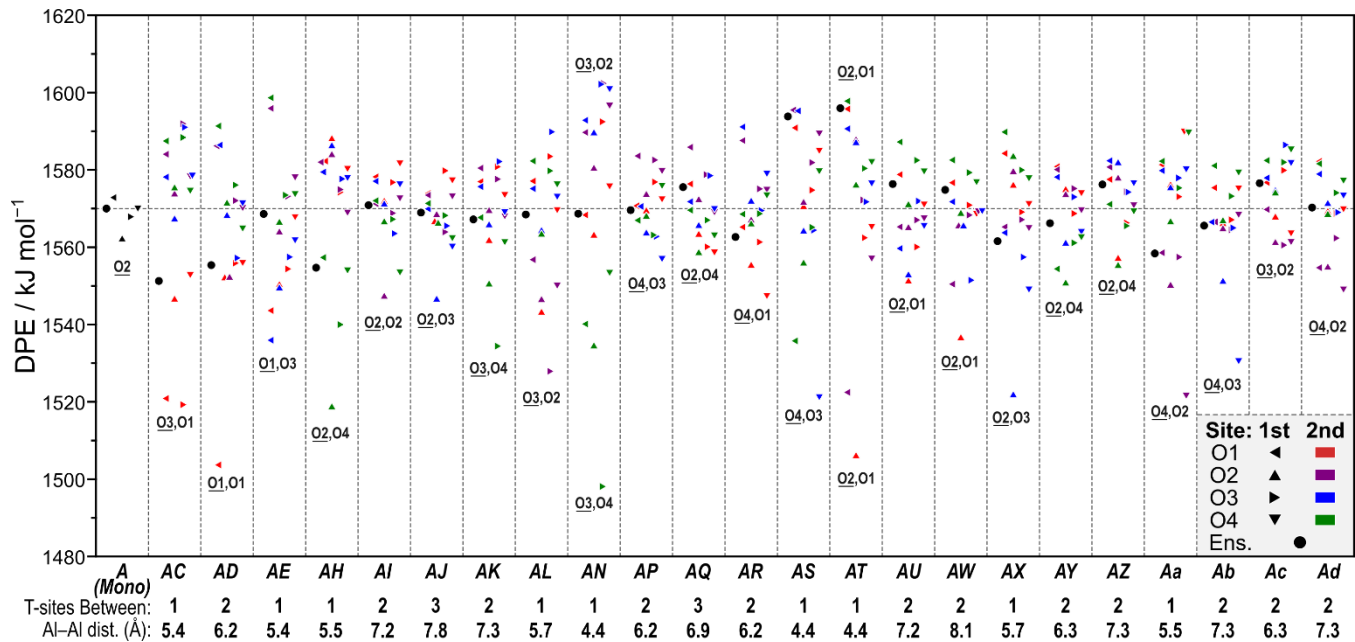


Figure 2-11. The DPE in kJ mol^{-1} for the isolated acid site and all site-pairs where the second site is protonated, with the number of Si linkers between each site and the distance in Å between the Al atoms of each site shown below. The dashed line marks the ensemble average DPE of the isolated site. The location of the most acidic proton combination for each site-pair is marked near its representative point, and the deprotonated O atom on the A site is underlined.

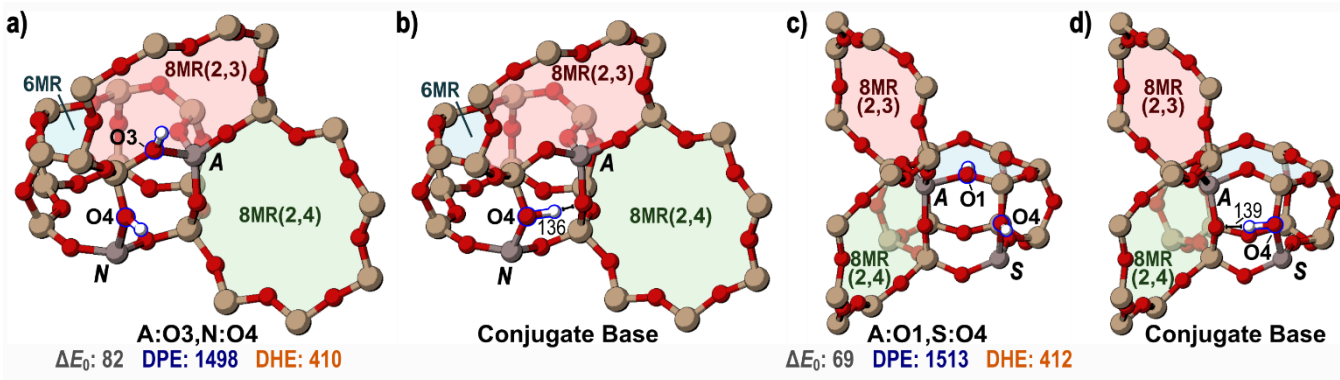


Figure 2-12. Proton positions for paired acid site and their conjugate bases **a)** Protons bound to O3 of the A site and O4 of the N site (A:O3, N:O4) in this structure give the lowest DPE value across all structures examined; **b)** in the most stable conjugate base formed by deprotonation of the A site in a), the remaining proton interacts strongly with the O4 of the deprotonated site. **c)** Protons bound to O1 of the A site and O4 of the S site also have a low DPE value; **d)** their conjugate base exhibits similar behavior to that of the most stable conjugate base of the AN site-pair. The relative stability (ΔE_0), DPE, and DHE values are shown beneath the structures which have not been deprotonated in kJ mol^{-1} and distances between the remaining H and framework O atoms in the conjugate base structures are shown in pm.

The A:O₂, T:O₁ and A:O₃, N:O₄ arrangements are such strong acids (predicted by DPE), in part, because they are relatively unstable arrangements of protons. The mobility of these protons, however, indicates that they are unlikely to reside in these unstable arrangements, even if they are formed in such arrangements. A proper ensemble average of the sixteen proton configurations around Al atoms at both sites and the four configurations of the deprotonated conjugate base structures gives an ensemble DPE value for the AT site-pair of 1596 kJ mol^{-1} , 90 kJ mol^{-1} higher than the A:O₂, T:O₁ arrangement and 28 kJ mol^{-1} higher (less acidic) than the ensemble DPE of an isolated site. Site AN, similarly, has an ensemble DPE value of 1569 kJ mol^{-1} , 71 kJ mol^{-1} higher than the A:O₃, N:O₄ configuration and 1 kJ mol^{-1} higher than the ensemble DPE of an isolated site. These examples, applied to Al arranged in the AT

and *AN* site-pairs, demonstrate the importance of ensemble average DPE values. Unstable arrangements of protons, while having weak O–H bonds and thus low DPE values, rarely exist because of the equilibrated nature of proton transfer among nearby O atoms and this is accounted for by using a Boltzmann distribution for each state (Eq. 2-6) within ensemble DPE values. All values reported here are from the RPBE-D3BJ functional, whose trends in ensemble DPE match those of other common functionals used in zeolites (PBE-D3BJ and BEEF; see Appendix A).

The *AC*, *AD*, and *AE* site-pairs within the 6MR of CHA are of particular interest because they can be selectively formed, counted, and thus kinetically tested.^{19,66} The *AC* and *AD* site-pairs have ensemble average DPE values lower—1551 and 1555 kJ mol⁻¹, respectively—than that of an isolated site (1568 kJ mol⁻¹). Upon deprotonation of the *A* site, the remaining protons form H-bonds (2.30 and 1.97 Å) across the 6MR to interact with the conjugate base for both the *AC* and *AD* site-pairs (Figure 2-15 a,b), similar to the anion-proton interaction that occurs to stabilize the conjugate base for the *AN* and *AS* site-pairs. The *AE* site-pair has an ensemble DPE value nearly identical (1569 kJ mol⁻¹) to that of the isolated site (1568 kJ mol⁻¹); in its most stable conjugate base configuration, the proton does not reside on O1 but instead on O3 and does not bridge the 6MR to stabilize the deprotonated *A* site. The *AH* and *Aa* site-pairs also have ensemble DPE values (1555 and 1558 kJ mol⁻¹, respectively) lower than the isolated site. The *A* and *H* sites are in the same 8MR(2,3), and there is evidence of anion-proton interactions in the conjugate base with a distance of 2.58 Å between the proton and the nearest O atom of the anion (Figure 2-13 c). The conjugate base of the *Aa* site-pair has no close proton-anion interaction as the proton points away from the *A* site, not towards

it (Figure 2-13 d), but the remaining proton is near the A site indicating that a dipole-dipole interaction between the O–H bond of the second site and the Al–O bonds of the anion stabilize the deprotonated site. This sharp reduction in DPE for site-pairs which share rings and are near enough to interact favorably is illustrated by Figure 2-14, which shows ensemble DPE values for all site-pairs tested. These examples give three distinct methods of stabilizing a conjugate base and therefore decreasing DPE.

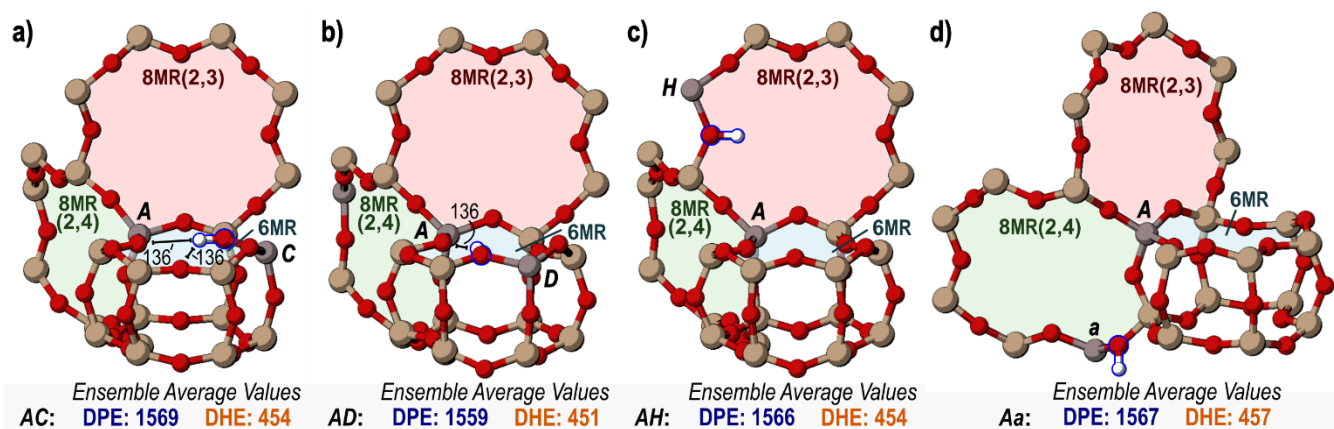


Figure 2-13. The most stable conjugate bases for site-pairs **a)** AC, **b)** AD, **c)** AH, and **d)** Aa. Interactions between the proton of the second site and framework O atoms are shown in pm where appropriate. Ensemble average DPE and DHE values for each site-pair are shown below each structure in kJ mol^{-1} .

Stabilizing the conjugate base is key to decreasing DPE, and proton-anion distances in the conjugate base structures strongly impact DPE. Proximal sites for which the remaining proton is near the deprotonated site can form stabilizing proton-anion interactions (H-bonds, dipole-dipole) upon deprotonation and thus have lower DPE values, as shown in Figure 2-13. Ensemble average DPE values increase with

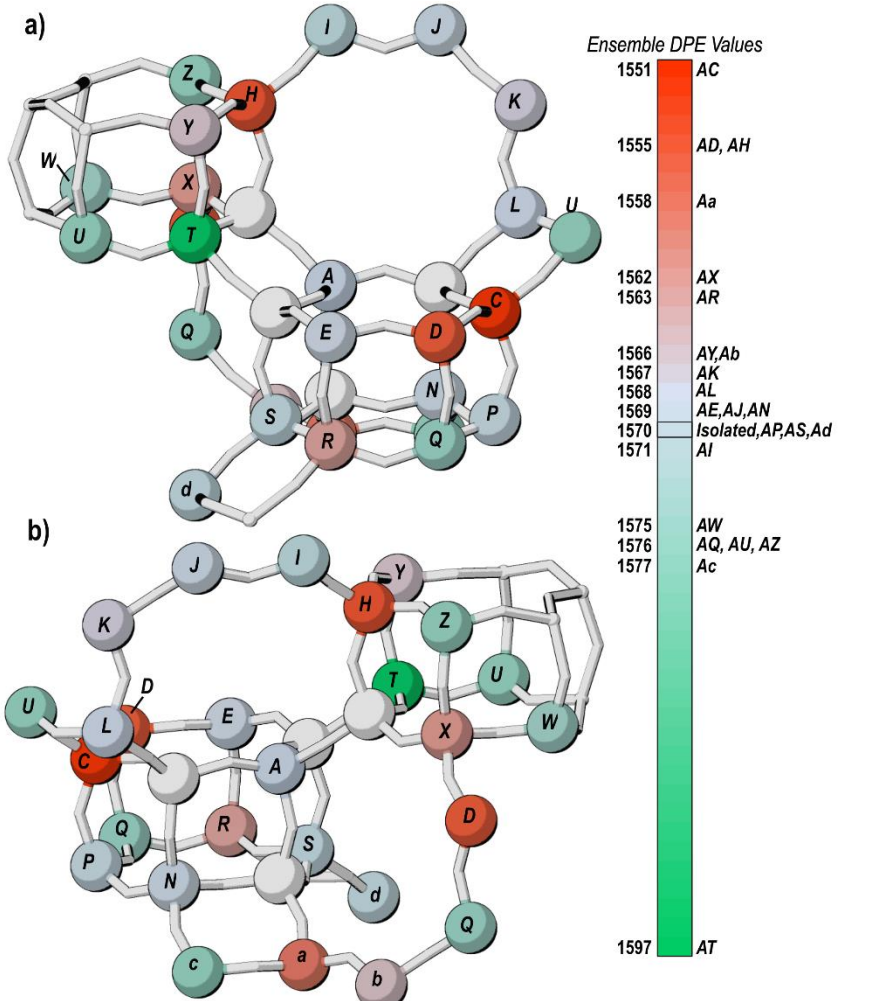


Figure 2-14. A diagram illustrating the effect of relative framework location on ensemble DPE values for site pairs showing **a)** the 6MR and 8MR(2,3) and **b)** the 8MR(2,3) and 8MR(2,4). Site-pairs whose DPE are higher than that of the isolated site (weaker acids) are shown in green and those whose DPE are reduced (stronger acids) are shown in red, with a corresponding color scale and associated ensemble average DPE value on the right.

proton-anion distances (as measured by the distance from the proton to the nearest O atom of the anion), and sites with an ensemble average distance in their conjugate bases higher than 4 Å typically have ensemble average DPE values higher than that of the isolated site (Figure 2-15). Site-pairs AN and AS have the closest proton-anion interactions (as shown in Figure 2-12 b and 2-16 d), however, these interactions are present in 4MR structures that have been significantly strained, negating the stabilizing

effect of the nearby proton to the conjugate base, and resulting in DPE values similar to those of the isolated site. The *AT* site-pair is also present in a 4MR, but its conjugate base does not have a strong anion-proton interaction because the locations of the *A* and *T* sites in the 4MR are not conducive to the proton sharing seen in the *AS* and *AN* site-pairs, which results from the preferred orientation of protons on O1 and O2 of the *T* site, where sharing protons with the *A* site across the 4MR would result in unfavorable strain. Therefore, the DPE of the *AT* site pair (like sites *AS* and *AN*) is much higher than the trend formed by the remaining 20 site-pairs. After the *AT* site-pair, the *Ac* site-pair has the highest ensemble DPE value (Figure 2-14). Acid strength can be adjusted by altering the proximity of acid sites, where nearby sites sharing 6MR or 8MR have lower DPE values, and nearby sites sharing 4MR or sites which, upon deprotonation, have a proton and anionic O atom separated by 4 Å or more have higher DPE values.

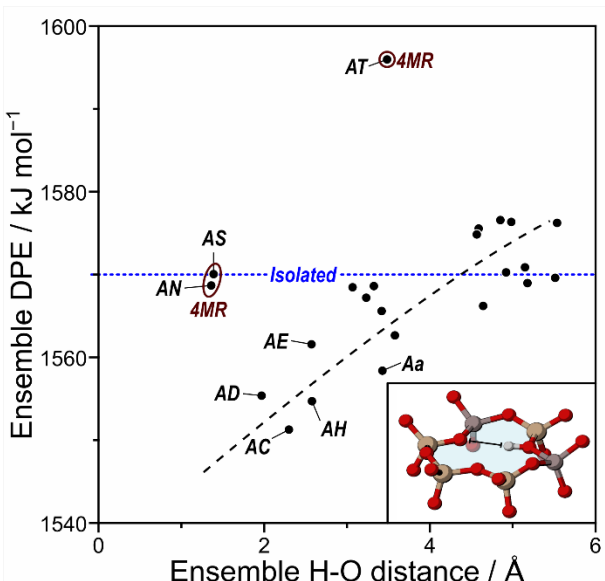


Figure 2-15. Ensemble average DPE in kJ mol^{-1} as a function of the ensemble average distance in Å between the H of the second site and the nearest O of the deprotonated A site. The horizontal dashed line represents the ensemble average value for the DPE of the isolated site, while the sloped dashed line represents a linear fit. The inset at the bottom right shows an example of the shortest H–O distance for the deprotonated AC site-pair in the 6MR.

DHE was also used to probe the acid strength of the A site with a second site in the unit cell. The lowest DHE (indicating the weakest O–H bond) is observed for the A:O₂, T:O₁ arrangement (381 kJ mol⁻¹), a value 75 kJ mol⁻¹ lower than that of the isolated site (456 kJ mol⁻¹). The low DHE of the first site reflects the instability of the H atom on O₂; this state is the least stable arrangement of protons and has a low DPE, as previously described. Average DHE values across all proximal site locations for different arrangements of H atoms show similar trends with those from the isolated site; when the proton is on O₂, the H–O bond is most easily homolytically cleaved (Figure 2-10 b). Average values across proximal site locations also show strong correlation between DHE and DPE; by both measurements the strongest acids are arranged with a proton on O₂ of the A site and O₁ of the second site and the weakest acids are arranged with a proton on O₁ of the A site and O₃ of the second site.

These values reflect the relative strengths of O–H bonds on various O atoms, but the mobility of H atoms in such systems dictates that ensembled values will reflect their behavior. Ensemble average DHE values for these AT and AS sites were 471 and 470 kJ mol⁻¹, both higher than the DHE value of an isolated site (456 kJ mol⁻¹), indicating stronger O–H bonds than that of the isolated site. The DHE of the AC, AD, and AE sites were 454, 451, and 460 kJ mol⁻¹, which are all similar to the DHE of the isolated site while their DPE values were lower than that for an isolated site; this indicates that, while a proximal proton can stabilize the conjugate base of the homolytically cleaved H–O bond, the stabilizing benefit conferred by that proton is much stronger when the resulting base is anionic.

A strong trend between ensemble average DPE and ensemble average DHE exists for site-pairs in the CHA unit cell (Figure 2-16 a). The electron affinity (Eq. 2-10) for each site-pair differs because sites now interact electronically over shorter distances; therefore, the perfect parity between DPE and DHE on the isolated O atoms disappears. The slope of a linear fit for this relationship is less than 1, indicating that electron affinity decreases when sites share a unit cell and interact. This decrease is an indication of the stabilizing effect that a nearby proton has on a nearby anionic site and offers insight into the increased reactivity for proximal sites where charge separation occurs during reaction.

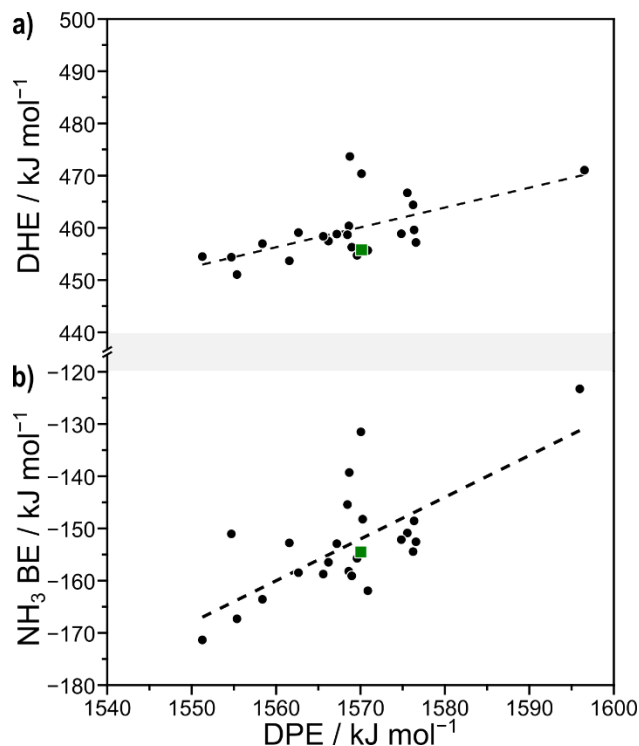


Figure 2-16. The relationship between **a)** DPE and DHE and **b)** DPE and NH₃ BE for all site-pairs where the second site is protonated. Energies shown are ensemble averages for each measurement of acid strength in kJ mol⁻¹. Dashed lines represent linear fits and green squares represent the ensemble average DPE, DHE, and NH₃ BE of the isolated site.

Ammonia adsorption energies on site *A* were also calculated in the presence of a proximal (protonated) acid site. NH₃ can interact with a proton bound to one of four O atoms at the *A* site and the second proton can bind to one of four O atoms at the second site, creating 16 unique structures per proximal acid site location. NH₃ deprotonates acid sites, forming an NH₄⁺ cation, in all cases. The most stable NH₃ structure is observed when the NH₄⁺ cation interacts with the O4 atom of site *A* (in the 8MR(2,4) ring) while the proton of the second site is bound to the O1 atom of site *C* (*A*:O4, *C*:O1), as shown in Figure 2-17 a. The NH₄⁺ is stabilized most in the 8MR(2,4), just as was observed for NH₃ bound to the isolated acid site (Figure 2-7 d); in this case, a second proximal proton stabilizes the anionic *A* site across the 6MR upon adsorption of NH₃, as was observed in conjugate base structures after deprotonation (Figure 2-13). NH₄⁺ is similarly stable on the *A*:O4, *D*:O1 site for the same reasons; ammonia adsorption entails heterolytic cleavage of the H–O bond, the negatively charged *A* site is stabilized by proximal protons. NH₃ is least stable when bound to O1 of the *A* site with a nearby proton on the *E* site (Figure 2-17 c); this instability results from unfavorable interactions between the NH₄⁺ and the proton. These unfavorable interactions push the proton on O1 of the *E* site into an unstable position above the 6MR, inducing strain the framework, much like two protons on the O1 sites of the *AC*, *AD* and *AE* site-pairs. The stabilization of a bound NH₃ follows trends that are similar to those of NH₃ stability on the isolated site (Figure 2-10 a): it is generally most stable on O4 and least stable on O1. When there is a second proton nearby, the NH₃ is most stable when the proton is on O1 of the second site, and least stable when the NH₃ binds to O1 of the *A* site and a proton is on O2 or O4 of the second site.

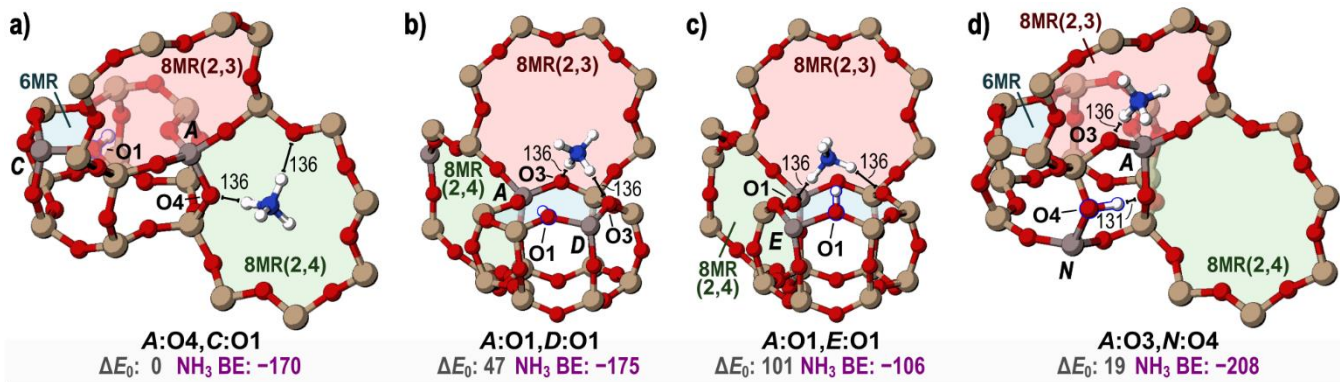


Figure 2-17. The adsorbed ammonia on **a)** O4 of the A site with a proton on O1 of the C site, **b)** O1 of the A site with a proton on O1 of the D site, and **c)** O1 of the A site with a proton on O1 of the E site, and **d)** O3 of the A site and O4 of the N site. Stabilities relative to the A:O4, C:O1 configuration shown in **a)** (ΔE_0) and NH_3 BE for the configuration shown for each site-pair are shown in kJ mol⁻¹. Interactions between H atoms and O atoms of the framework are shown in pm.

More exothermic NH_3 BE values are observed when relatively unstable protons create relatively stable NH_4^+ cations upon NH_3 adsorption. The strongest NH_3 adsorption site is the A:O3, N:O4 site with an NH_3 BE of -208 kJ mol⁻¹; this site also has the highest DPE observed in this work (Figure 2-17 d). While the stabilizing effects of the nearby proton can still impact acid strength measurements, the formation of an extra framework cation which can interact unfavorably with the remaining proton leads to different trends for acid strength of individual combinations of protons for DPE and NH_3 BE (Figure 2-10 b). Because protons and NH_4^+ are mobile, these individual values are not reflective of realistic behavior of these sites, and an ensemble average more accurately reflects the physical properties related to acid strength.

Ensemble average NH_3 BE values for NH_3 bound to the A site are most exothermic for site pairs AC and AD with values of -171 and -167 kJ mol⁻¹, which are > 10 kJ mol⁻¹ more exothermic than that of the isolated site (-156 kJ mol⁻¹). Site-pair AE, which also involves two sites in the same 6MR, has an ensembled NH_3 BE slightly more

exothermic (-158 kJ mol^{-1}) than isolated sites. The proximal acid in the 6MR stabilizes the deprotonated and anionic A site to which NH_3 binds, similar to the stabilization that occurs upon deprotonation to a non-interacting distance (DPE) which also shows that acids are stronger with proximal Al at sites C and D. Ensemble average NH_3 BE and DPE trend strongly (Figure 2-16 b). This indicates that experimental NH_3 BE measurements, while they can be corrupted by interactions between NH_4^+ cations and the framework, still trend strongly with purely theoretical measurements of acid strength. The strong correlation between NH_3 BE and DPE was not observed in a previous study examining the acid strength of sites across many frameworks,¹⁶ however, changing framework identity or acid site location will significantly alter guest-host interactions between the NH_4^+ cation and the local framework. This study, in contrast, examines the strength of NH_3 adsorption at a single T-site in a single framework and is only altering the presence and location of a proximal acid site, which cause these guest-host interactions to cancel in comparisons.

The Sphere of Influence of Acid Sites

To determine the distance at which a second site influences the acid strength of a Brønsted site, DPE and DHE were calculated for 143 Brønsted acid site-pairs in a $4 \times 1 \times 1$ CHA supercell. In each orientation, the same centrally located T-site was deprotonated or dehydrogenated. The resulting DPE values were not corrected for their anion densities and are therefore not comparable to those calculated for site-pairs in the CHA primitive unit cell but can be compared to one another and thus give insights into the distance over which sites impact each other.

Ensemble DPE values are not well-predicted by Al-Al distances, indicating the strong impact of the exact arrangement of Al atoms across different structural motifs

(e.g., 6MR, 8MR) as described in preceding sections. With this scatter, Figure 2-18 a also shows a general increase in ensemble DPE values with increasing Al–Al distances as DPE increase from ~1605 kJ mol⁻¹ (on average) at distances of 9 Å to ~1615 kJ mol⁻¹ at distances > 24 Å along with a concomitant decrease in the scatter, indicating that specific arrangements matter less for sites separated over large distances, as expected. This general increase in DPE values is either caused by shifts in the electron affinity (EA) of the conjugate base or by electronic interactions which exist in charged periodic calculations. EA are altered by nearby Al atoms; the excess electron is expected to localize at the deprotonated site in this semi-conductor material, such that one would expect electron affinities to be governed by local structure (unlike calculations of acid sites on metals which reflect global composition).²² Alternatively, the long-range effects of Al–Al distance on DPE could be related to the dipole-dipole interactions present for charged periodic calculations that cannot be sufficiently accounted for using these methods. The residual spread in DPE values observed at large distances likely reflects inherent error in DFT methods and does not reflect interactions or differences in T-site locations as all T-sites are crystallographically identical within the CHA framework.

Ensemble average DHE values, in contrast to DPE values, do not probe electron affinities of the conjugate base and are also uncorrupted by the large dipole-dipole interactions present in the calculation of charged states in periodic DFT methods. The spread in DHE values, like DPE values, is significant at short distances but rapidly decreases with increasing Al–Al distance (Figure 2-18 b). Unlike DPE, no general increase in DHE values is observed as Al–Al distances increase, ensemble DHE values

approach $\sim 450 \text{ kJ mol}^{-1}$ and remain constant, with scatter, across all Al–Al distances $> 9 \text{ \AA}$. Only 13 site-pairs in the supercell have ensemble DHE values which differ by $> 5 \text{ kJ mol}^{-1}$ from this limiting value; 10 of these site pairs (77%) are separated by $< 9 \text{ \AA}$, despite only 31 of the 143 site-pairs tested in the supercell (22%) being separated by less than 9 \AA . The largest variation in DHE values also occurs within this range. Therefore, interactions between sites are most impactful when T-sites are separated by $< 9 \text{ \AA}$.

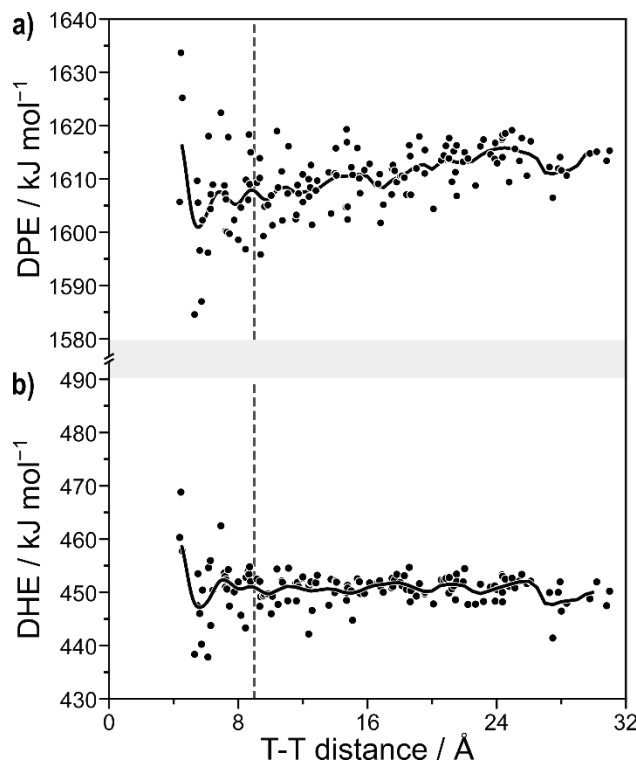


Figure 2-18. Ensemble average values for **a)** DPE and **b)** DHE as a function of the distance between Al T-sites in the CHA supercell. The solid black line in each part represents a moving average value for DPE or DHE. Dashed vertical lines represent the 9 \AA distance at which site interaction becomes negligible.

These data varying the distance between Al sites from 4 to 31 \AA provide contradictory sizes for the sphere of influence of an acid site within CHA. DPE values

are impacted more by proximity than DHE values, with greater scatter and continued shifts in DPE values even at large distances ($> 20 \text{ \AA}$). Such effects, however, cannot be separated from the artifacts inherent in these calculations and higher methods applied to cluster models of this size are computationally intractable. DHE values, apart from few outliers, indicate that acid sites do not noticeably interact with one another over distances $> \sim 9 \text{ \AA}$, roughly corresponding to Al sites separated by 3 Si Ti-sites. This cutoff is qualitatively consistent with the effects observed in the primitive CHA unit cell, indicating that Brønsted acids are most affected by the placement of a second site 1–2 T-sites away. However, the adsorption of a base (NH_3) to the second site and the subsequent formation of a cation at that site (NH_4^+) that is significantly larger than a proton increases the range over which acid sites interact, leading to significant increases in acid strength for sites within 8MR separated by 3 T-sites (e.g., the AJ site-pair, whose Al are separated by 7.8 \AA). These data within the $4 \times 1 \times 1$ supercell and in the primitive unit cell, taken together, indicate that sites up to $\sim 9 \text{ \AA}$ apart, or separated by 3 T-sites, can influence one another.

Proximity of Sites with Varying Si:Al Ratio

Bulk Si:Al ratios influence Al–Al distances. Here, we estimate these impacts by simulating Al arrangement assuming a random distribution of Al is generated while obeying Löwenstein's rule¹²⁹ such that no two Al are located at adjacent T-sites. Interactions between Brønsted acid sites depend on Al–Al distances, but also upon the specific arrangement of Al atoms such that no general trend exists between Al–Al distance and shifts in acid strength caused by proximity. However, Figure 2-18 does indicate that Al–Al distances $> 9 \text{ \AA}$ can be considered effectively isolated, while a fraction of Al separated by $< 9 \text{ \AA}$ will interact with one another. Figure 2-19 shows the

fraction of Al atoms that have a neighboring Al within 5–16 Å as a function of the Si:Al ratio. For example, 72% of Al have an Al neighbor within 9 Å at a Si:Al ratio of 30, while only 9% have an Al neighbor within 5 Å (across a 4-MR in this framework). As Si:Al ratios decrease, average Al–Al distances decrease and higher fractions of Al atoms have neighbors at close distances. For example, at a Si:Al ratio of 4 (similar to the chabazite mineral), over 60% of Al have a neighbor within 5 Å. These distance distributions indicate that even high Si:Al ratio materials may have a small fraction of paired sites in the specific arrangements (Figure 2-14) which alter acid strength. Previous work has more thoroughly investigated the effects of Si:Al ratio on acid strength in FER and similarly found that nearby sites interact with one another at low Si:Al ratios,⁸⁶ a finding which is corroborated here. Random distributions of Al sites, however, do not result from target synthesis approaches of more recent investigations,^{19,66} but these still give insights into how proximal acid sites behave in low Si:Al ratio CHA frameworks.

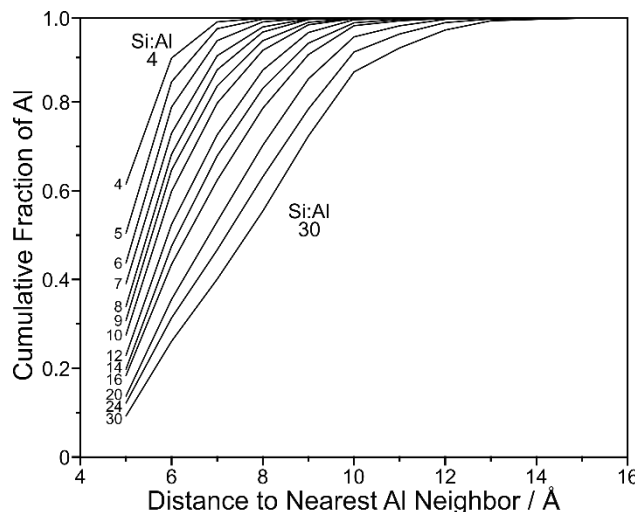


Figure 2-19. Fraction of sites at a variety of Si:Al ratios with random Al distribution in CHA with nearest Al between 3 and 16 Å away. Curves are labeled on the left with the Si:Al ratio they represent.

Altering the State of Proximal Acid Sites

We have considered how a proximal acid site would increase or decrease the strength of the Brønsted acids in CHA. The structures considered in those studies placed a bare proton on the second acid; zeolite-catalyzed reactions, however, rarely occur at conditions that would result in bare protons. Methanol dehydration, for example, occurs on sites covered in a mixture of methanol monomers and dimers as indicated by kinetic studies showing rates that begin linearly dependently on methanol pressure and approach saturation behavior at higher methanol pressures.⁷² This typical Langmuir-Hinshelwood kinetic behavior indicates that surface composition changes over this range of methanol pressures (0–15.3 kPa CH₃OH) and can be explained by a transition from bare to methanol-covered surfaces or by a transition from surfaces covered in methanol monomers to a surface covered in methanol dimers. The arbiter of this disagreement is *in situ* FTIR studies that show the complete disappearance of the vibrational signature of bare O–H bonds between 0.2 and 0.5 kPa CH₃OH (at 415 K), indicating that at very low CH₃OH pressures, bare protons are not present.⁷² The absence of bare protons is also inferred from kinetic data for ethanol dehydration,⁵² for arene methylation (and associated reverse-titration experiments),¹³⁰ and for alkene oligomerization.¹³¹ This work demonstrates the strong interactions of bare protons with bases, with NH₃ BE values ranging from −106 to −208 kJ mol^{−1} and an ensemble average binding energy on isolated sites of −156 kJ mol^{−1}. These strongly exothermic interactions predict that all surfaces would be covered by NH₃ at low temperatures during any NH₃ TPD study and that such surfaces would likely be covered during

relevant catalytic reactions, such as methanol dehydration which has been previously studied for isolated and paired sites in CHA.^{19,72}

Therefore, the effects on the state of the second acid (bare, covered) are critical and were determined here by recalculating DPE, DHE, and NH₃ BE for the same 23 proximal acid site locations with NH₃ adsorbed to the second site. Figure 1-12 b shows that, regarding the arrangements of NH₄⁺ cations and protons, similar trends are observed whether the proximal site is a bare proton or deprotonated by NH₃: H is most easily removed from O2 and NH₃ binds most weakly to O1 and most strongly to O4 when NH₃ is bound to the second site. Similar conclusions can therefore be reached regarding the preferred O binding of protons and NH₄⁺ cations as those discussed previously. In this section, we will focus on the effects of the state of the second acid on ensemble average values which reflect the performance of such materials when protons and NH₄⁺ cations are mobile.

Adsorbing NH₃ to the proximal site weakens the acid strength of a proton at the A site, with ensemble DPE values increasing by an average of 11 kJ mol⁻¹. Bare protons at proximal positions can H-bond to anionic sites in conjugate base structures, and this stabilization is disrupted in the absence of a bare proton as the second site has been deprotonated upon contact with NH₃. Considering specifically the AC, AD, and AE site-pairs in which both Al atoms are present in the same 6MR, ensemble DPE values change from 1551, 1555, and 1569 kJ mol⁻¹ with a bare proximal proton to 1595, 1588, and 1608 kJ mol⁻¹ with a proximal NH₄⁺ cation at the nearby C, D, or E site, respectively. These increases of ~40 kJ mol⁻¹ in ensemble DPE suggest that acid site proximity causes acids to weaken compared to isolated states (DPE of 1568 kJ mol⁻¹),

in direct contrast to the behavior of proximal bare acids, which typically cause these acids to become stronger. Ensemble average DPE values increased upon adsorption of NH₃ to the second site for most site-pairs examined in this study (Figure 2-20), but decreased by > 10 kJ mol⁻¹ for the AJ, AK, and Ab site-pairs; in each of these cases, acid sites are separated by > 7 Å and share an 8MR, indicating the ability of the NH₄⁺ cation to stabilize the deprotonated conjugate bases across 8MR structures (Figure 2-21 b-d), similar to the ability of protons to stabilize conjugate base structures across 6 MR structures. Sites in the 6MR are stabilized by the NH₄⁺ cation similarly to the proton stabilizing the anionic A site when it remains protonated; for example, upon deprotonation of the A site when NH₃ is adsorbed to the D site, the NH₄⁺ is no longer located above the 6MR, but is pulled down by the anionic A site such that it is planar to the 6MR (Figure 2-21 a), but this does not lead to an increase in the stability of the conjugate base. The disruption of the ability of protons to stabilize conjugate base anions across 6MR and over short distances along with the enhanced ability of NH₄⁺ cations to stabilize conjugate base anions across 8MR and longer distances results in no strong correlation between ensemble DPE values as the state of the proximal site changes (Figure 2-20), indicating the need to understand these interactions on a molecular level for each cation (proton or NH₄⁺).

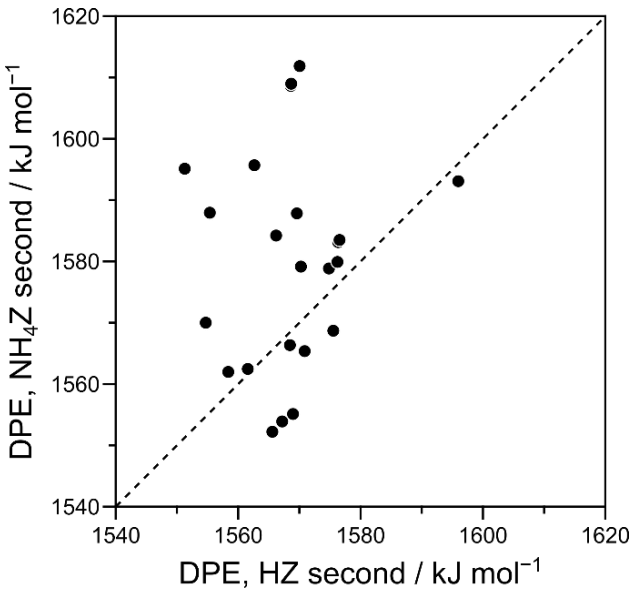


Figure 2-20. The relationship between DPE when the second site is protonated (HZ) or when ammonia has adsorbed onto the second site (NH₄Z). The dotted line represents parity between DPE where the second site is protonated and when NH₃ is bound to the second site.

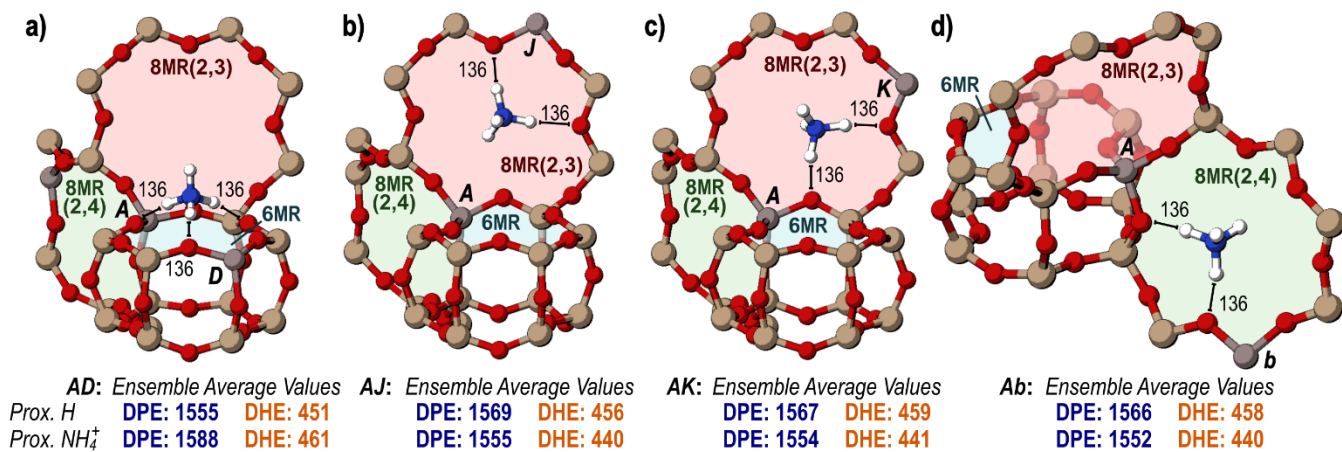


Figure 2-21. The anions of the **a)** AD, **b)** AJ, **c)** AK, and **d)** Ab site-pairs with NH₃ adsorbed to the second site. Distances between H of the NH₄⁺ and framework O atoms are shown in pm. Ensemble average DPE and DHE values when a H is on the second site and when NH₃ has adsorbed to the second site are shown below each structure in kJ mol⁻¹.

DHE can be measured with NH₃ bound to the second site. Much like DPE, the dehydrogenated A site is stabilized more strongly by nearby sites who share an 8MR. The AC, AD, and AE site-pairs have DHE of 470, 466, and 483 kJ mol⁻¹, all higher than the DHE of the isolated site, when the DHE of AC and AD with a proton on the second site were lower than the DHE of the isolated site. The DHE of the AI (448 kJ mol⁻¹), AJ (445 kJ mol⁻¹), AK (445 kJ mol⁻¹), Aa (440 kJ mol⁻¹), and Ab (448 kJ mol⁻¹) site-pairs were all reduced by the presence of NH₃ on the second site and all site pairs share 8MR. DHE with NH₃ adsorbed to the second site trends strongly with DPE with NH₃ adsorbed to the second site (see Appendix A). Again, the perfect parity between the DPE and DHE seen on the isolated site disappears because of the confounding effects of the nearby NH₄⁺ cation on the second acid site, which similarly affects the EA of the conjugate bases.

Two adsorbed ammonia are most stable when the first is adsorbed to O4 of the A site and the second is adsorbed to O1 of the D site. The ammonium cation on the A site, when on O4 in the 8MR(2,4) is additionally stabilized by the presence of the D site in that ring, which appears due to periodic boundary conditions. The two anionic sites in the 6MR can interact simultaneously with the ammonia adsorbed to O1 of the D site, allowing the cation to orient itself closer to the plane of the ring, rather than the unfavorable interactions of the adsorbed ammonia with the 6MR in the isolated acid (Figure 2-7 a). Because these larger adsorbed species interact differently and over longer distances, orientations of ammonia that were unfavorable on the isolated acid and when the second site was protonated can become favorable.

NH_3 binds most favorably to O4 of the *A* site when there is NH_3 is on O2 of the *W* site (-214 kJ mol^{-1}). Ensemble average NH_3 BE values indicate that NH_3 binds more weakly to the *AC* (-139 kJ mol^{-1}), *AD* (-156 kJ mol^{-1}), and *AE* (-126 kJ mol^{-1}) than sites separated by longer distances which share 8MR rings with the *A* site, as in the *AI* (-163 kJ mol^{-1}), *AJ* (-165 kJ mol^{-1}), *AK* (-161 kJ mol^{-1}), and *Ab* (-164 kJ mol^{-1}) pairs. Ensemble average values for NH_3 BE also trend linearly with DPE when calculated with NH_3 on the second site (Figure 1-18 b). Arithmetic averages over the location of the first NH_3 indicate that the second NH_3 still generally prefers to bind to O4, with an average adsorption energy of -157 kJ mol^{-1} and least prefers to bind to O1, with an average adsorption energy of -140 kJ mol^{-1} (Figure 2-10 b).

The average difference between all metrics of acid strength (DPE, DHE, and NH_3 BE) for the isolated site and for a site-pair gives is used to give a broad view of how a second proximal site can increase, decrease, or have little effect on Brønsted acid strength. Most site-pairs which do not share a ring, or which share a 4MR, are weakened or unaffected by proximity, regardless of the state of the second site (bare or with NH_3 adsorbed; Table 2-2). Acid sites with a neighbor within the same 6MR are strengthened when the second site is bare but weakened if the second site has NH_3 adsorbed to it. Sites sharing an 8MR can only be strengthened by a bare proton when they are separated by 1 Si T-site, and only site-pairs sharing an 8MR are strengthened by the presence of NH_3 on the second site.

Table 2-2. Acid sites can be weakened, unaffected, or strengthened when a second site is placed in varying positions as a bare proton or with NH₃ adsorbed.

		<i>Proximal H+</i>	
	Weakened (5) ^b	Unaffected (11)	Strengthened (6)
<i>Proximal</i> <i>NH₄⁺</i>	Weakened (14)	AW (NR, 2) ^c	AE (6MR, 1)
		AZ (NR, 2)	AN (4MR, 1)
		AU (NR, 2)	AP (NR, 2)
		Ac (NR, 2)	AS (4MR, 1)
		AT (4MR, 1)	AY (NR, 2)
	Unaffected (4)	Ad (NR, 2)	
		AQ (8MR, 3)	AI (8MR, 2)
	Strengthened (5)	AL (8MR, 1)	AH (8MR, 1)
		--	AJ (8MR, 3)
			AK (8MR, 2)

Site-pairs within 6MR structures can be selectively synthesized, titrated, and their rates thus independently calculated from isolated sites as shown for CH₃OH dehydration.^{19,66} This work demonstrates the abilities of site pairs in 6MR and 8MR motifs to be stronger acids, depending on their specific arrangement and the adsorbates bound to them. These results can give insights into the enhanced reactivity of increased rates of methanol dehydration on paired sites in CHA.¹⁹ The 3, 6, and 8MR structural motifs that influence these changes in acid strength with varying Al position also exist in many other zeolite frameworks,^{122,132} and Al sites are likely to interact over these similar structural arrangements in many frameworks that contain 6 and 8MR motifs.

Inhibition of Methanol Dehydration Rates on Small-Pore Zeolites

Methanol dehydration turnover rates (415 K, per H⁺) on CHA zeolites containing predominantly isolated H⁺ sites increase linearly with methanol partial pressure (P_{CH₃OH}) at low partial pressures (<1 kPa), before reaching a maximum and transitioning to a kinetic regime reflecting inhibition at high partial pressures (>10 kPa) (Figure 2-22). This behavior is not captured by the form of the associative dehydration rate law derived

assuming H⁺ sites are covered by methanol monomers and protonated dimers as most abundant surface intermediates (MASI) (Eq. 2-12).⁴⁷

$$r_A = \frac{k_{DME,A} K_D P_{CH_3OH}}{1 + K_D P_{CH_3OH}} \quad (2 - 12)$$

In Eq. 2-12, k_{DME,A} is the rate constant for DME formation via the associative mechanism, K_D is the equilibrium constant for forming a protonated dimer from a gaseous methanol and adsorbed methanol monomer, and P_{CH₃OH} is partial pressure of methanol. In situ IR spectra measured under conditions of methanol dehydration catalysis (415 K, 0.05-20 kPa) detected methanol monomers (~2400 cm⁻¹) and dimers (~2600 cm⁻¹)¹⁰¹, and vibrational modes for methanol clusters (~3370 cm⁻¹)¹³³ at high methanol partial pressures (>10 kPa).²¹ Including methanol trimers as a MASI introduces a second-order methanol pressure term in the denominator of the associative dehydration rate law (Eq. 2-13), which is able to describe the rate inhibition measured at high methanol partial pressures (Figure 2-22, solid line).²¹

$$r_A = \frac{k_{DME,A} K_D P_{CH_3OH}}{1 + K_D P_{CH_3OH} + K_1 K_D P_{CH_3OH}^2} \quad (2-13)$$

In Eq. 2-13, K₁ is the equilibrium constant for forming a methanol trimer from a gaseous methanol and adsorbed protonated dimer. Before using Eq. 2-13 to describe methanol dehydration rates on CHA zeolites, we first examine and discard other mechanistic assumptions that would also predict high-pressure kinetic inhibition, by considering other plausible intermediates and rate laws derived from the dissociative mechanism that do not consider surface methoxy as a MASI, since such species are not detected by in situ IR spectra of CHA zeolites (Si/Al = 15) containing isolated H⁺ sites.²¹

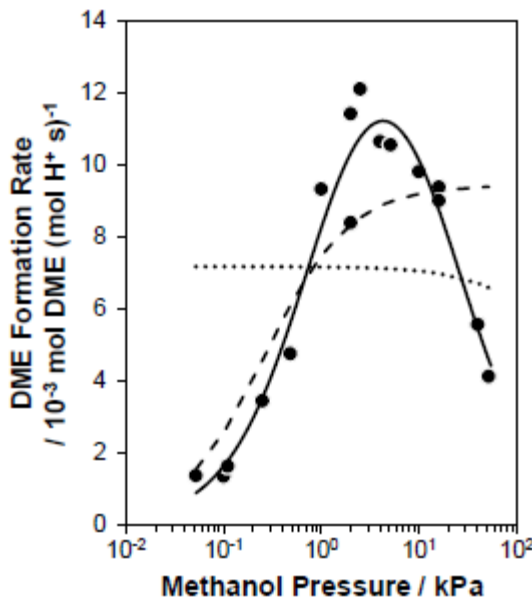


Figure 2-22. Least-squares regressions of Eq. 1-13 (solid line), Eq. 1-15 (dotted line), and Eq. 1-16 (dashed line) to experimentally measured methanol dehydration rates (per H^+ , 415 K) on a H-CHA (Si/Al = 15) sample containing predominantly isolated H^+ sites.

An alternate rate law can be derived for the dissociative mechanism, assuming methanol monomer dehydration to form methoxy intermediates is the kinetically relevant step, and that H^+ sites, methanol monomers, and protonated dimers are the MASI (r_{D1} ; derivation in Appendix A-12):

$$r_{D1} = \frac{k_{Me}K_M P_{CH_3OH}}{1 + K_M P_{CH_3OH} + K_M K_D P_{CH_3OH}^2} \quad (2-14)$$

In Eq. 2-14, k_{Me} is the methoxy formation rate constant, and K_M is the equilibrium constant for forming a methanol monomer from a gaseous methanol and a vacant H^+ site. This expression predicts inhibition at high methanol partial pressures because protonated dimers are spectator species in the dissociative mechanism (Figure 2-1). This rate expression would require vacant H^+ sites to be a MASI, however, which is inconsistent with in situ IR spectra that show complete perturbation of bridging OH stretching vibrations ($\sim 3608 \text{ cm}^{-1}$) by adsorbates at low methanol partial pressures

corresponding to the first-order kinetic regime (<1 kPa CH₃OH, 415 K) [18]. The removal of vacant H⁺ sites as a MASl causes Eq. 2-14 to predict between zero-order and negative-order dependences on methanol pressure, resulting in a rate law (Eq. 2-15) that does not describe the first-order dependence of methanol dehydration rates at low pressures (Figure 2-22, dotted line):

$$r_{D1} = \frac{k_{Me}}{1 + K_M P_{CH_3OH}} \quad (2-15)$$

Another alternative rate law can be derived from the dissociative mechanism, assuming DME formation is the kinetically relevant step and all preceding steps are quasi-equilibrated, and that methanol monomers and protonated dimers are the MASl, in accordance with in situ IR spectra measured on CHA zeolites (Si/Al = 15) containing isolated H⁺ sites (r_{D2} ; derivation in Appendix A-12):

$$r_{D2} = \frac{k_{DME,D} K_{MMe} K_{Me} P_{CH_3OH} P_{H_2O}^{-1}}{1 + K_D P_{CH_3OH}} \quad (2-16)$$

In Eq. 2-16, $k_{DME,D}$ is the DME formation rate constant for the dissociative mechanism, K_{MMe} is the equilibrium constant for forming a methoxy-methanol pair from a surface methoxy and gaseous methanol, and P_{H_2O} is the gas-phase partial pressure of water, which is generated via methanol monomer dehydration to form a surface methoxy. This rate law predicts a first-order kinetic regime at low methanol pressures and a transition to a zero-order kinetic regime at higher pressures, but also predicts rate inhibition caused by hydration of surface methoxy intermediates. Eq. 2-16 was regressed to methanol dehydration rates (per H⁺, 415 K) measured on CHA zeolites containing isolated H⁺ sites, assuming that the gaseous water partial pressure is equal to that of DME formed from reaction (Figure 2-22, dashed line). The high-pressure

inhibition observed experimentally causes methanol conversion to decrease (Figure 2-23 a) faster than Eq. 2-16 would predict, indicating that the product water formed via methanol dehydration is unable to account for the measured inhibition (Figure 2-22, dashed line). Moreover, methanol dehydration rates do not depend on space velocity at fixed methanol pressure (per H⁺, 1 kPa CH₃OH, 5–30% conv.; Figure 2-23 b), as would be predicted by Eq. 2-16 because of the inverse dependence of methanol dehydration rates on water pressure (solid line, Figure 2-23 b; derivation in Appendix A-8). Methanol dehydration rates (415 K, per H⁺) were also measured after treating methanol reactants to remove any residual moisture and contaminants and were identical to those measured using unpurified methanol. Thus, any adventitious water present in the reactant methanol feed, or generated in situ as a reaction product, is not responsible for the observed inhibition at high methanol pressures.

DFT Assessments of Prevalent Methanol Dehydration Reaction Pathways

Prior to interpreting the mechanistic origin of high-pressure inhibition of methanol dehydration rates, we first use DFT to predict the free energy landscapes (Figure 2-24) of both the associative and dissociative mechanism at isolated H⁺ sites in CHA (1 bar, 415 K). For the associative mechanism, DME formation from a protonated dimer intermediate is the kinetically relevant (i.e., rate-determining) step, and DFT estimates a

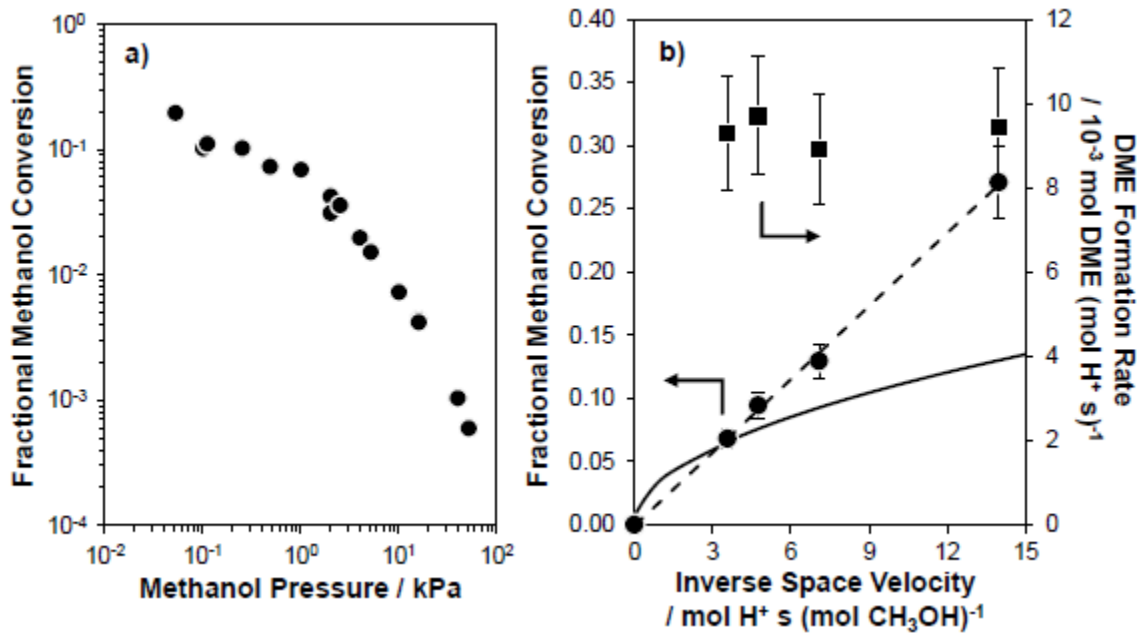


Figure 2-23. **a)** Fractional methanol conversion (415 K) on a H-CHA (Si/Al = 15) sample with isolated H⁺ sites as a function of methanol pressure, and **b)** fractional methanol conversion (circles) and DME formation rates (per H⁺, 415 K; squares) along with the predicted dependence from Eq. 7 (solid line) as a function of inverse space velocity.

zero-order free energy barrier ($\Delta G_{\text{zero}} = \Delta G_{\ddagger} - \Delta G_{\text{dimer}}$) of 137 kJ mol⁻¹ and first-order free energy barrier ($\Delta G_{\text{first}} = \Delta G_{\ddagger} - \Delta G_{\text{monomer}} - \Delta G_{\text{CH}_3\text{OH},g}$) of 123 kJ mol⁻¹ (Figure 2-24). For the dissociative mechanism, the first step methylates the zeolite surface with an intrinsic and overall barrier of 135 kJ mol⁻¹, while the second step involves methylating methanol to form DME with an intrinsic barrier of 77 kJ mol⁻¹ and an overall barrier of 130 kJ mol⁻¹ (Figure 2-24). Either of these steps could be kinetically relevant should DME form via the dissociative mechanism. Therefore, the kinetic fates of surface methoxy intermediates were determined by calculating ratio of the reverse rate of the first step (r_{D1}) to the forward rate of the second step (r_{D2}) as a function of conversion (details in Appendix A). The forward rate of the second step is >10x faster than the

reverse rate of the first step below 30% conversion, corresponding to the highest value tested in this work (Appendix A-12), and causes the first step to become kinetically relevant at these conditions.

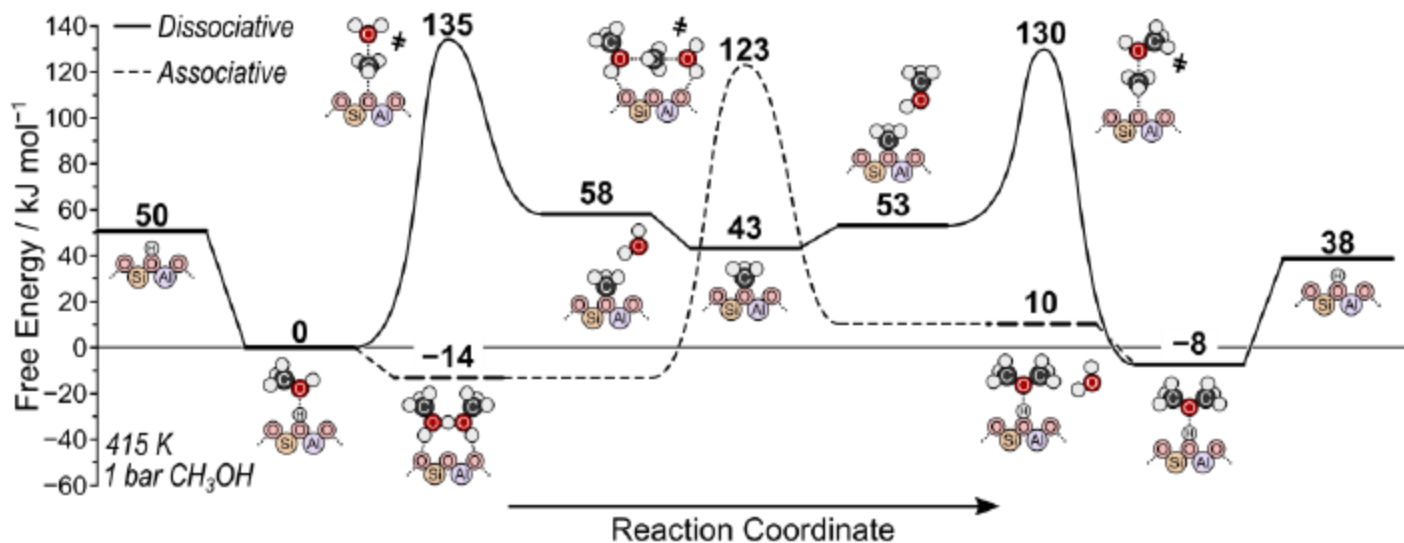


Figure 2-24. Reaction coordinate diagram showing DFT-calculated free energies (ΔG ; kJ mol^{-1}) of intermediates and transition states involved in methanol dehydration on isolated H^+ sites in CHA at 415 K and 1 bar of CH_3OH .

The reaction coordinate diagram in Figure 2-24 was constructed after carefully examining each intermediate and transition state structure to identify their most stable configurations, using systematic reorientations of initially converged structures to more comprehensively probe the configurational space accessible within zeolite voids [54]. The first step of the dissociative mechanism involves surface methylation transition states that are stabilized by 8-MR structures, in which H atoms of hydroxyl groups form H-bonds to lattice O atoms (Figure 2-25 a). Surface methylation transition states preferentially interact with O₃ of the conjugate base and form two H-bonds to O atoms in the 8-MR, in which O₃ is located (192 and 194 pm, Figure 2-25 a). The most

favorable surface methylation transition states at O4 and O2, which are also in 8-MR, are 13 and 18 kJ mol⁻¹ higher in energy, respectively, indicating the strong preference for the transition state geometry at O3 for surface methylation. The transition state at O1 is 38 kJ mol⁻¹ higher in energy than that at O3, as this transition state is not solvated by surrounding framework atoms, because it is instead located in the larger CHA cage void, which confers weaker dispersive stabilization.

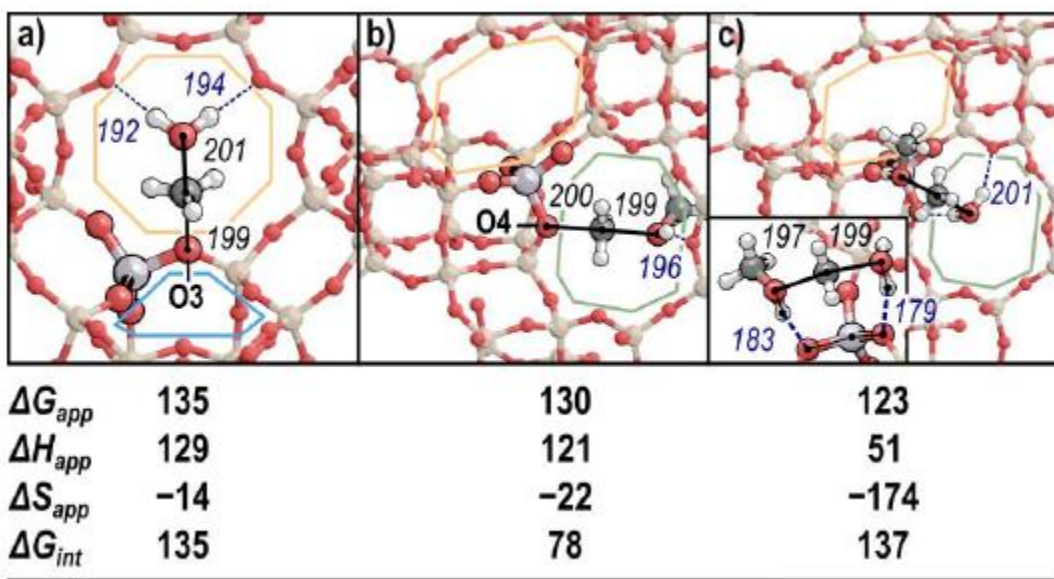


Figure 2-25. The most favorable transition state found in CHA for **a**) surface methylation (the first step of the dissociative mechanism), **b**) methanol methylation (the second step of the dissociative mechanism), and **c**) associative dimethyl ether formation. The O atom that the methyl group interacts with in **a**) and **b**) is labeled. Incipient bonds (black) and H-bonds (navy) are labeled in pm. Apparent (ΔG_{app}) and intrinsic free energy (ΔG_{int}) and apparent enthalpy (ΔH_{app}) barriers in kJ mol⁻¹, and apparent entropies (ΔS_{app}) in J mol⁻¹ K⁻¹, are shown relative to an adsorbed methanol. The 8-MR (orange, green) and 6-MR (light blue) adjacent to each transition state are highlighted.

The second step of the dissociative mechanism, in which another methanol accepts the surface methyl group, also occurs most easily in the 8-MR; however, this transition state forms preferentially at O4 of the conjugate base rather than at O3 (Figure 2-25 b). The methanol that accepts the surface methyl group forms one H-bond

to another O atom in the 8-MR that contains O4 of the active site. The reacting oxygenate species (CH_3OH) contains only one polar O–H bond instead of two (H_2O), resulting in less H-bonding capacity in this transition state than in the other two possible transition states that occur during methanol dehydration (Figure 2-25). Moreover, this H-bond is longer (196 pm; Figure 2-25 b) and weaker than the H-bonds formed in surface methylation (192 and 194 pm; Figure 2-25 a) and associative DME formation (179 and 201 pm; Figure 2-25 c) transition states. The associative transition state (Figure 2-25 c) is stabilized by 8-MR structures similarly to surface methylation transition states (Figure 2-25 a). The water leaving group formed at this transition state forms two H-bonds to framework O atoms in the 8-MR, one of which is O4 of the conjugate base and stabilizes partial charges of the transition state structure. Furthermore, the methanol that accepts the methyl group forms another H-bond to O3 of the conjugate base, again stabilizing the transition state and allowing for rapid surface protonation after DME is formed. These concerted H-bonding motifs form a ring of interactions as the methyl group is transferred from one oxygenate to another (Figure 2-25 c, inset), allowing for more effective charge distribution than is possible in either of the dissociative transition states. Moreover, H-bonding in the associative transition state occurs predominantly with O atoms of the conjugate base, which harbor more negative partial charge, resulting in shorter (181 pm on average in Figure 2-25 c; 193 and 196 pm in Figure 2-25) and stronger stabilizing interactions between reacting species and the zeolite surface. Maximum rate analysis was then used to predict rates of competing reaction pathways using these DFT-predicted free energy barriers, which are taken together with statistical mechanics formalisms (see Appendix A-11. for relevant formulas) to calculate

rate (k_i) and equilibrium constants (K_i), as described in previous work.^{52,134} The overall rate of a reaction pathway is taken as the rate of the slowest elementary step, identified from rates calculated by separately considering each elementary step to be the sole rate-limiting step. The fastest overall rates among different competing reaction pathways are used to identify prevailing reaction routes. Although the associative route occurs with an overall barrier 12 kJ mol⁻¹ lower than that of the dissociative route at 415 K (123 kJ mol⁻¹ overall; Figure 2-24), the resulting larger rate constant does not account for pressure effects on rates, requiring maximum rate analysis to assess competing dehydration pathways. The results of maximum rate analysis at 415 K and 0.1% conversion are shown in Figure 2-26 a, with rates of the associative pathway and of the first and second steps of the dissociative pathway shown as a function of methanol pressure. The second step of the dissociative pathway occurs at faster rates than the associative mechanism at all pressures considered here (0.01–100 kPa) (Figure 2-26 a), consistent with analysis of the reversibility of the first step that indicates it is the sole kinetically relevant step of the dissociative mechanism. The dissociative pathway dominates at pressures below 4 kPa at 415 K, which reflects the relative pressure dependences of rates for the associative and dissociative routes:

$$\frac{r_{D1}}{r_A} = \frac{k_{D1}}{K_A K_D P_{CH_3OH}} \quad (2-17)$$

This equation indicates that the dissociative route will dominate at sufficiently low methanol pressures, and that the prevailing reaction mechanism will shift to the associative route at higher pressures. Rates estimated by DFT predict this transition occurs at 4, 10, 23, and 63 kPa at 415, 433, 450, and 473 K, respectively. This shift reflects entropic and enthalpic preferences for these routes, in which the adsorption of a

second methanol in the associative route confers enthalpic gains but concomitant entropic losses that preferentially benefit the dissociative mechanism at high temperatures and low pressures. This is consistent with prior work on MFI zeolites^{48,66,101} and POM catalysts⁴⁷, which indicate similar behavior for these mechanisms with different kinetic conditions.

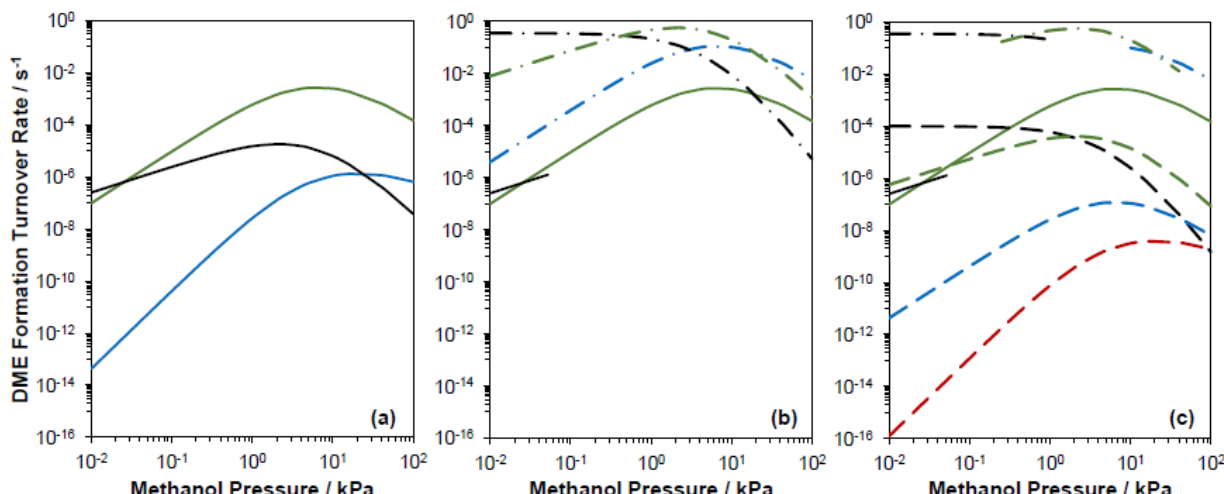


Figure 2-26. DFT-predicted rates (415 K) with zero (black), one (green), two (blue), or three (red) spectating methanol molecules for **a**) the associative mechanism (solid lines), **b**) kinetically-relevant DME formation of the dissociative mechanism (dashed-dotted lines), and **c**) kinetically-relevant methoxy formation of the dissociative mechanism (dashed lines) at 0.1% CH₃OH conversion. The maximum predicted rates of the associative mechanism (solid lines) are shown in **b**) and **c**) and of kinetically-relevant DME formation of the dissociative mechanism (dashed-dotted lines) are shown in **c**) for comparison.

Conclusion

The proximity of Brønsted acid sites in zeolites alters their strength. This is predicted by DPE, DHE, and NH₃ BE calculations for 23 arrangements of proximal acid sites with varied Al–Al distances in the CHA framework, which has a single crystallographically unique T-site, indicating that all changes in acid strength predictions are related to proximity and not variations in acid site location. Rough correlations were observed between DPE, DHE, and NH₃ BE predictions across all proximal acid sites.

Deprotonation of an acid site forms an anionic conjugate base that can be stabilized via H-bonding, dipole-dipole, and electronic interactions by a nearby proton placed 1–2 linking Si atoms away in specific locations that facilitate such interactions. Acid sites which coexist within 6MR structures of CHA show the greatest enhancement to acid strength, with decreases in ensemble average DPE values of 13–17 kJ mol⁻¹, caused by H-bonding between the conjugate base AlO₄⁻ and the proximal proton of the second site. These interactions stabilized some conjugate base structures with Al separated by 1–2 linkers in 8MR arrangements, resulting in slight decreases to DPE values (6–13 kJ mol⁻¹). Brønsted acid sites separated by 1 Si T-site and arranged across a specific 4MR of CHA resulted in very stable protons, and the inability of the residual proton to stabilize the conjugate base results in a calculated DPE value that is ~30 kJ mol⁻¹ higher than that of an isolated site, indicating a significant weakening of the acid; this is the only such arrangement of Al atoms that resulted in an increase in DPE of > 10 kJ mol⁻¹. Other sites had weak impacts on DPE, with roughly half of all proximal acid sites shifting DPE values by < 5 kJ mol⁻¹ relative to isolated species.

Brønsted acid sites are rarely unoccupied during catalysis at practical conditions as protons are typically covered by H-bonding species (e.g., CH₃OH, H₂O), reacted to form surface-bound alkoxides (e.g., CH₃–Z), or deprotonated by a nearby base (e.g., NH₃). Thus, the impact of bare protons on the acid strength of proximal sites may be mitigated by the presence of an adsorbate on that site (e.g., NH₃, CH₃OH) or by the free energy required to desorb that species from the proximal site prior to reaction. A proximal site titrated with NH₃ (forming an NH₄⁺ cation) was, for most cases, significantly less capable of stabilizing the conjugate base structure of a nearby acid

site, thus the adsorption of NH₃ to a proximal site increased DPE values of the deprotonated site by 11 kJ mol⁻¹, on average. This shift completely reverses the effects of proximity on acid strength for sites separated by 1–2 Si in 6MR structures, with DPE values proximal to a second site that is titrated by NH₃ being > 20 kJ mol⁻¹ higher than those for isolated sites. The NH₄⁺ cations present on the second site are not capable of H-bonding to the anionic conjugate base of the first site when these sites are in the same 6MR. Sites separated by 2–3 Si atoms in the 8MR, however, have conjugate base structures that are stabilized by the NH₄⁺ cation (which resides in the plane of the 8MR and H-bonds to both Al sites simultaneously), and these stabilizations result in DPE values that are > 10 kJ mol⁻¹ lower than isolated sites, indicating a stronger acid.

Anionic conjugate base structures of deprotonated acid sites are thus stabilized by proximal protons on Al sites nearby (1–2 sites) and across small voids (6MR) which stabilize protons and by proximal NH₄⁺ cations on Al sites greater distances away (2–3 sites) and across larger voids (8MR) which stabilize NH₄⁺ cations. Specific influences of acid site proximity on reaction rates, therefore, will depend on the intervening distances and nature of the voids over which the sites are separated, the state of the second site, and the nature and size of the cation being formed by relevant transition states involved in the reaction.

CHAPTER 3
ReO_x PROMOTIONAL EFFECTS ON BIMETALLIC CATALYSTS FOR THE PURPOSE
OF HYDROGENOLYSIS

Selective C–O cleavage of biomass-derived alcohols is critical to their transformation into value-added chemicals (while complete deoxygenation is desired for fuels). Oxophilic metal promotores such as ReO_x, WO_x, MoO_x, RuO_x, have been shown to increase C–O hydrogenolysis rates and alter product distributions for a variety of hydrogenolysis reactions.^[R] Most studies have focused on aqueous phase reactions, which complicate kinetic studies and mechanistic analysis because of the ubiquitous role of H₂O in chemical reactions (as a solvent, reactant, and co-catalyst). Here, we have examined the effects of ReO_x-promotores on Pt and Au catalysts for C–O hydrogenolysis of glycerol (a bio-diesel byproduct) and ethanol (a volatile fermentation product suitable for gas and liquid phase comparisons). These reactions are studied in aqueous and gas-phase flow and batch reactors with and without co-fed water.

Pt (5 wt. %) and Pt-ReO_x (5 wt. % of both metals) were impregnated on activated carbon (Norit SG-1), additionally, Au (1 wt. %) and Au-ReO_x (1 wt. %, 3 wt. %) were prepared on CeO₂ supports. Aqueous phase reactions are carried out in a batch reactor (1 wt. % alcohol, 473 K, 4.0 MPa H₂). The ReO_x promotion during glycerol reactions on Pt-based systems increased rates by a factor of ~10 (normalized by Pt-surface atoms) and shifted selectivity from 1,2-propanediol (72%) and ethylene glycol (19%) to 1,3-propanediol (18%), 1,2-propanediol (20 %), and 1- and 2-propanol (61 %). Observed selectivity and rate shifts indicate that ReO_x facilitates C–O activation and enables C–O activation at secondary positions of the C₃ backbone. This result is consistent with prior studies²⁻⁴ and consistent with work suggesting that ReO_x promotores incorporate Brønsted acid sites into the catalyst. These Brønsted acid sites catalyze dehydration

reactions (with a preference towards secondary C–O activation because of enhanced carbenium ion stability) and any unsaturated compounds formed via dehydration are rapidly converted to saturated alcohols on Pt at these high H₂ pressures (4.0 MPa). ReO_x increases Pt-based reaction rates by ~3 and shifts selectivity away from diethylether (formed by condensation) and towards gas-phase ethane formation for ethanol. Preliminary data gathered in a gas-phase flow reactor (neat ethanol feed, no water) shows rates > 10-times higher on Pt-ReO_x than the unpromoted Pt catalyst and (as was observed in aqueous phase) shifts selectivity away from diethylether and towards C–O cleavage products. This indicates that liquid H₂O is not required to enable ReO_x to promote C–O hydrogenolysis rates, additional studies which will co-feed water and ethanol vapor will further elucidate the role of H₂O in this reaction.

Au-based catalysts, in contrast to Pt, are ineffective at hydrogenation; thus, dehydration chemistry on Brønsted acid sites (formed by ReO_x) should yield unsaturated compounds and avoid complete deoxygenation (as C₃ dienes are very unstable). Such hypotheses were confirmed here, with glycerol showing no reactivity on mono-functional Au/CeO₂ catalysts while Au-ReO_x/CeO₂ produced prop-2-en-1-ol at high (> 90%) selectivity, indicating that C–O cleavage can occur solely on bifunctional Au-ReO_x sites (ReO_x alone is not reactive) and that it forms, as primary intermediates, unsaturated compounds (indicative of Brønsted acid reactivity). The consequence of phase and the presence of H₂O on these Au-catalyzed reactions is currently being examined.

Introduction

The increased demand of energy for transportation, residential, and commercial use is being facilitated by a growing population especially as large nations, like India

and China, become modernized and they use dramatically more energy.¹ There are many approaches to try and remedy these problems, one such innovation is biomass conversion—repurposing waste to higher market value chemicals. Biomass conversion has been around for millennia; from burning wood or fuels for heat and/or charcoal to the production of alcohols by fermenting plants and fruits.^{135–138} However, industrially it was not until the 1970's where sugars/starches were used to make ethanol or oils from seeds and plants were converted to biodiesel.^{26,139,140} Specifically, growing fields and crops to produce ethanol or fuels creates a carbon neutral cycle since the carbon in the fuels comes from atmospheric CO₂ the plants photosynthesize¹⁴¹. Unfortunately, this can have side-effects such as making soil less fertile over time, upsetting the trade and cost of food markets for farmers and consumers¹⁴¹, and there are still left-over products like lignin, which are hard to re-purpose efficiently^{142,143}. There exist a variety of methods that yield C₁₃ range species which ultimately form components in diesel fuel, and instead uses oils that would have been disposed of otherwise and not directly from crops.^{139,144–146}

Different approaches exist for this process of converting triglycerides to diesel such as a pyrolysis or hydrotreating triglycerides. Pyrolysis uses hydrogen at elevated temperatures (500–1000 K) and pressures (> 1 MPa), which forms propane, three additional alkanes and CO₂.^{147,148} Solvent liquification is also a promising route because this is performed at lower temperatures (300–600 K) and it is possible to extract more temperature sensitive compounds like propanediols that can be valuable; however, non-environmentally friendly solvents are used.^{146,149–152} Alternatively, transesterification can be used to yield the desired bio-products without using the other techniques like

pyrolysis (requiring high temperatures) or emulsions (requiring solvents).

Transesterification of triglycerides in the presence of methanol yields C₁₃ range species that ultimately form components in diesel fuel as well as glycerol (Figure 3-1).^{139,146} The catalysts often used for transesterification reactions are wide ranging but include alkali, acid, enzyme or heterogeneous catalysts, among which alkali catalysts like sodium hydroxide, sodium methoxide, potassium hydroxide, potassium methoxide are more effective.^{3,140,146}

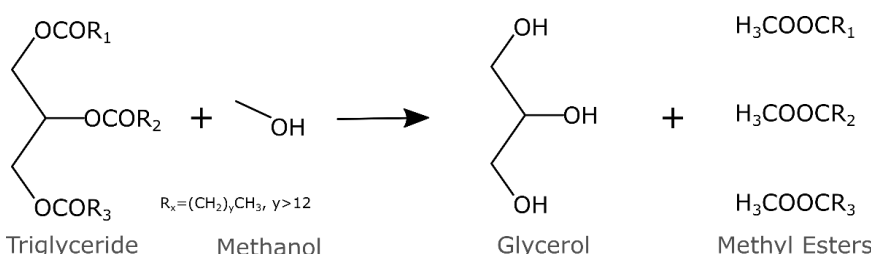


Figure 3-1. Transesterification of triglycerides in the presence of methanol to form methyl esters and glycerol

Glycerol is a highly functionalized molecule, having an –OH bond on each of its 3 carbons, but this leads to it being viscous and having a low vapor pressure.¹⁵³ Above 540 K glycerol can be converted to syngas^{147,148} or burned for energy, but it is only 30% efficient (when accounting for energy required for heating, pumping, and pressurizing).¹⁰ Currently, the market is over saturated with glycerol 22.7 million metric tons of glycerol were produced in 2012; however¹⁵⁴, its main industrial uses (sweetener and lubrication)^{140,151,153} account a fraction of the glycerol produced^{150,154}. Converting glycerol into value added commodity products would be advantageous; glycerol conversion can be accomplished through steam reforming, oxidation, dehydration, acetalization, esterification, etherification, carboxylation, and chlorination—all of which produce a wide distribution of products.^{139,151,155–157} This creates a vast number of products but here we will focus on glycerol hydrogenolysis. Molecules that are similar in

nature are especially valuable for a wide variety of application; here is a list of most common products formed from glycerol reactions under a variety of conditions and catalysts: 1,3-propanediol, 1,2-propanediol, 1-propanol, 2-propanol, ethylene glycol, propane, ethane, methane. All these products can be used as monomers for polymers, for solvents, or for energy.^{158–162}

Typically, polyols have higher market value. The overall reaction from glycerol to 1,3- and 1,2-propanediol and ethylene glycol require a secondary C–O cleavage, a primary C–O cleavage, and a C–C bond cleavage, respectively. Transition metals such as Rh, Pt, Pd, Ru, Ir, Cu, and Ni (sometimes ReO_x, MO_x, and WO_x promoters are added) are used on various supports and are often thought to perform both dehydration and rehydration reactions to create diols.^{25,157,163–166} For example, the production of 1,2-propanediol can exhibit selectivities of >90% for over a dozen Cu-based metal catalysts.^{153,167} Glycerol hydrogenolysis has a preference to undergo primary C–O cleavage however this trend not seen in polyols such as 1,2,4-butanetriol or larger where the secondary C–O cleavage is preferred.²⁵

Multiple groups and mechanisms have been proposed for glycerol conversion. For example, there are ways in which the glycerol could align itself over the metal surface and react; the primary alcohol is deprotonated, a radical is formed at the primary –OH which is eliminated by a hydride transfer.^{168–171} However, the pathways could also use either Lewis or Brønsted acid sites to facilitate these reaction steps. Liquid phase reactions performed on Zn-Cr, which makes a Lewis acid site, yielding selectivities to acetol of around 40% indicating Lewis acids can form acetol, the precursor to 1,2-propanediol.¹⁷² Also, a Brønsted acid catalyst can form acetol by the

direct dehydration then subsequent ketoenol tautomerization. It has generally been accepted that glycerol is turned into acetol via a dehydration step at an acid site, then it is further hydrogenated to 1,2-propanediol at a transition metal site.^{25,153,167}

In many applications, oxyphilic metal promotion can increase conversion and turnover rate, alter selectivities, and alter product yields. Previous work has proposed that Ir-ReO_x catalysts form 1,2-propanediol in a single step via regioselective hydride attack of glycerol (Figure 3-2 a).^{158,159,173} A primary –OH interacts with the Re metal, where H⁻ is transferred from the alcohol to the Ir surface, a hydride transfer attacks the other primary alcohol resulting in water leaving. Bimetallic catalysts with oxyphilic metal promotion can facilitate new reaction mechanism compared to the monometallic case, however other species can now form because the new catalytic environment.^{152,157,158,163,164}

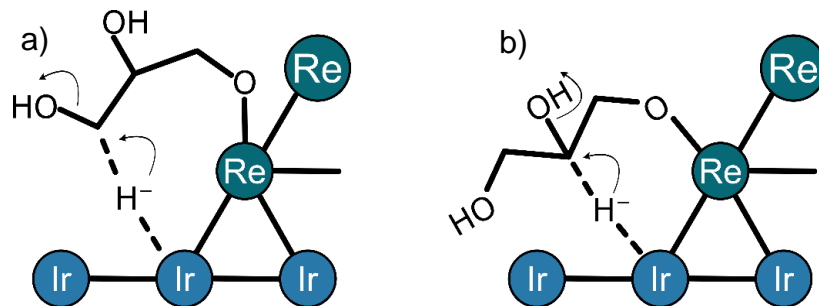


Figure 3-2. Proposed transition state for a single step conversion from glycerol to a) 1,2-PDO and b) 1,3-PDO via a hydride transfer adapted from reference ^{158,160}.

The formation of 1,3-PDO is thought to occur by protonating the secondary –OH, forming a H₂O⁺ complex which is, removed with a H from a primary carbon, a hydrogen shift occurs moving the double bond to the activated primary C–O bond, subsequent hydrogenation of the primary alcohol results in 1,3-PDO (Figure 3-3). Furthermore, it has been demonstrated through experiments, NH₃ TPD, and DFT that RhReO_x acts as

a Brønsted acid.^{22,157} The NH₃ TPD bound to the ReO_x sites with a standard enthalpy of -100 kJ mol⁻¹ and the DFT results indicate the hydroxyls have acidic protons which participate in the reaction.²⁵ The proposed mechanism involves substrate adsorption onto the surface of ReO_x cluster at the -CH₂OH-CH₂OH group to form terminal alkoxide. Next, hydride activated on the Rh metal attacks the 2-position of the alkoxide to break the C–O bond. The hydrolysis of the reduced alkoxide releases the product. The proposed structure of the transition state of the glycerol hydrogenolysis to 1,3- and 1,2-PDO is shown in Figure 3-3.^{22,157} ReO_x/C in H₂ and PtReO_x/C in air exhibits a Re oxidation state of +7, however, PtReO_x/C in H₂ as an oxidation state of Re slightly above of +2.¹⁶³

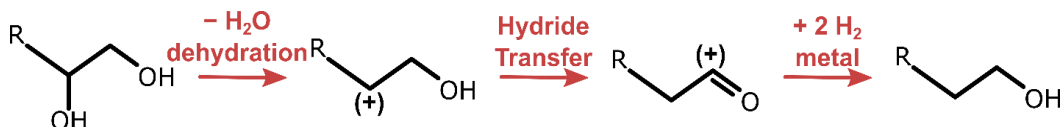


Figure 3-3. Proposed mechanism for the formation of 1,3-PDO resulting from the hydrogenolysis of glycerol adapted from reference^{22,157}.

Ethylene glycol is the result of C–C cleavage which has been demonstrated on multiple metal catalysts; Pt, Ru on multiple supports created 10% selectivity towards ethylene glycol.^{161,164,174} It was shown that Au catalyst are poor at hydrogenation, and the addition of Au to Cu/Al₂O₃ inhibited ethylene glycol formation (no C–C cleavage).^{175,176} Secondary products, such as C₁-C₃ alcohols and alkanes, can be formed by repeating a series of C–C and C–O cleavages. Au will produce unsaturated compounds like allyl alcohol and propylene.^{176–178}

Glycerol is viscous and has a higher vapor pressure than other alcohols its size; using ethanol as another alcohol in this study is advantageous because it is volatile, has

a primary C-O bond, and forms non-viscous products making it ideal for gas phase studies.^{54,179–182} Furthermore, the effects of water on the kinetics can be studied in vapor phase as the inlet can flow pure ethanol to mixtures of ethanol/water. The vapor phase also would allow for titration studies to help count the ReO_x sites as well as further elucidate Bronsted acid mechanisms.

Here we investigate the role that ReO_x promotion plays on hydrogenolysis reactions by running reactions under high H₂ pressure (1.0-4.0 MPa) on Pt/C, Pt-ReO_x/C, Au/CeO₂, and Au-ReO_x/CeO₂. Glycerol and ethanol are used as reagents in concentrations of 1 wt. % in aqueous phase water, and were analyzed using a GC, a GC-MS, and an HPLC. Ethanol was used because of its higher vapor pressure compared to glycerol making it more facile to work with in the vapor phase. The effects of water on this reaction was tested by running ethanol in a continuous flow packed bed reactor in the vapor phase where we could vary the inlet reagent from neat ethanol (99.95% pure) to ethanol water mixtures of varying mol percent.

Methods

Catalyst Synthesis

Pt / C

Platinum (5 wt. %) on a carbon support was prepared via an incipient wetness impregnation. Chloroplatinic acid hexahydrate (H₂PtCl₆*6H₂O, >37.5 ± 3.0 wt.% Pt) (Sigma Aldrich, CAS: 18497-13-7) was opened, immediately weighed, and a known amount of water was added and stirred to create a solution. A concentrated stock solution of the hydrate was created to eliminate uncertainties in precursor weight. The impregnation took place on activated carbon (Norit SX-1G), with a BET surface area of 1000 m²/g. The carbon was dried overnight in a muffle at 383 K to remove water. An

incipient wetness factor of 1.8 was used to dilute the concentrated chloroplatinic solution which was added drop wise via incipient wetness techniques to the carbon; the weights of the dried support and pre-cursor solution were adjusted such that 5 wt.% was Pt. The wet catalyst was placed in a muffle for 12 hours at 383 K which was transferred to a reduction furnace. The furnace was purged for 15 minutes with He (Airgas UHP, >99.9999%) at 70 mL min⁻¹, then the inlet gas was switched to H₂ (Airgas UHP, >99.9999%) for the reduction. The catalyst was heated to 723 K at a rate of 0.5 K min⁻¹, was held there for 3 hours, and was cooled to room temperature while still under the flow of H₂ at 70 mL min⁻¹.

Pt - ReO_x / C

The platinum (5 wt. %) and rhenium (4.9 wt. %) on a carbon support catalyst was prepared via an incipient wetness impregnation. The chloroplatinic acid hexahydrate solution (from previous section) and a perrhenic acid solution (HReO₄, 50-54 wt. % Re) (Strem Chemical: 13768-11-1) were weighed and added drop wise via incipient wetness to the dried carbon (Norit SX-1G) with the same incipient factor of 1.8 such that the Pt was 5 wt. %, and the Re:Pt had a 1:1 molar ratio. The catalyst was dried for 12 hours in a muffle at 383 K and underwent previously described reduction (rate 5 K min⁻¹, held at 723 K for 3 hours, cooled to ambient, using H₂).

Au / CeO₂

Hydrogen tetrachloroaurate (III) hydrate (HAuCl₄·3H₂O, 99% Au) (Acros Organics: 27988-77-8) was dissolved in DI water that was further purified (Thermo Scientific Barnsted Micro Pure ST UV with 6 L Tank) to make a solution that was 0.185 mMolar chloroauric acid. A magnetically spun hot plate, fitted with a thermocouple in the solution beaker, was heated and maintained at 353 K. Lastly, cerium (IV) oxide (99.9%)

(Acros Organics: 1306-38-3) powder, which was dried overnight in a muffle (383 K), was added to the heated solution while being stirred by a magnetic bar; the weights were selected such that post-synthesis Au loading is 0.3 wt. % assuming all the gold from the precursor precipitated (11.9 mL H₂O, 0.0061 g chloroauric acid, 0.997 g CeO₂).

Over the course of 4 hours under constant mild stirring a stock solution of 0.1 M ammonia hydroxide (NH₃OH, 28-30%) (Acros Organics: 1336-21-6) in DI water that was further purified (Thermo Scientific Barnsted Micro Pure ST UV with 6 L Tank) was added dropwise to the solution. The ammonia hydroxide solution was used to maintain a pH of 8 which was measured using a pH probe (Apera PH7000). After 4 hours, an aspirator was used to filter (Fisher Brand, P4, medium-fine porosity, slow flow), wash (> 1 L of water), and dry the solution. The catalyst was placed in a muffle (383 K) overnight. Finally, the dried catalyst was placed in a calcination furnace and heated to 673 K (ramp 1 K min⁻¹, held for 4 hours) under air (Airgas: UHP, O₂ 21 mol %, balanced in N₂, >99.999%), and allowed to cool to ambient; yielding a 0.3 wt. % Au/CeO₂ catalyst.

Au - Re / CeO₂

Incipient wetness (Section: Methods – Pt-Re/C) was used to add Re to an Au/CeO₂ catalyst (Section: Methods – Au/CeO₂) to make Re (0.3 wt. %) – Au (1.0 wt. %) / CeO₂. The catalyst was dried in a muffle (383 K, 12 hours) and was placed in the reduction furnace. The furnace was purged for 15 minutes with He (Airgas UHP, >99.9999%) at 70 mL min⁻¹, then the inlet gas was switched to H₂ (Airgas UHP, >99.9999%). The catalyst was heated to 623 K at a rate of 0.5 K min⁻¹, was held there for 3 hours, and allowed to cool to room temperature while all under the flow of H₂.

Reactions

Parr 300 mL reactions

A modified Parr reactor (300 mL) with a 4848 controller as shown in Figure 3-7, was used to run aqueous phase reactions under H₂ pressure. Further images for the reactor setup are depicted in Appendix B Figure B-3. The desired catalyst was selected and dried overnight in the muffle at 383 K to remove any moisture. The catalyst was weighed and added to the 300 mL reactor. The sealed reactor was pressurized to 4 MPa of H₂ (Airgas UHP, >99.9999%), rested for 1 minute, then was slowly depressurized down to just above atmospheric pressure. This process was repeated five times to remove air and humidity from the reactor. On the fifth purge the reactor was vented down to 2 MPa and was heated at a rate of 6 K min⁻¹ to 473 K (reaction temperature) to re-reduce the catalyst; the resulting pressure would be 4 MPa.

The reagent solution was prepared by adding either 1 wt.% or 5 wt.% glycerol (C₃H₈O₃, >99%) (Sigma Aldrich: 56-81-5) or ethanol (C₂H₆O, 200 proof) (Sigma Aldrich: 64-17-5) in DI water that was further purified (Thermo Scientific Barnsted Micro Pure ST UV with 6 L Tank) to a resistance of < 18.0 MΩ x cm. 200 mL of the solution was added to the pre-solution vessel and the remaining solution was kept for analysis. An 1/8th inch dip tube runs from the top of the vessel towards the bottom so any inlet gas bubbles through the solution before collecting in the head space of the vessel and leaving. The solution was bubbled for 15 minutes under a low pressure and low flow of H₂. After 15 minutes, the pressure was increased to 2 MPa and the pre-solution vessel was heated to 473 K at a rate of 6 K min⁻¹.

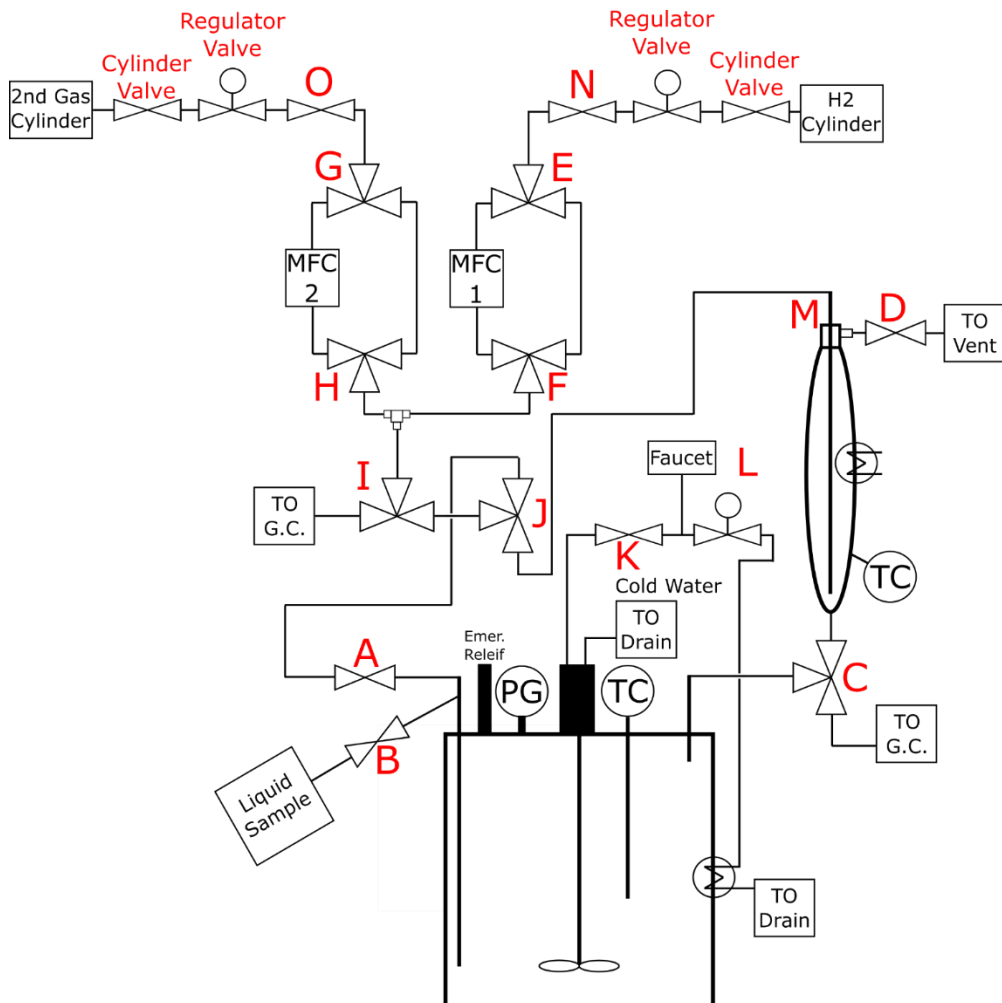


Figure 3-4. The schematic drawing of the reactor, with all relevant parts labeled.

Once the catalyst re-reduction is complete and the reagent solution is at 473 K, the reactor is vented down to just above the atmospheric pressure and the solution charges the reactor. Within 2 minutes of charging the reactor with the reagent, the temperature is maintained at 473 K and the pressure is run at either 1.0 or 4.0 MPa. Samples were taken at times (hours): 0, 0.3, 0.6, 1, 2, 4, 8, 12, 18, 24, and 30 via the liquid sampling port (Figure 3-4). Before every sample, the system is backfilled through inlet port (Figure 3-4) to 0.1 MPa above the system pressure to remove fluid in the dip tube. The excess pressure (+0.1 MPa) is reduced during sampling back to normal

system pressure. The first 1.0–1.5 mL of sample is collected in a waste container as it contains residual fluid. Approximately 2.5–3.0 mL of solution is collected for each sample. At 30 hours, the reaction is quenched with an internal water-cooling loop bringing the temperature down to atmospheric, the cooled reaction is vented down to ambient conditions. Prior to cleaning the reactor, a liquid sample of the retentate is taken for analysis. As the reactor is being vented a head space sample is often taken via a gas sampling syringe and the gas is qualitatively analyzed by the GC-MS for product identification.

Parr 50 mL reactions

A Parr 50 mL reactor was used to test the Pt, PtReO_x, Au and AuReO_x catalysts with 1 wt.% aqueous solutions of ethanol or glycerol in 4.0 MPa of H₂. On-line sampling was not performed on this reactor and instead the head space was analyzed post reaction to compute gas phase products and selectivities. The catalyst weight was determined by using a substrate to surface metal ratio of 350 while using 30 mL of solution. The catalyst was loaded in the reactor and filled to 4.0 MPa of H₂ (Airgas UHP, >99.9999%), held for a minute and slowly vented down to just above ambient pressure. This process was repeated 5 times to ensure all air and water were removed. The catalyst was re-reduced by pressurizing to 1.8 MPa and heating at a rate of 6 K min⁻¹ to 473 resulting in a pressure of 4.0 MPa. This reactor is held at 473 K for 2 hours and cooled.

The reagent solution was made in the same manner described in the section above, and once the reactor has cooled from re-reduction, the reactor is opened, and the solution is added quickly along with a magnetic stir bar. H₂ is bubbled through the solution catalyst mixture for 10 minutes around 50 mL min⁻¹, before the outlet is closed

and the system is pressurized to 1.8 MPa. Using heat tape and a house made PID temperature controller, the system is heated to 473 K at a rate of 10 K min^{-1} . The reaction is run for 30 hours, and the reactor is subsequently cooled to room temperature. The cooled head space (around 1.8 MPa) is sent through heated 1/16th inch lines to a Vici 10 port switch valve which directs the flow from the reactor to the FID and TCD in the GC-MS (explained in Methods Section GC-MS analysis). After depressurization to ambient pressure, a liquid sample is collected for HPLC analysis.

Continuous flow reactor

A continuous vapor phase packed bed reactor was constructed to perform reactions on the described catalysts (Figure 3-5). A tank of 5 mol% Ar balanced in Hydrogen was used as a feed hydrogen source, and an MFC was used to regulate the flow rate, and the pressure was kept downstream by a BPR controlled by an EPR (ProportionAir, PN: QB1SSNEEZP500PSG). An ISCO pump and Teledyne D-series controller were used to control the ethanol flow rate; ethanol was vaporized in the inlet stream. The catalyst bed is 1 inch in length and located in the center of the reactor. The remaining reactor volume is packed with quartz wool. The catalyst was diluted in CS-21 silica (2161) to ensure the 1-inch bed.

Reactions were carried out around 488 K with ethanol to H₂ molar ratios of 0.01–0.05, system pressures between 0.55–2.0 MPa, and flow rates between 50–300 SCCM. The product stream entered a Vici 10 port switch valve which directs the flow from the reactor to the FID and TCD in the GC (explained in Methods Section GC Analysis). Finally, the product stream exits to the fume hood through a bubble flow meter to find the flowrate.



Figure 3-5. The flow and instrumentation setup for the packed bed flow reactor.

Characterization and Analysis

H₂ chemisorption

Hydrogen chemisorption was performed on a Quantachrome AutosorbIQ (ASIQA3). The catalyst was prepared by heating at 4 K min^{-1} under H₂ (Airgas UHP, >99.9999%) to a reduction temperature of 773 K for all 4 catalysts (Pt/C, Pt/ReO_x/C, Au/CeO₂, Au/ReO_x/CeO₂), which was held for 1.5 hours. An evacuation procedure started as the sample was cooled to 308 K over the course of 2 hours and it was held there for another 2 hours under vacuum. The analysis took place at 308 K and ramped in pressure from 10-450 torr and the amount of H₂ uptake was estimated by linearly extrapolating the higher-pressure region of the adsorption isotherm to zero pressure. We assumed each hydrogen adsorbed on a single active site.

HPLC analysis

Liquid samples from the Parr 300- and 50-mL reactors were analyzed using a Waters Alliance HPLC (e2695) equipped with a RI (2414) and PDA (2489), and an ion exclusion column (Bio Rad Aminex HPX-87 H). Samples were filtered (Thermo Scientific Nalgene 0.45 um SFCA) and placed in a 3 mL sample vial (Waters, screw top with pre-slit PTFE/Silicon septa). 10 μ L of sample solution was injected into a 250 μ L sample loop with a mobile phase (5 millimolar $\text{H}_2\text{SO}_4/\text{H}_2\text{O}$) flow rate of 0.6 mL min⁻¹. Conversions (eq. 3-1 & 3-2), carbon balances (eq 3-3), selectivities (eq. 3-4), and rates (eq. 3-5 and 3-6) were calculated using the equation described in the below section (GC-MS Analysis).

GC-MS analysis

The GC-MS (Agilent: 7890N & 5977B) was used for analysis in all 3 reactors (300- and 50-mL Parr and the flow reactor) to qualitatively and quantitatively identify products. The unit is equipped with a Vici 10 port switch valve which directs the online flow to the 2 columns; a HP-1 (Agilent: 19091Z-215, 50m x 0.320 mm x 1.05 um) which leads to a FID and a capillary column (Agilent: Porapak Q, 6 feet, G3591-80013) which feed into a TCD. Manual injection can also be performed in 1 of 2 inlets. Gas phase samples are collected from the 300-mL Parr reactor and the flow reactor with a gas sampling syringe to help identify compounds.

The 50-mL Parr reactor is connected to the GC-MS via heated sampling lines that feed into the Vici switching port for on-line analysis for quantification of gas phase species. Conversion could be calculated two ways, each having different uncertainties associated with it:

$$x = \frac{C_{react.\ final} - C_{react.\ initial}}{C_{react.\ initial}} \times 100\% \quad (3-1)$$

Where x is the percent conversion, C is the concentration in mol L⁻¹ of the reactant at the initial and current time. This measures the depletion of the reagent used referenced to t=0, however alcohols especially polyols can often suffer from higher uncertainties in detectors like FID and TCDs at larger concentrations (>0.5 wt. %), which prompts the use of another metric to measure conversion.

$$x = \left(1 - \frac{NC_{react.\ final} \times C_{react.\ initial} - \sum_{i=1}^n NC_i \times C_i}{NC_{react.\ initial} \times C_{react.\ initial}} \right) \times 100\% \quad (3-2)$$

Where x is the percent conversion, NC represents the number of carbons in each species, C is the concentration in mol L⁻¹ for the species, and n is the number of products formed. The uncertainty of the reagent at t=0 is canceled because percent conversion is normalized by the moles of reactant at t=0. The products formed are all often at dilute concentrations (<0.1 wt. %) and offer more certainty in their peak areas than the reactant at another time intervals. Many of the batch reactions have rates and selectivities calculated at 10% conversion, interpolation was used to obtain these values unless otherwise noted.

The carbon balance was calculated using eq. 3-3;

$$C_{bal.} = \frac{\sum_{i=1}^n NC_i \times C_i}{NC_{react.\ initial} \times C_{react.\ initial}} \times 100\% \quad (3-3)$$

Where species i is the products or the reactant at time t, and C is the concentration in mol L⁻¹. Selectivities were calculated for each product as well;

$$S_j = \frac{C_j}{\sum_{i=1}^n C_i} \times 100\% \quad (3-4)$$

Where species j , is the product of interest, over all the products formed through n species, and C is the concentration. The instantaneous rates for each species were found using the following.

$$R = \frac{\Delta C_j}{\Delta t} \quad (3-5)$$

Rates (R) are calculated by taking the difference from the previous sample's (j) concentration and the current one (ΔC) over the time difference (Δt) in units of mols L⁻¹ s⁻¹ g⁻¹. Where the instantaneous rates are found by taking the difference of the concentrations from $t=0$ and the current time of interest.

$$R_{instantaneous} = \frac{dc_j}{dt} \quad (3-6)$$

The uncertainty in the initial data points is high because the concentrations are very dilute and there is a lower limit to what the detectors can analyze, thus there is higher errors associated with initial rates. Instead, rates and selectivities were analyzed by acquiring the time it took to deplete 10% of the reagent, then the linear slope from the time 0 data point and the data at 10% conversion is used as an averaged rate (Figure 3-6).

GC analysis

On-line samples from the flow reactor were analyzed using a GC (Agilent 6890 N) equipped with a Vici 10 port switch valve which directs the flow from the reactor to the FID and TCD. A schematic diagram of this setup can be found in Appendix B Figure B-2. Conversion was calculated using equations 3-1 and 3-2 and selectivity, carbon balance, and rates were calculated using equations 3-3, 3-4, and 3-5.

Results and Discussion

Catalyst Characterization – H₂ Chemisorption

Hydrogen chemisorption was used to estimate the number of active sites. The dispersion and assuming a 2:1 H:Site stoichiometry in combination with the catalyst loading (Table 2-1). H₂ adsorbed more favorably on the Pt (69 μmol H g⁻¹) catalyst than PtReO_x (30 μmol H g⁻¹). It should be noted that almost all the uncertainties came from the precursors; chloroplatinic acid came as a powder assayed at 37±3 wt. % Pt, and the perrhenic acid solution was assayed at 52±2 wt. % Re.

Table 3-1. The four catalysts of interest with their metal loading content and uncertainties. The strong isotherm of H₂ chemisorption was used to find H₂ uptake, dispersion (assuming 2:1 adsorption per site), and particle size.

Catalyst	Pt/Au Loading [wt. %]	Re Loading [wt. %]	H ₂ Uptake [umol H g ⁻¹]	Dispersion [%]	Particle Size [nm]
Pt/C	5.0+-0.4	-	69	28	3.9
PtReO _x /C	5.0+-0.4	4.9+-0.2	30	12.1	9.1
Au/CeO ₂	0.31+-0.02	-			
AuReO _x /CeO ₂	0.31+-0.02	1.0+-0.1			

Glycerol Hydrogenolysis

Effects of ReOx promotion on hydrogenolysis catalysts (Pt)

Glycerol (1 wt. %) (aq.) was reacted on Pt (5 wt. %) / C and Pt- (5 wt. %) Re (4.9 wt. %) / C catalysts under 4.0 MPa of H₂ pressure. Figure 3-6 shows the concentration of glycerol over time for the first 15 hours of the 30-hour run for 0.3 g of Pt based catalyst. Initial rates (eq. 3-6) and selectivities (eq. 3-4) are reported at 10% conversion based on the reagent depletion; the rate is the slope from the initial time to 10% conversion which in this case occurs at 8.6 hours (further normalized by catalyst weight) and we take the opposite sign because this is reagent depletion and not product

formation. A replicate of this catalyst was performed, and both of their results are compared in Table 3-2.

Two types of bond cleavages occur on Pt, C–C cleavage which creates ethylene glycol and a C–1 species as well as primary C–O cleavage which creates 1,2-propanediol and 2-propanol (Figure 3-8). Ethylene glycol is a primary product indicated by its non-zero intercept at 0% conversion and has a negative slope (Figure 3-7 a). 1,2-propanediol appears shortly after the reaction and increases over-time, which would indicate it is a secondary product. This discrepancy is likely because the amounts made at low conversion (1wt. % glycerol, @ 1% conversion = 0.01 wt. %). Furthermore, the sampling time is every 20 minutes and it is possible the conversion of 1,2-propanediol to 2-propanol is more facile than glycerol to 1,2-propandiol. Figure 3-8 is a graphical table representing the various bond conversions that can take place from glycerol to obtain the various observed products. The rate of 1,2-propanediol ($13 \text{ mol L}^{-1}\text{S}^{-1}\text{g}^{-1} 10^7$) and 2-propanol ($3 \text{ mol L}^{-1}\text{S}^{-1}\text{g}^{-1} 10^7$) can be summed together to obtain the cumulative rate for primary C–O cleavage of $16 \text{ mol L}^{-1}\text{S}^{-1}\text{g}^{-1} 10^7$. When comparing this to Davis et al. work with glycerol hydrogenolysis they observed 72% 1,2-propanediol and 28% ethylene glycol under similar conditions.¹⁶³

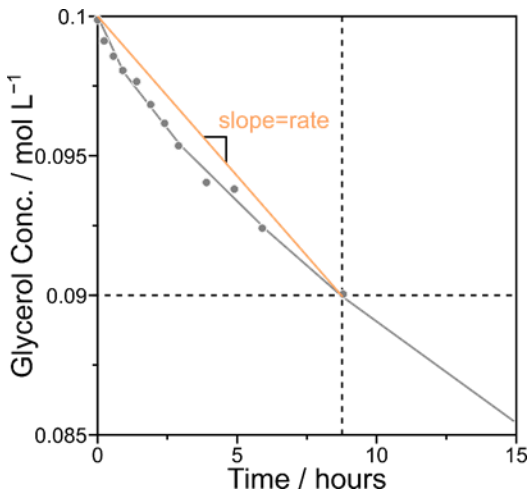


Figure 3-6. Concentration of glycerol as a function of time on a Pt catalyst. The horizontal dotted line is 10% conversion based on the reagent depletion, the vertical dotted line is the time for 10% conversion, the solid line are guidelines through the data points, and the yellow line is the slope/rate. For reagent depletion the negative slope is used for the rate.

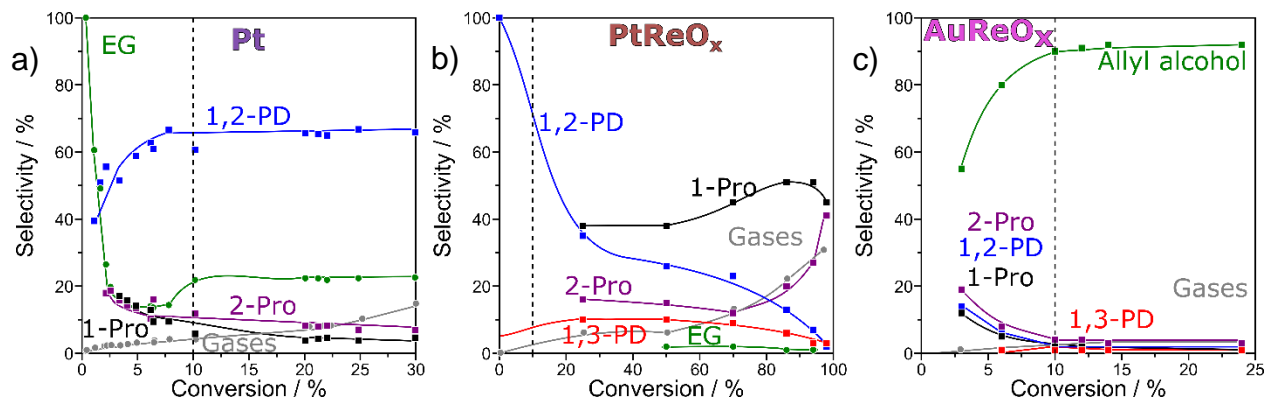


Figure 3-7. Selectivity as a function of conversion for a) Pt, b) PtReO_x, c) AuReO_x.

Table 3-2. Selectivities and initial rates at 10% conversion for glycerol (1 wt. %) hydrogenolysis on Pt/C with 2 replicates as well as glycerol (aq.) alone in the reactor and with the carbon Norit support.

Catalyst	Pt/C	Pt/C	Norit	None
Conv. (Feed)	10.00%	10.00%	0.00%	0.00%
T.O.S. (hr)	7.6	8.6	30.0	30.0
Cat. wt. (g)	0.3001	0.3000	0.3000	0.00
	Selectivities %	Initial Rates mols ⁻¹ s ⁻¹ g ⁻¹ 10 ⁷	Selectivities %	Initial Rates mols ⁻¹ s ⁻¹ g ⁻¹ 10 ⁷
Glycerol		24		23
1,2-PDO	71%	13	61%	13
EG	10%	4	18%	4
2-Pro	9%	3	11%	3
MeOH	5%	2	6%	2
Gases	5%	2	4%	1

Three PtReO_x samples were run using 1.0 and 0.1 g of catalyst which yielded different selectivities (Table 3-3). The selectivity as a function of conversion for PtReO_x (Figure 3-7 b) indicates that 1,2-propanediol is a primary product, and although the first sample didn't reveal 1,3-propanediol as a primary product it seems likely to be a primary product. 1- and 2-propanol appear around 20% conversion and remain approximately constant which indicates that they are secondary products. At 10% conversion no C–C cleavage is observed, and even at higher conversions, the amount of C–C cleavage is negligible. For the 0.1 g of catalyst sample, the ReO_x promoter increased rates by a factor of ~35 (normalized by Pt-surface atoms) and shifted selectivity from 1,2-propanediol (71%), ethylene glycol (10%), and 1-propanol (9%) to 1,3-propanediol (18%), 1,2-propanediol (20 %), 1-propanol (42%) and 2-propanol (19 %) at a conversion of 10% (Table 2-2). Pt facilitates primary C–O cleavage and minor C–C cleavage where the oxophilic metal promoter allows secondary C–O cleavage promotes primary C–O cleavage and almost eliminates C–C cleavage. Similarly, Davis et al. observed 1,2-

propanediol (36%), 1-propanol (25%), 1,3-propanediol (15%), ethanol (9%), 2-propanol (8%), EG (8%) at 50% conversion.¹⁶³

Table 3-3. Selectivities and initial rates at 10% conversion for glycerol (1 wt. %) hydrogenolysis on PtReO_x/C with 2 replicates.

Catalyst	PtReO _x /C	PtReO _x /C	PtReO _x /C			
Conv. (Feed)	10.00%	10.00%	10.00%			
T.O.S. (hr)	0.2	0.2	11.3			
Cat. wt. (g)	1.0000	1.0001	0.1001			
	Selectivities %	Initial Rates mols ⁻¹ s ⁻¹ g ⁻¹ 10 ⁷	Selectivities %	Initial Rates mols ⁻¹ s ⁻¹ g ⁻¹ 10 ⁷	Selectivities %	Initial Rates mols ⁻¹ s ⁻¹ g ⁻¹ 10 ⁷
Glycerol		553		840		818
1,2-PDO	71%	137	53%	271	20%	85
EG						
2-Pro	6%	71	11%	100	19%	84
1-Pro	15%	169	28%	250	42%	180
1,3-PD	5%	45	7%	66	18%	77
MeOH						
Gases	1%	1				

A carbon balance was obtained using the HPLC (the liquid phase products); the reactor was cooled, and a head space sample was injected into the GC-MS. Calibrations using manual gas phase injections are difficult, thus here we qualitatively identify the gas phase products—using a 50 mL Parr reactor after the 30-hour reaction. Carbon dioxide (2%) and methane (3%) were found in small quantities for Pt/C, and PtReO_x yielded carbon dioxide (<1%), and methane (<1%). At the catalyst loading and conditions used, glycerol does not readily react to gas phase species, but the PtReO_x/C generated less gas phase species because it created very little ethylene glycol if any.

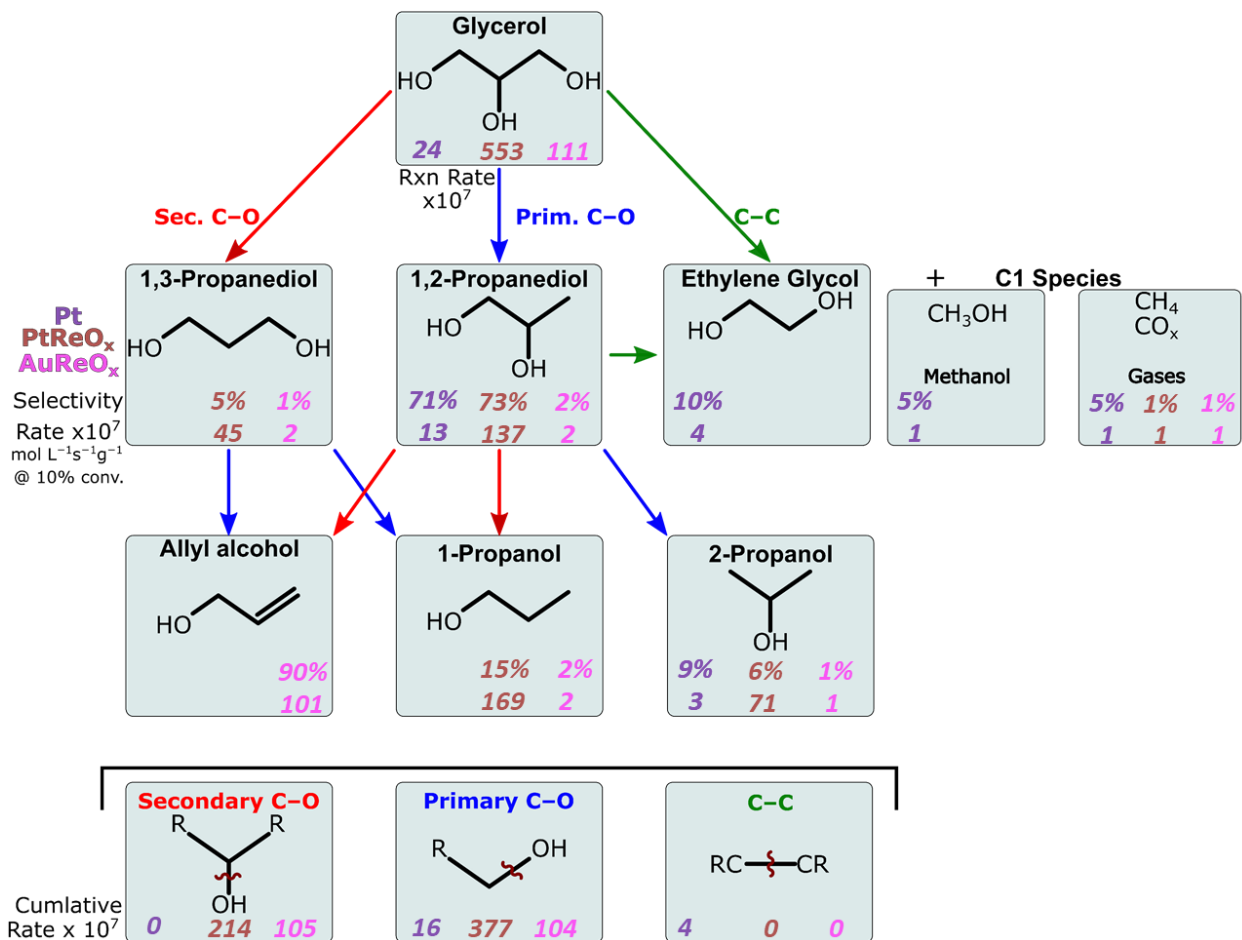


Figure 3-8. Reaction scheme for glycerol hydrogenolysis, comparing the rates and selectivities at 10% conversion for the 3 catalyst Pt, PtReO_x, and AuReO_x. (473 K, 4.0 MPa, 200 g glycerol (1 wt. %))

Several control reactions were performed to rule out factors that could conflate the results. First, a 1 wt. % glycerol (aq.) solution was loaded into the reactor absent of any catalyst or support to rule out thermo-based glycerol reactions, and over the 30 hours 0% conversion was observed with over a 99.8% carbon balance. The Norit SX-1G carbon and the CeO₂ support were reacted with 1 wt. % glycerol without any metal loading and both supports had 0% conversion and a >99.5% carbon balance (Table 3-2).

Effects of ReO_x promotion on poor hydrogenation catalysts (Au)

Au (1.0 wt. %) and Au (1.0 wt. %) Re (0.3 wt. %) were loaded on a ceria support via a base catalyst synthesis and incipient wetness. The monometallic Au impregnated catalyst had 1% conversion and a carbon balance of >98.0% after a 30-hour reaction. Figure 2-5 c) depicts the selectivity as a function of conversion for glycerol hydrogenolysis on AuReO_x; allyl alcohol is the dominant product but it is a secondary product because its selectivity increases and plateaus over conversion. The AuReO_x/CeO₂ catalyst reached 29% conversion over the 30 hours and created predominantly prop-2-en-ol (90%), 1-propanol (2%), 2-propanol (1%), 1,3-propanediol (1%), 1,3-propanediol (1%) at 10% conversion. The allyl alcohol that is produced is the result of both a primary and secondary C–O cleavage but remains unsaturated because the poor hydrogenation character of Au. The gas phase products formed were analyzed in reactions run in a 50 mL Parr reactor and produced <1% gases which was mainly methane. Similar results were observed by Tomishege et al, in which they observed allyl alcohol (91%) and 1-propanol (5%).¹⁷⁶

Ethanol Hydrogenolysis

Effects of ReO_x promotion on hydrogenolysis catalysts (Pt)

Unlike glycerol, ethanol reactions result in primarily gas phase products; the C–C cleavage often results in methanol, methane, or CO_x and the C–O cleavage forms ethane and water (Figure 2-7). Moreover, ethanol can undergo a C–O cleavage followed by a subsequent C–O coupling with another ethanol to form diethyl ether (DEE). For this reason, the 50 mL reactor connected to a GC-MS is used to quantitatively identify the products and their selectivities across the various catalysts. A

liquid sample was taken prior to and after the reaction and tested in an HPLC to examine the quantitative changes of concentrations in the liquid phase. A single reaction was performed in the 300 mL to examine the evolution of liquid phase products as a function of time during the 30-hour reaction.

Ethanol was reacted without any supports, with activated carbon, and with CeO₂ to see if ethanol undergoes thermal reactions or if support effects play a role in the reaction. With only ethanol (1 wt. %) in the reactor, approximately 1% conversion was observed forming only DEE with a >99% carbon balance and both carbon and ceria experience a 2% conversion forming only DEE.

Figure 3-9 shows the rates and selectivities at 10% conversion. The rate of reaction for ethanol on Pt is $132 \text{ mol L}^{-1}\text{s}^{-1}\text{g}^{-1}\times 10^7$, which is 5 times higher than that of glycerol indicating that ethanol hydrogenolysis is more facile. Ethane, methanol, and diethyl ether are made in equal parts (20%) with the predominant species being methane (35%). If ethanol undergoes C–C cleavage, methane and a CO_yH_x species would be made in equal molar proportions; if the rates of methanol and CO_x production are less than that of methane, additional C–O cleavages must have occurred. The lack of oxygenates may be from forming 2 methanes from ethane or cleaving methanol or CO_x making methane. With these considerations C–O coupling has a rate of 20, primary C–O cleavage has a rate of 62, and C–C cleavage is roughly two-thirds of that of C–O cleavage at $43 \text{ mol L}^{-1}\text{s}^{-1}\text{g}^{-1}\times 10^7$. The rate of C–C cleavage on Pt increases from 4 in glycerol to $43 \text{ L}^{-1}\text{s}^{-1}\text{g}^{-1}\times 10^7$, which may indicate the presence of alcohols in the α or β positions that affect how C–C cleavages occur. It is also interesting that the rate of methane production is twice that of ethane formation.

ReO_x promotion again increases the rate of reaction (Figure 3-9), this time from 132 to $811 \text{ L}^{-1}\text{s}^{-1}\text{g}^{-1} \times 10^7$. At 10% conversion almost only ethane and methane are observed (94%) indicating the rate of C–O cleavage ($560 \text{ L}^{-1}\text{s}^{-1}\text{g}^{-1} \times 10^7$) is more prevalent than C–C ($286 \text{ L}^{-1}\text{s}^{-1}\text{g}^{-1} \times 10^7$). Similar to Pt, the rate of C–C cleavage for ethanol is higher than that of glycerol hydrogenolysis for ReO_x -promoted Pt catalysts.

Effects of ReO_x promotion on poor hydrogenation catalysts (Au)

$\text{AuReO}_x/\text{CeO}_2$ in ethanol (aq.) forms primarily gas phase products (Figure 2-7), methanol and DEE were the only liquid phase molecule found using the HPLC and had a conversion of 36% (based on feed depletion) after 30 hours. The GC hooked up inline to the 50 mL Parr reactor reveled selectivities for ethylene (61%), ethane (18%), methane (11%), methanol (10%), CO_x (0%), and DEE (0%). Like glycerol on AuReO_x , an unsaturated compound formed from a C–O cleavage; ethylene is formed from the primary C–O cleavage and a hydrogen leaving, forming the double C–C bond. An elimination of the C–O coupling mechanism as well as no CO_x species are observed. Because there are equal parts methanol and methane, it can be inferred that C–C cleavages only occur from ethanol, and methanol does not undergo C–O cleavage after it is formed.

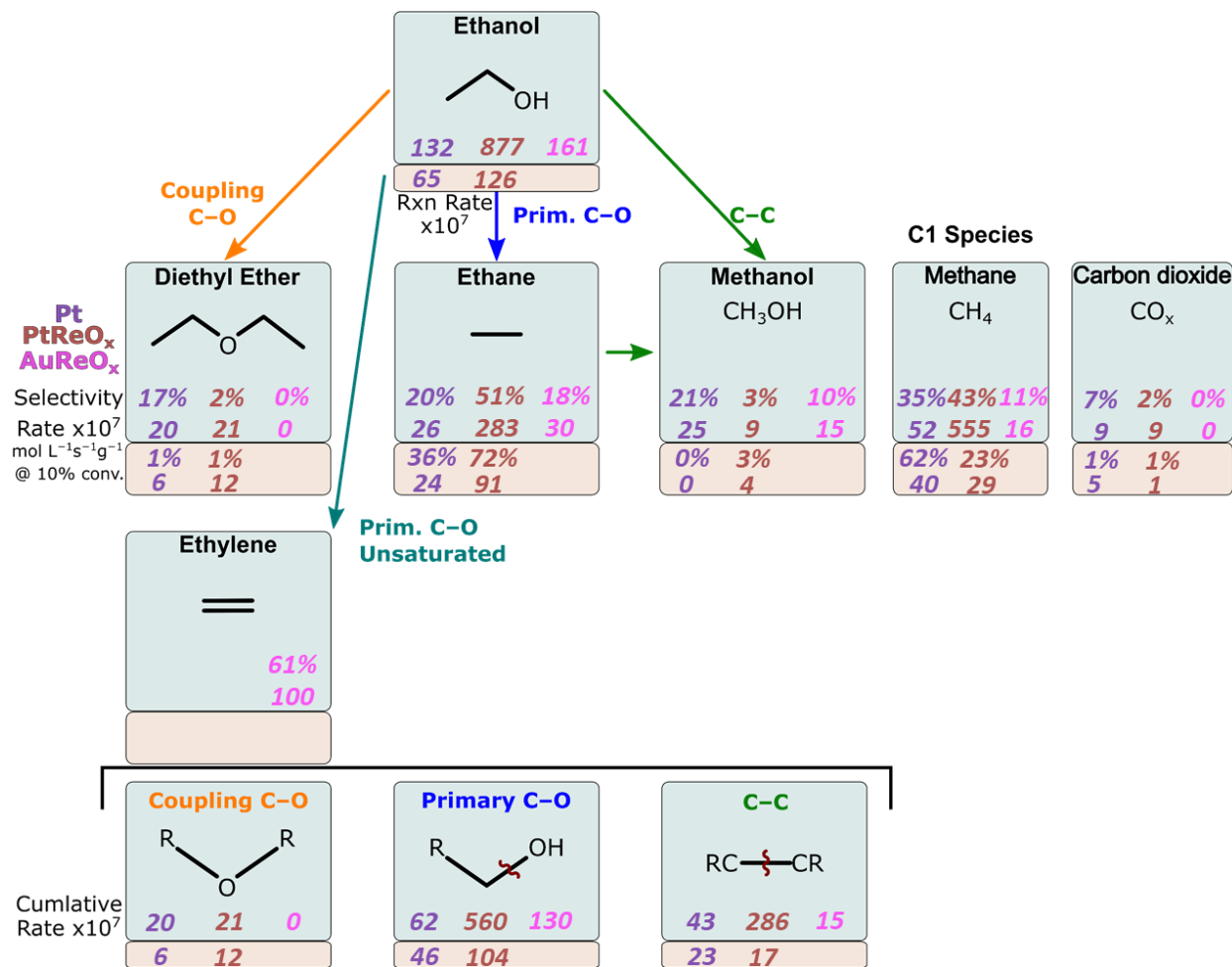


Figure 3-9. Reaction scheme for ethanol, comparing the rates and selectivities at 10% conversion for the three catalysts: Pt, PtReO_x, and AuReO_x, in the liquid phase (blue boxes) and the gas phase (tan boxes). (473 K, 4.0 MPa, 200 g glycerol (1 wt. %))

Continuous flow reactor, ethanol (g) reagent

Using the flow reactor described in the Methods section, ethanol is vaporized in a hydrogen gas stream and was reacted over plug flow reactor using either Pt/C or PtReO_x/C. A GC is used and it revealed that four products are produced by this reaction: ethane, methane, methanol, and diethyl ether (DEE). Using a temperature of approximately 488 K, the total flow rates are varied from 50–400 SCCM, and the molar reagent concentration (ethanol:H₂) were varied from 0.01–0.05. However, the increased

flowrate increases the pressure drop in the GC sampling loop (Appendix B-2), which subsequently allows more products in the same loop causing deviations in peak areas. An internal standard of Ar (5 mol %) balance in H₂ is being used to help correct this as well as help correct for other deviations in the flow unit (Future Works).

Because the peak areas are related to both the conversion and the flowrate, for the remainder of the study, the condition of interest has a measured flowrate of 107 SCCM while the molar ratio is kept constant at a molar ratio of (ethanol:H₂) 0.037. For the Pt catalyst (Figure 3-9), the rate of reaction is 65 L⁻¹s⁻¹g⁻¹ × 10⁷ with ethane (36%) and methane (62%) being the dominant species with no methanol or CO_x present. This reflects that oxygenated species are not favored in gas phase reaction in the presence of no feed water, and C–O cleavage is the prevailing reaction. ReO_x has a promotional effect again but this time it only increases rates by a factor of 2 compared to the Pt catalyst. Most of the products formed are ethane, meaning primary C–O cleavage is almost 10 x more likely than C–C cleavages. However, more CO_yH_x species are seen with the ReO_x than Pt indicating that the ReO_x facilitates some role in the C–O cleavages. C–O coupling is increased by a factor of 2 from the monometallic to bimetallic catalyst which is increased as primary C–O cleavage is enhanced.

Water phase effects on alcohol conversion

The phase effects of water on the alcohol conversion were explored by running ethanol in two batch phase reactors as well as a continuous phase flow reactor. The rate of reaction of Pt in the vapor is half of that of the liquid phase, and the PtReO_x is 6 times smaller than that of the liquid phase reactions. The liquid phase reactions produced oxygenated compounds such as methanol or CO_x, at a much higher rate than in the vapor phase. Water must play some role in either coordinating species to adsorb

to the metal sites or stabilizing intermediate and participating in proton shuttling to enhance rates. Since C–OH cleavage will form water, the driving force in the aqueous media is lower than that of the gas phase since pure ethanol is feed into the reactor. The only water present is that which forms during the reaction reflecting water's role in C–O cleavage. The reduction of diethyl ether formation in the gas phase is observed; rates of $20 \text{ L}^{-1}\text{s}^{-1}\text{g}^{-1}\times 10^7$ for liquid phase compared to 6 and $12 \text{ L}^{-1}\text{s}^{-1}\text{g}^{-1}\times 10^7$ in the gas phase, for Pt and PtReO_x, respectively, is likely because water H-bonding helps bring 2 ethanols into close enough contact to react.

Conclusion

ReO_x promotion on Pt based catalysts for glycerol shifted selectivities from 1,2-propanediol (72%), ethylene glycol (19%), and 1-propanol (9%) to 1,3-propanediol (18%), 1,2-propanediol (20 %), 1-propanol (42%) and 2-propanol (19 %) at a conversion of 10% (Table 2-2) with rates ~10 time higher than the monometallic. This indicates oxophilic metal promoters increase secondary C–O cleavage and almost completely suppress C–C cleavage. This promotional enhancement is seen on non-hydrogenolysis metals like Au which in its monometallic form is non-reactive. AuReO_x/CeO₂ formed prop-2-en-ol (90%), 1-propanol (4%), 2-propanol (3%), 1,3-propanediol (2%), methanol (1%), and a carbon balance of 95% from glycerol. The allyl alcohol that is produced is the result of first a primary and then a secondary C–O cleavage. The fact that no propane is observed indicates the role that an α– or β–diol plays on small polyol species.

An even smaller alcohol, ethanol does produce alkane species unlike glycerol or the other C₃ alcohols. Ethanol (aq.) exhibited similar trends to glycerol in that the rates for Pt, PtReO_x, and AuReO_x were 132 , 877 , and $161 \text{ L}^{-1}\text{s}^{-1}\text{g}^{-1}\times 10^7$, respectively —

ReO_x enhanced the rates reactions and ethanol hydrogenolysis occurs more quickly than glycerol. The Pt catalyst produced methane (35%) and equal parts ethane, methanol and diethyl ether (20%). Primary C–O cleavage (rate of $62 \text{ L}^{-1}\text{s}^{-1}\text{g}^{-1}\times 10^7$) is the dominant reaction occurring but much more C–C cleavage ($43 \text{ L}^{-1}\text{s}^{-1}\text{g}^{-1}\times 10^7$) is observed compared to glycerol ($4 \text{ L}^{-1}\text{s}^{-1}\text{g}^{-1}\times 10^7$). PtReO_x were dominated by the non-oxygenated species ethane (51%) and methane (43%) with their rates being ~10 times higher than that of the Pt catalyst. Lastly, AuReO_x catalysts produced an unsaturated species, ethylene (61%) as well as ethane (18%) and equal parts methanol and methane (10%). This represents a 3-fold decrease in C–C cleavage compared to Pt and 19 times smaller than that of PtReO_x.

Ethanol in the vapor phase exhibited rates of reactions of 65 and $126 \text{ L}^{-1}\text{s}^{-1}\text{g}^{-1}\times 10^7$ for Pt and PtReO_x, respectively. ReO_x still enhances the rates of reactions but the rate is higher for liquid phase reactions indicating water plays a role in the mechanisms. There are virtually no oxygenated species when the reaction is performed in vapor phase, only ethane (36% Pt, 72% PtReO_x) and methane (36% Pt, 72% PtReO_x) which further predicts that water stabilizes oxygenated intermediates. The rate of C–C cleavage is roughly the same for Pt and PtReO_x ($\sim 20 \text{ L}^{-1}\text{s}^{-1}\text{g}^{-1}\times 10^7$) however the primary C–O cleavage is more than double (46 Pt, 104 PtReO_x, $\text{L}^{-1}\text{s}^{-1}\text{g}^{-1}\times 10^7$) for the oxyphilic metal promotion.

Future Works

The flow reactor for gas phase ethanol reactions will be used to gather additional information on the role of water and Brønsted acids for alcohol hydrogenolysis. Elucidating these mechanisms will be done by performing the reactions at a variety of flow rates and reagent to H₂ ratios, as well as using feed streams of pure ethanol (what

this study used) and mixtures of ethanol in water. Furthermore, an advantage of a flow reactor is the ability to titrate the catalyst, being able to count acid sites (ReO_x) which will give more credence to the role Bronsted acid site on oxyphilic metal promotion. Although the supports themselves did not cause reactions, the metal-support interactions could cause changes in selectivities. Synthesizing either Pt or PtReO_x on CeO_2 or synthesizing AuReO_x on C would reveal the role of these interactions. Lastly, ethylene glycol will be used to further understand the intermediates because there remains uncertainty in what are the primary and secondary products.

CHAPTER 4

NO_x REDUCTION USING ATOMICALLY DISPERSED RHODIUM ON OXIDE SURFACES FOR POTENTIAL AUTOMOTIVE CATALYSTIC CONVERTER APPLICATIONS

Introduction

The improved air quality in many urban areas across the globe can be attributed to automotive catalytic converters. The three-way catalysts (TWC), designed for gasoline engines, consists of Pt, Pd and Rh which simultaneously reduces and oxidizes pollutants to reduce emissions. The oxidation of CO and unburnt hydrocarbons are typically performed by Pt and Pd where NO reduction to N₂ occurs predominately on the Rh site.^{183–186} The mechanism for the reduction on Rh remains elusive, however increased demands for higher emission control are prompting more research into this phenomenon.^{183,185} Furthermore, elucidating this mechanism could make TWCs more economical by increasing the metal-utilization efficiency since precious metals are expensive. Discovering insights to NO reduction could direct Rh structures that would enable novel TWC designs with improved performance. Crucial insights into the mechanisms that atomic Rh plays on NO reduction is highly advantageous; yet a rigorous comparison changing environmental and support conditions have not been studied.

The TWC is unique in its ability to oxidation and reduction under a dynamic and wide range of inlet compositions and temperatures.^{183–186} Often the TWC supports consist of Al₂O₃, CeO₂ and ZrO₂ which have Pt, Pd, or Rh particles deposited on the surface. Because the mechanisms are not well understood, the current state of TWCs have been optimized in a combinatorial experimental way. But emission standards, like the US EPA Tier 3¹⁸⁷ and California Air Resources Board LEV III standards,¹⁸⁷ are

increasing the demand to understand the way in which these reactions occur.

Atomically dispersed Rh is less studied than Rh particles which restricts the advancements in TWC metal utilization efficiencies and overall performance.

Rh has a low volatility compared to Ru and Ir, which allows the Rh to stay on the support where it demonstrates high rates and selectivity at reducing NO_x to N₂ compared to Pt or Pd.¹⁸⁸ But again the exact Rh site and mechanisms are not well understood under the wide range of reaction conditions.^{185,186,189,190} Single crystal Rh surface studies indicate NO dissociation is more facile than Pd or Pt and that undercoordinated defect sites are where most of the reactions take place.^{191–196} However, extended surfaces are not common in TWC at the low Rh loading (< 0.3 wt. %) and these studies do not explain the observed promotion that Rh on supports exhibit for NO reduction.¹⁸⁵ Examining the Rh–support interactions indicates atomic Rh may be the active site in the TWC which is further proven by the fact Rh can coordinate 2 ligands (e.g., CO, NO and/or olefins); creating new reaction pathways for NO reduction.¹⁹⁷

Dynamic changes in the reactivity and selectivity for NO reduction occur and shift as a function of operating condition. These shifts could be attributed to changes in the local structure or environment which shift the reaction mechanism. Higher Rh loading studies have reacted mixtures of NO+H₂ and NO+CO under reaction conditions.^{198–202} These higher loadings form particles while the creation of atomically dispersed Rh on single oxide particles (Al₂O₃, CeO₂ and TiO₂) facilitating lignin chemistry on the metal^{32,36} which under reaction conditions it is shown isolated Rh sites are active.^{203–206} NO reduction is often comprised of complex reaction networks but the N–O cleavage

step is often the rate-determining step.^{207–218} Studies over a wide range of NO coverages on Pt(111) show HNOH* is first formed which cleave the N–O bond.^{125,219} However, water, over a wide range of H₂O:NO ratios, does not affect the rates indicating water does not play a direct role in N–O cleavage.²¹⁹ A reaction mechanism over isolated Rh has been proposed to undergo direct NO* dissociation followed by Rh–N coupling to NO forming N₂ or N₂O.²²⁰

Here we set out to observe the effects of atomic Rh structures on various oxides (Al₂O₃, CeO₂ and TiO₂). First, surface formation energies will be used to determine the most stable facets of the proposed oxides. The binding energies and stable configurations will be found for the following states: Rh, Rh–CO, CO–Rh–CO, Rh–NO, NO–Rh–NO, and CO–Rh–NO, on the most stable oxide surfaces. The binding energies and exchange energies for CO and NO are calculated to start to examine reaction barriers and kinetics for NO reduction in automotive conditions.

Methods

Four oxide materials were considered in this work, TiO₂ anatase and rutile, CeO₂, and γ-Al₂O₃; the bulk structures were obtained from the Crystallographic Open Database. Periodic, plane-wave based DFT calculations were implemented using the Vienna ab initio simulation package (VASP). Wavefunctions were constructed using PAW potentials and energies will be converged to within 10⁻⁶ eV; exchange-correlation energies were computed using the revised Perdew-Berke-Ernzerhof (RPBE) functional.⁸⁰ Atomic positions were relaxed until the maximum force on all atoms is < 0.05 eV Å⁻¹.^{67,81} During these calculations, a Γ-centered 1 × 1 × 1 K-point mesh was used to sample the first Brillouin zone. Isolated Rh atoms were modeled on support oxides. Rh/CeO₂, for example, was modeled as a Rh-adatom on a 3 × 3 CeO₂ (111)

surface with 4 layers perpendicular to the surface. These calculations were modeled spin polarized with the addition of the Hubbard U-term to correct for improper delocalization of electrons in Ce's f-orbitals (DFT+U).⁸² The value of the U parameter can have influences on the energy; the formation energy of Ce and O₂ to form CeO₂ changed by 100 kJ mol⁻¹ when the U parameter was changed from 0–9.²²¹ A variety of U parameters were tested for this study and a U of 2 yielded the closest unit cell size to experiments.

Transition state structures were isolated using a combination of NEB⁸³⁻⁸⁴ and dimer methods. Frequency calculations were performed for relevant minima and transition state structures to calculate zero-point energies and entropies of adsorbed species to ultimately calculate reaction and activation enthalpies and free energies. More details for the NEB, Dimer, and frequencies are provided in Chapter 2: Methods. All calculations were setup, monitored, and verified using the computational catalysis interface (CCI), which automates and simplifies DFT studies.

Surface formation energies were calculated for over a dozen facets that were cleaved from the converged bulk structures using the following parameters.

$$\text{Surface formation energy} = \frac{E_s - N_s \times \frac{E_b}{N_b}}{2A} \quad (4-1)$$

Where E_s is the energy of the surface, N_s is the number of atoms on the surface, E_b is the energy of the bulk structure, N_b is the number of atoms in the bulk, and A is the surface area of the facet. The facet with the lowest surface formation energy for each oxide had a Rh-adsorbate structure added to the surface, and had subsequent adsorbates placed on or around the Rh atom.

Redhead Analysis was used to convert the experimentally derived temperature programmed desorption (TPD) spectra to binding energies. Equation 4-2 depicts the conversion from the inputs and outputs of the TPD to binding energies.

$$\frac{E}{RT_p} = \ln\left(\frac{vT_p}{\beta}\right) - 3.64 \quad (4-2)$$

Where E is the energy of desorption in kJ mol⁻¹, T_p is the temperature at peak desorption rate, R is the ideal gas constant, v is the pre-factor in literature for 1st order CO–Rh binding, B is the temperature ramp rate, and 3.64 is an empirical number made from the conditions described.

This study examines atomically dispersed Rh on oxide surfaces — both polymorphs of TiO₂, anatase and rutile, as well as γ-Al₂O₃ and CeO₂. The bulk structures will be optimized using DFT and surface formation energies were found for multiple facets and terminations for the oxides listed above. CO*, 2 CO*, NO*, 2 NO*, and CO*+NO* were placed in multiple configurations on Rh bound to the oxide surface giving binding and exchange energies.

Results & Discussion

Surface Formation Energies

The bulk structures for TiO₂ (anatase, rutile, and P25), CeO₂, and γ-Al₂O₃ were optimized for find the surface formation energies of the various facets. TiO₂ the polymorph P25 is an experimentally derived structure for an industrially produced surface that is roughly 25% rutile and 75% anatase. Collaborators at USCB preferred focusing on the 2 main polymorphs (anatase and rutile) for now with an emphasis on rutile. All structures are available in Appendix C (Figure C-2–5), and a summary table of energies can be found in Table 4-1. For rutile the most stable surface is the (110), which

was corroborated with previous literature to be the most common thermodynamically stable surface whose surface formation energy was found to be $5.7 \text{ kJ mol}^{-1} \text{ A}^{-1}$. For anatase the (100), (001), (110), (101), and the (111) terraces were considered, and each terrace had 1–3 unique terminations. The most stable surface formation energy for each of the surfaces were 5.9, 5.8, 9.5, 9.0, and $28.0 \text{ kJ mol}^{-1} \text{ A}^{-1}$ for the (100), (001), (110), (101), and the (111) terraces, respectively. The rutile (110) and anatase (100) were found to be the most stable facets in prior work.^{222,223} It is suggested that defect sites or stepped surface play a major role in NO reduction²²⁴; the (021) and (145) planes were also examined with energies of 9.0 and $8.5 \text{ kJ mol}^{-1} \text{ A}^{-1}$, respectively. The CeO_2 surfaces (110) and (111) were examined which yielded formation energies of 6.3 and $2.9 \text{ kJ mol}^{-1} \text{ A}^{-1}$, respectively. Which is consistent with literature results which revealed the surface stability for the facets are (111)>(110)>(100).²²⁵ Lastly, $\gamma\text{-Al}_2\text{O}_3$ examined the following facets (100), (001), (010), and (111) which had formation energies of 12.5, 17.1, 11.7, and $20.3 \text{ kJ mol}^{-1} \text{ A}^{-1}$, respectively which is validated by further literature.²²⁶

Table 4-1. Surface formation energies (in $\text{kJ mol}^{-1} \text{ A}^{-1}$) for the following facets and terminations for the four oxides that converged.

Facet/Term.	Al_2O_3 Gamma				TiO_2 Anatase					TiO_2 Rutile	CeO_2	
	100	001	010	111	100	001	110	101	111	110	110	111
A	16.8	22.2	19.5	20.3	6.0	18.9	9.5	9.0	28.0	5.7	6.5	2.9
B	14.9	17.2	18.1				5.8					
C	12.5		11.7									

CO and NO Adsorption Energies

The $\gamma\text{-Al}_2\text{O}_3$ (010) surface is of the most interest for the experimental collaborators and was extensively studied using DFT. A Rh atom was systematically placed on several locations on the $\gamma\text{-Al}_2\text{O}_3$. Upon optimizing, there was only 1 stable

placement of an atomic Rh (Figure 4-1 a) which was in a 3-fold site. A single CO is able to bind in 3 unique ways to the Rh (Figure 4-1 b) with CO adsorption free energies of -240 , -237 , and -214 kJ mol^{-1} (1 bar and 573 K). The two most stable configurations are the Rh in a 3-fold site, however the presence of an adsorbate on Rh can sit on a bridge site. Initially, 24 structural configurations were optimized resulting in the 3 unique configurations shown in Figure 4-1 b. The energy spread for the 1st CO binding energy is shown in Figure 4-2 a) and it should be noted that the relative energy difference for E0, H, and G are approximately the same ($<2 \text{ kJ mol}^{-1}$) for all structures.

Atomic Rh can facilitate the binding of 2 species so 2nd CO BEs were explored. six unique structures were obtained from 12 initial structural configurations (Figure 4-1 c) with binding free energies ranging from -88 – 13 kJ mol^{-1} (Figure 4-2 b). The most stable di-carbonyl structure has a bent CO* which is mildly interacting with oxide. The mobility of Rh on an oxide surface is still being explored however the energies of these various configurations and Rh placements implies that Rh is mobile under these conditions.

Mono- and Di- NO adsorption can take place on the Rh atom at conditions relevant to automotive exhaust. NO prefers to bind atop on Rh which sits in a 3-fold site (most stable) or 9 kJ mol^{-1} less stable sitting on a bridge site (Figure 4-3 a). When a second NO is allowed to adsorb, it does so with a free binding energy of -327 kJ mol^{-1} at 573 K. Out of 12 initial structural structures, 6 unique converged configurations exist for the di-nitrosyls (Figure 4-3 b). One nitrogen strongly interacts with the oxide in the most stable structures causing it to bend and interact with the Rh and the oxide surface.

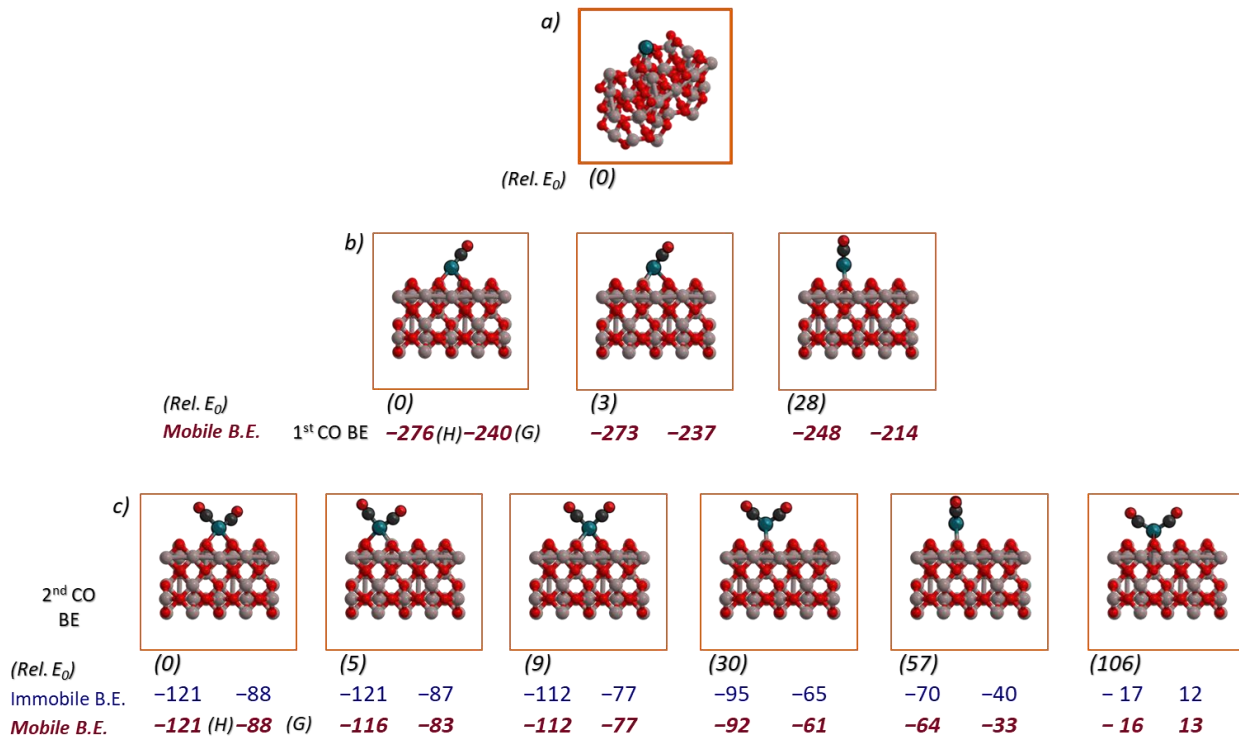


Figure 4-1. The structures and energies (E_0 , and G) in kJ mol^{-1} for mono- (b) and di-carbonyls (c) binding to a Rh atom (a) on the Al_2O_3 (010) surface at 573 K and 1 bar.

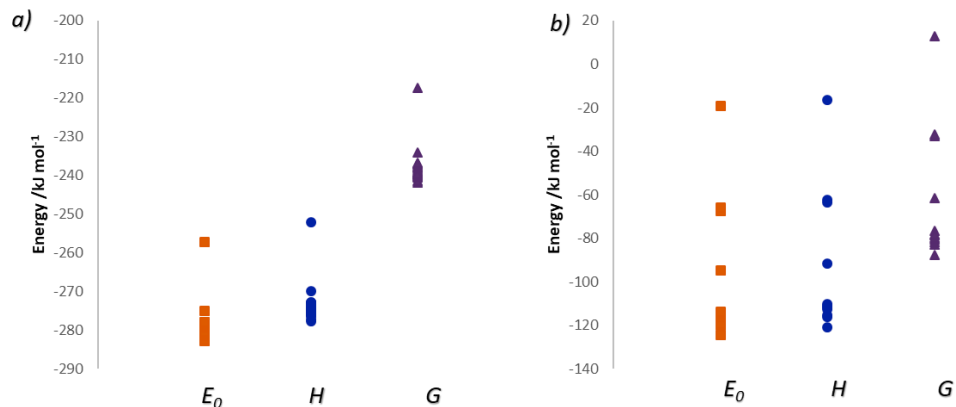


Figure 4-2. The spread of electronic (E_0) and free energies (G) as well as enthalpy (H) for the a) 24 configurations for the first CO binding energy and b) the 12 configurations for the second CO binding energy.

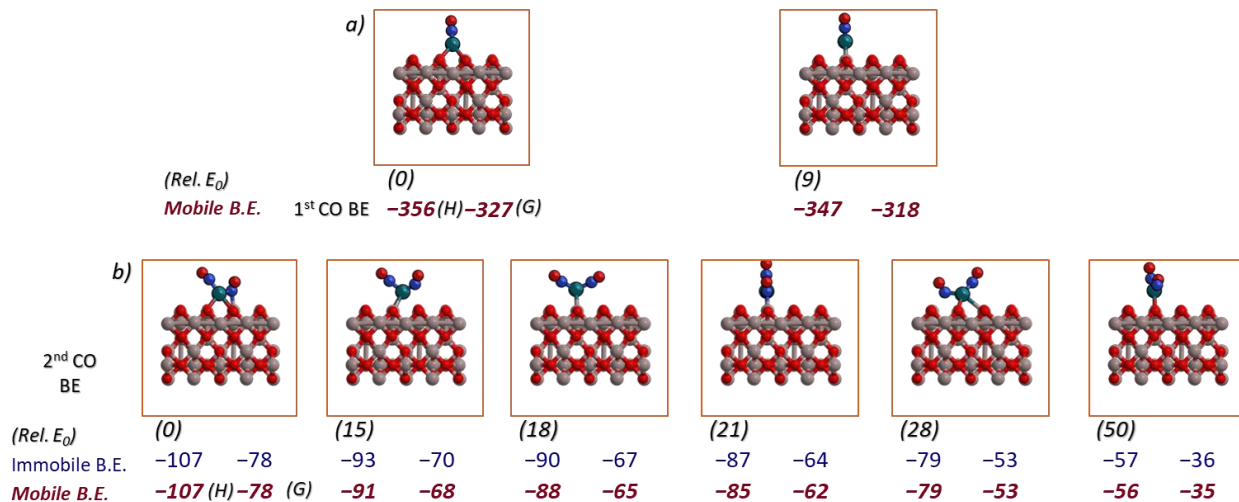
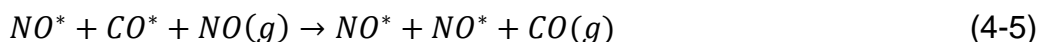
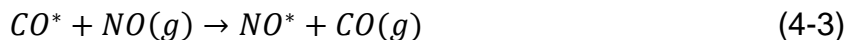


Figure 4-3. The unique NO binding configurations with their relative E_0 , Gibbs free energy calculated in kJ mol⁻¹ at 573 K and 1 bar.

CO and NO Exchange Energies

Using the various state calculations in the previous section, the exchange energies can be calculated. These represent the amount of energy required to replace an existing adsorbate with a different one and are defined in the following equations.



CO binds more weakly than NO creating a CO to NO free exchange energy of -93 kJ mol⁻¹; if a single CO on a di-carbonyl is replaced with an NO the exchange energy is -83 kJ mol⁻¹. However, it is almost energy neutral for a CO and NO bound on a Rh atom to form a dinitrosyl (-5 kJ mol⁻¹). On the CO-Rh-NO state, the NO is bound strongly to the oxide, and the CO which is replaced by a 2nd NO does not get the additional stabilization from the oxide. A figure depicting the most stable configuration

for each state with their energies has arrows indicating the exchange energy (Figure 4-4) taking place. These exchange energies are found in Table 4-2.

Table 4-2. The binding energies/exchange energies/enthalpies (kJ mol^{-1}) for CO and NO adsorbed on a Rh surface at 573 K and 1 bar.

		E_0	H	G
Binding Energies	1st CO	-281	-276	-240
	2nd CO	-125	-121	-88
	1st NO	-362	-356	-327
	2nd NO	-109	-107	-78
Exchange Energies	$\text{CO}^* + \text{NO}(g) \rightarrow \text{NO}^* + \text{CO}(g)$	-91	-92	-93
	$\text{CO}^* + \text{CO}^* + \text{NO}(g) \rightarrow \text{CO}^* + \text{NO}^* + \text{CO}(g)$	-86	-87	-83
	$\text{NO}^* + \text{CO}^* + \text{NO}(g) \rightarrow \text{NO}^* + \text{NO}^* + \text{CO}(g)$	1	-3	-5

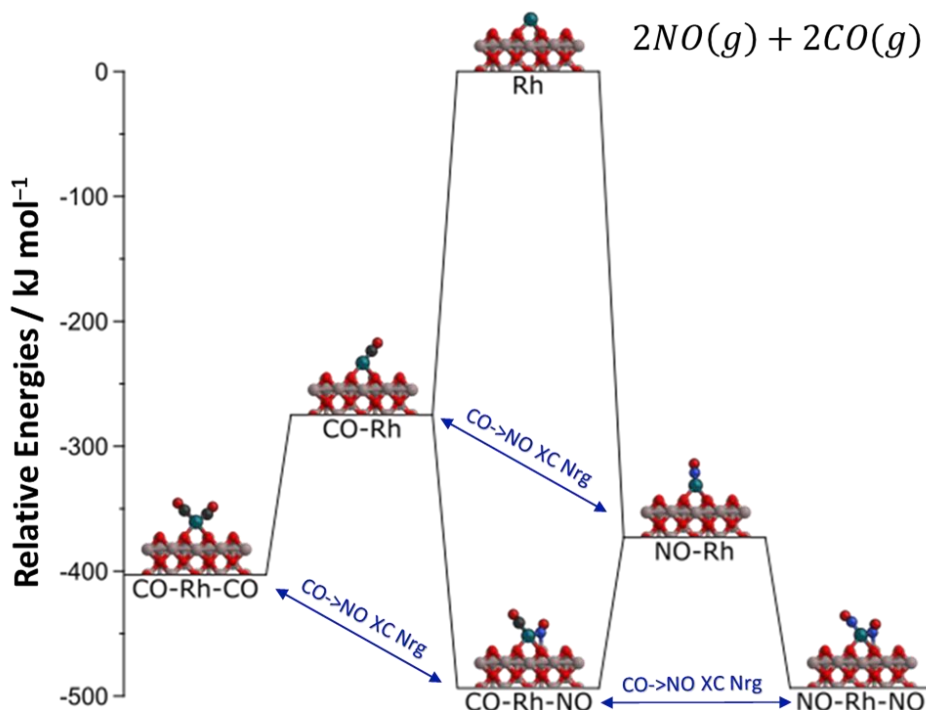


Figure 4-4. The binding energies and the exchange correlation energies for CO and NO with the structure of the most stable state presented.

Frequencies

Zero-point vibration energies and frequencies were found using DFT on the structures list above. A single CO* on a Rh particle has a C-O stretch of 1937 cm⁻¹, when a second CO* is present a symmetric vibration occurs at 1964 cm⁻¹ (27 cm⁻¹ higher than the isolated CO*) and an asymmetric vibration occurs 28 cm⁻¹ lower at 1909 cm⁻¹. The DFT predicted gas phase vibrations for CO and NO are 2102 and 1898 cm⁻¹, respectively. DFT predicts lower frequencies than experimental results, however published experimental CO* and NO* on atomic Rh have yet to be published for direct comparisons. The NO* binds with a vibration at 1799 cm⁻¹; and similarly, there is a up and down shift of about 50 cm⁻¹ for the symmetric and asymmetric di-NO* stretches, respectively. The Rh-NO-CO state has the C–O vibration occur at 1956 cm⁻¹ (about the same as the symmetric (sym.) Rh-CO-CO) and a N–O vibration at 1671 cm⁻¹ (close to the asymmetric (asym.) vibration of Rh-NO-NO).

Table 4-3. The vibrational frequencies for the various vibration on Al₂O₃ (010) (X=C or N): X-O (asymmetric (asym.) and symmetric (sym.)), X-X (wag), Rh-X (Wag both asym. and sym.), O-X-Rh (wag) of the described states.

Frequencies (cm ⁻¹)	X-O sym.	X-O Asym.	X-X wag	Rh-X Sym.	Rh-X Asym.	O-X-Rh wag(sym.)	O-X-Rh wag(asym.)	O-X-Rh wag
CO (gas)			2102					
NO (gas)			1898					
Rh-CO		1937			540	488	462	
Rh-CO-CO	1964	1909	545	497	454	422	337	285
Rh-NO		1799			620	488	422	
Rh-NO-NO	1754	1661	600	523	470	353	259	170
Rh-NO-CO	1956	1671	670	526	475	434	349	254

Conclusion

Surface formation energies were calculated for a number of oxides, polymorphs, facets, and terminations. γ -Al₂O₃ has the most stable surface formation energy (11.7 kJ mol⁻¹ Å⁻¹) however high defect/step edge surfaces (021) and (145) had relatively low formation energies of 19.0 and 18.5 kJ mol⁻¹ Å⁻¹. Rhodium has only one stable location on the γ -Al₂O₃ surface which is 3-fold bound to 2 oxygens and 1 Al. NO binds atop to Rh (-327 kJ mol⁻¹) with a N–O vibration at 1799 cm⁻¹ and is stronger than C–O (-240 kJ mol⁻¹) with a frequency of 1937 cm⁻¹. The second binding energy for NO and CO are -78 and -88 kJ mol⁻¹ with symmetric and asymmetric bond stretches of 1964 and 1909 and 1754 and 1661 cm⁻¹, respectively. One NO is strongly interacting with the oxide surface when there are 2 species bound to the Rh, this results in negligible CO to NO exchange energies (-5 kJ mol⁻¹).

Future Works

Reactions

The single Rh atom allows bound species to uniquely interact with oxide simultaneously opening new mechanistic routes for CO reduction or NO_x oxidation that are not feasible with a Rh particle or surface. Two similar reactions will be first explored using the same initial state CO-Rh-NO to i) C*-Rh NO₂ (g) and ii) N*-Rh CO₂ (g). The reaction energy and barriers could be lower for the 2 reactions than a Rh particle or surface.

Hydroxyl Groups

Under reaction automotive exhaust conditions our collaborators at Ford Motors have witnessed hydroxyl groups form on the oxide surface. All unique oxygens had a

hydrogen placed upon it and the state calculations (Rh-CO, CO-Rh-CO, Rh-NO, NO-Rh-NO, CO-Rh-NO) as well as the reactions were re-setup in this new environment.

Defect and Step Edge Sites

There is evidence that defect and step edges play a dominant role in NO_x reduction and CO oxidation, thus oxygen and metal vacancies were created and step edge facets (021) and (145). The surface formation energies for most stable oxygen and metal vacancies are 22.2 and 25.1 kJ mol⁻¹ Å⁻¹ and the two facets are 19.0 and 18.5 kJ mol⁻¹ Å⁻¹, respectively. The vacancies or step edge terraces could bind Rh stronger than without the vacancies or defects could prevail different chemistries.

APPENDIX A
SUPPORTING INFORMATION FOR CHAPTER 2

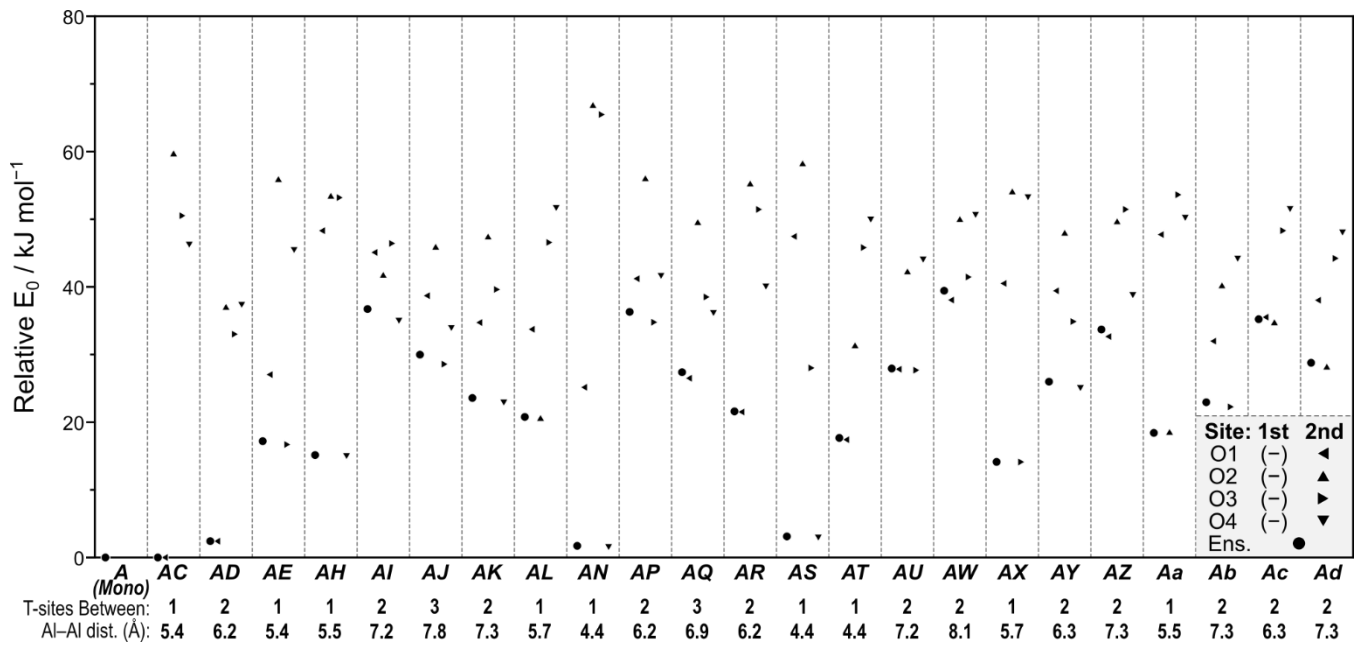


Figure A-1. The relative E_0 for the isolated acid site (for which there is only one structure) and all site-pairs where the second site is protonated, with the number of Si linkers between each site and the distance in Å between the T-atoms of each site shown below. Circles represent ensemble average E_0 for each site-pair, and triangles mark individual E_0 . The direction of the triangle indicates the location of the H on the second site: O1 (◀), O2 (▲), O3 (►), and O4 (▼).

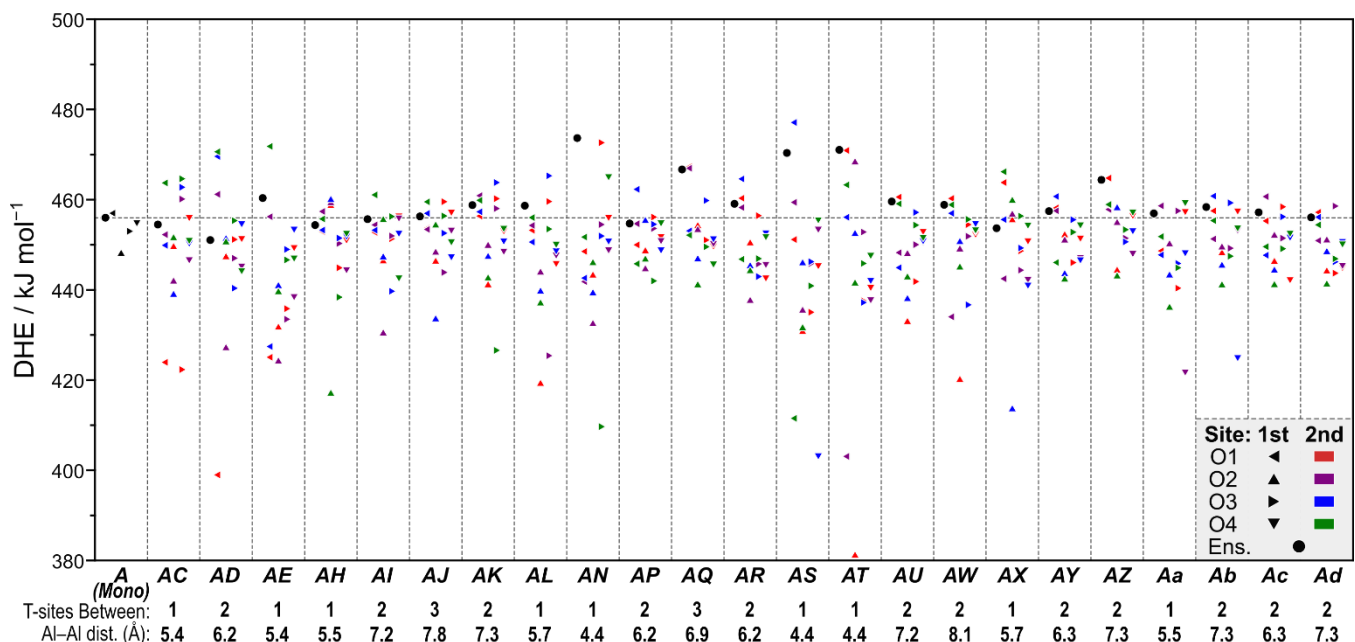


Figure A-2. The DHE for the isolated acid site and all site-pairs where the second site is protonated, with the number of Si linkers between each site and the distance in Å

between the T-atoms of each site shown below. Circles represent ensemble average DHE for each site-pair. The dashed line marks the ensemble average DHE of the isolated site and triangles mark individual DHE for each configuration. The direction of each triangle indicates the O atom from which the H was removed: O1 (\blacktriangleleft), O2 (\blacktriangleup), O3 (\blacktriangleright), and O4 (\blacktriangledown). The color of each triangle denotes the location of the remaining H on the second site: O1 (red), O2 (purple), O3 (blue), and O4 (green). The configuration of the most acidic protons for each site combination by DHE is marked near its representative point, and the dehydrogenated O atom on the A site is underlined.

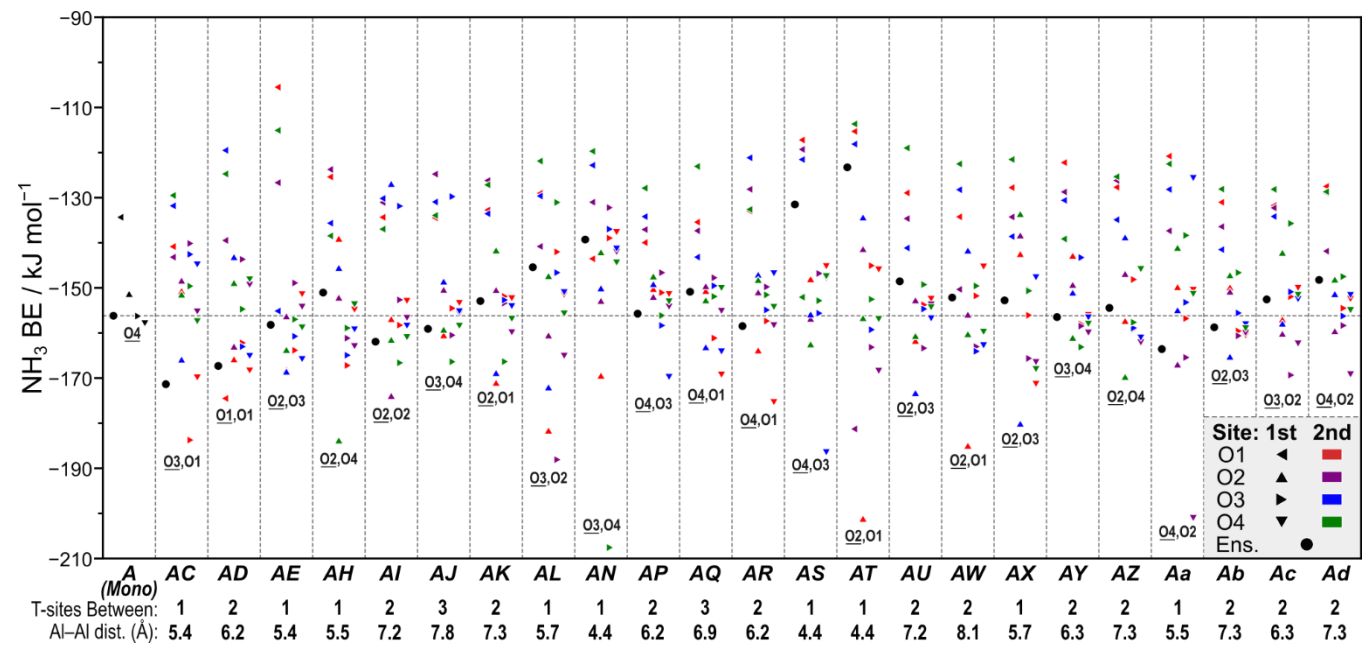


Figure A-3. The NH_3 BE for the isolated acid site and all site-pairs where the second site is protonated, with the number of Si linkers between each site and the distance in Å between the T-atoms of each site shown below. Circles represent ensemble average NH_3 BE for each site-pair. The dashed line marks the ensemble average NH_3 BE of the isolated site and triangles mark individual NH_3 BE for each configuration. The direction of each triangle indicates the O atom from which the H was removed: O1 (\blacktriangleleft), O2 (\blacktriangleup), O3 (\blacktriangleright), and O4 (\blacktriangledown). The color of each triangle denotes the location of the remaining H on the second site: O1 (red), O2 (purple), O3 (blue), and O4 (green). The configuration of the most acidic protons for each site combination by NH_3 BE is marked near its representative point, and the deprotonated O atom on the A site is underlined.

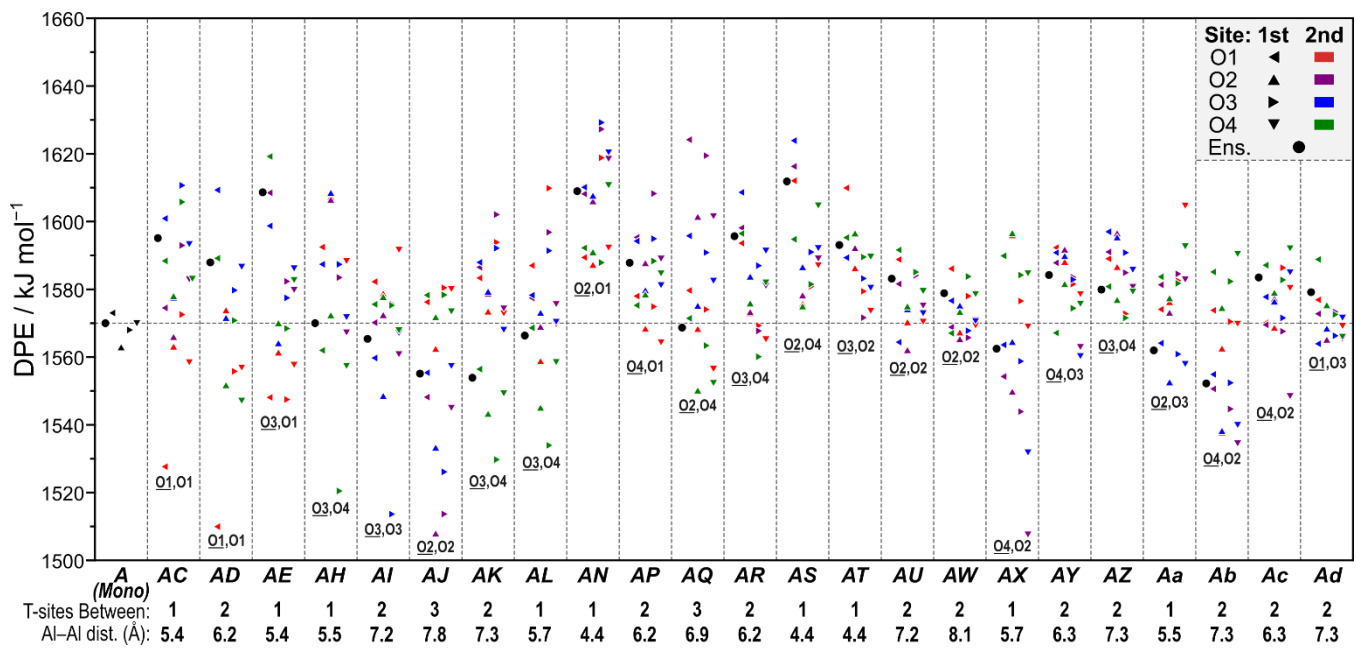


Figure A-4. The DPE for the isolated acid site and all site-pairs where the second site has NH₃ adsorbed, with the number of Si linkers between each site and the distance in Å between the T-atoms of each site shown below. Circles represent ensemble average DPE for each site-pair. The dashed line marks the ensemble average DPE of the isolated site and triangles mark individual DPE for each configuration. The direction of each triangle indicates the O atom from which the H was removed: O1 (◀), O2 (▲), O3 (▶), and O4 (▼). The color of each triangle denotes the location of the NH₃ on the second site: O1 (red), O2 (purple), O3 (blue), and O4 (green). The configuration of the most acidic protons for each site combination by DPE is marked near its representative point, and the deprotonated O atom on the A site is underlined.

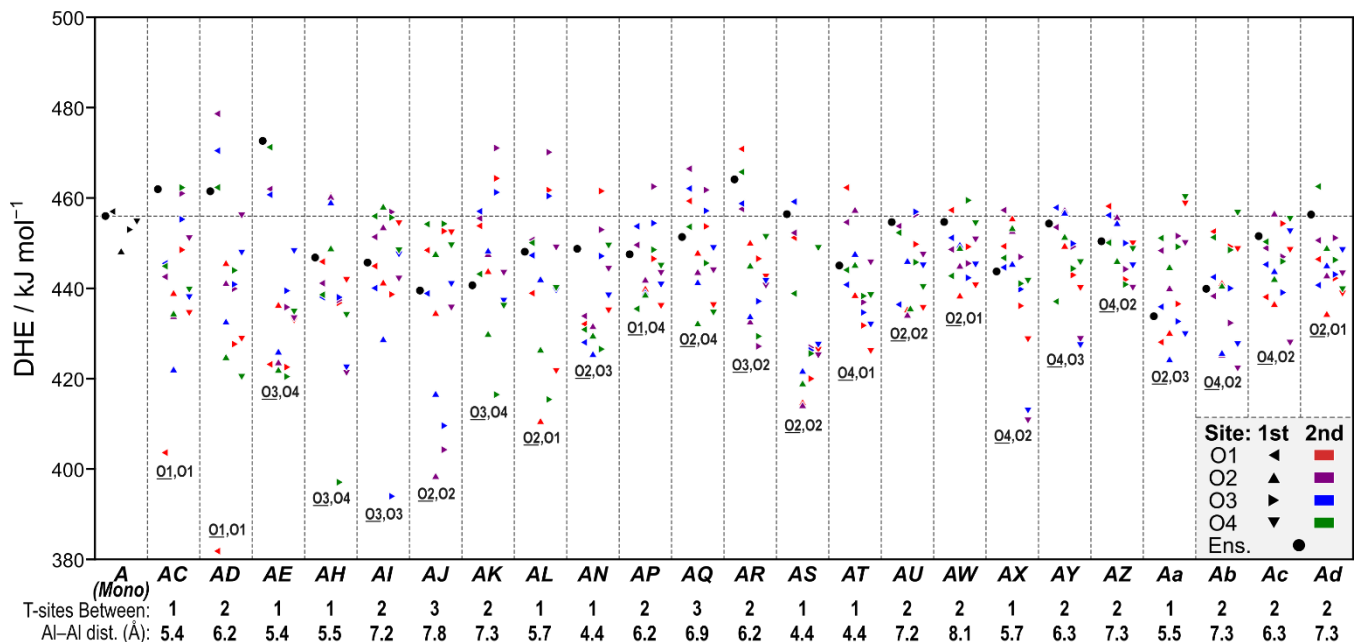


Figure A-5. The DHE for the isolated acid site and all site-pairs where the second site has NH_3 adsorbed, with the number of Si linkers between each site and the distance in Å between the T-atoms of each site shown below. Circles represent ensemble average DHE for each site-pair. The dashed line marks the ensemble average DHE of the isolated site and triangles mark individual DHE for each configuration. The direction of each triangle indicates the O atom from which the H was removed: O1 (\blacktriangleleft), O2 (\blacktriangleup), O3 (\blacktriangleright), and O4 (\blacktriangledown). The color of each triangle denotes the location of the NH_3 on the second site: O1 (red), O2 (purple), O3 (blue), and O4 (green). The configuration of the most acidic protons for each site combination by DHE is marked near its representative point, and the deprotonated O atom on the A site is underlined.

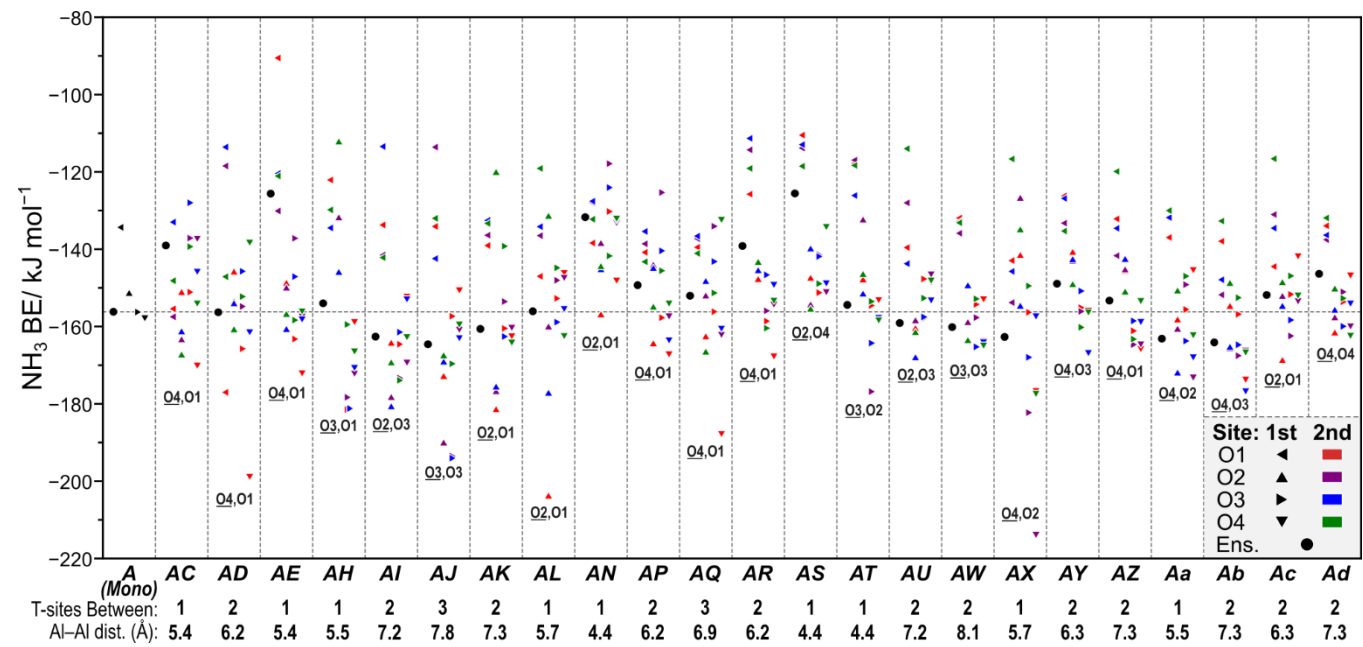


Figure A-6. The NH_3 BE for the isolated acid site and all site-pairs where the second site has NH_3 adsorbed, with the number of Si linkers between each site and the distance in Å between the T-atoms of each site shown below. Circles represent ensemble average NH_3 BE for each site-pair. The dashed line marks the ensemble average NH_3 BE of the isolated site and triangles mark individual NH_3 BE for each configuration. The direction of each triangle indicates the O atom from which the H was removed: O1 (\blacktriangleleft), O2 (\blacktriangleup), O3 (\blacktriangleright), and O4 (\blacktriangledown). The color of each triangle denotes the location of the NH_3 on the second site: O1 (red), O2 (purple), O3 (blue), and O4 (green). The configuration of the most acidic protons for each site combination by NH_3 BE is marked near its representative point, and the deprotonated O atom on the A site is underlined.

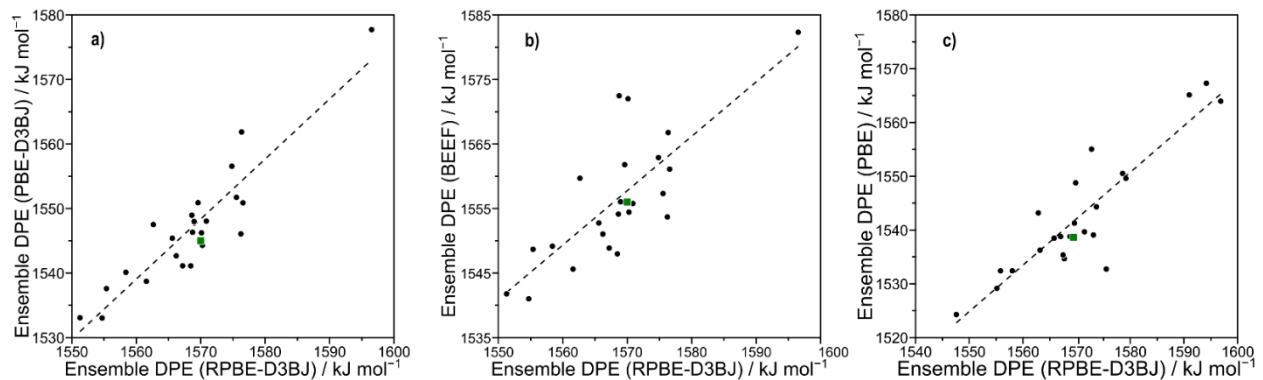


Figure A-7. Comparison of the DPE values between RPBE-D3BJ and **a)** PBE-D3BJ, **b)** BEEF-vdW, and **c)** PBE (without dispersion correction) functionals. The green dot represents ensemble DPE values of the isolated site. The values in part **c)** were optimized such that forces on each atom were less than $0.05 \text{ eV } \text{\AA}^{-1}$, while those in parts **a)** and **b)** were optimized such that the forces on each atom were less than $0.01 \text{ eV } \text{\AA}^{-1}$.

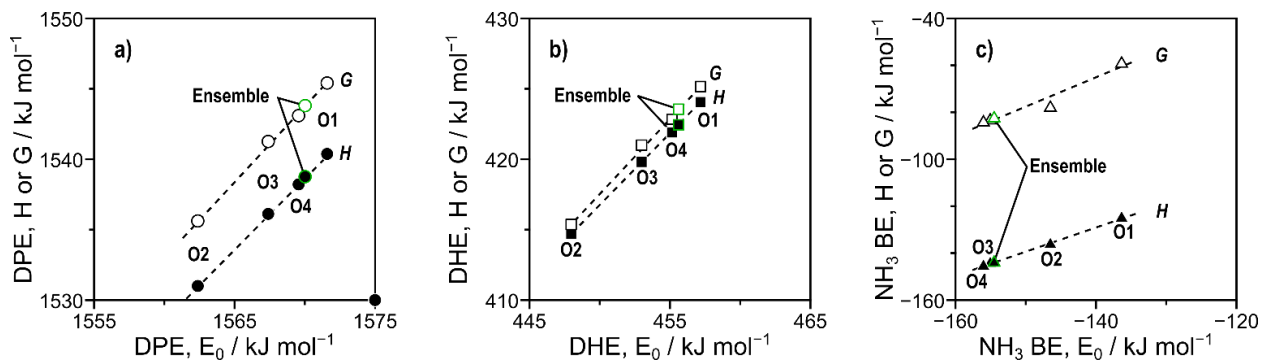


Figure A-8. The linear relationship between **a)** electronic DPE and DPE enthalpies (filled) and free energies (hollow), **b)** electronic DHE and DHE enthalpies (filled) and free energies (hollow), and **c)** NH_3 BE and NH_3 BE enthalpies (filled) and free energies (hollow). Dashed lines represent linear fits and ensemble energies are represented by points outlined in green.

The artifacts associated with periodic calculations of charged systems and the strong dipoles created by the presence of a charge-neutralizing background charge were explored through a series of calculations designed to understand what factors influence these artifacts. The effects of acid site and anion position were examined by forming a single Brønsted acid site at multiple crystallographically identical T-sites in CHA. These acids should give identical DPE values, but their DPE varied by 1.4 kJ mol^{-1} across the six T-sites (*A* through *F*, Figure 1 in the main text) examined, with an average of $1568.2 \text{ kJ mol}^{-1}$ (Figure S8). Next, we examined the effects of centering the anion within the unit cell for each of the six T-sites tested, which alters the composition and charge density at the unit cell boundary. These values should also be identical, but instead they varied by 1.3 kJ mol^{-1} and had a higher average value ($1569.0 \text{ kJ mol}^{-1}$) than the

previous set, indicating that the position of the acid site and resulting anion have small impacts ($1\text{--}2 \text{ kJ mol}^{-1}$) on calculated DPE values. These calculations were first performed with convergence criteria where the maximum force on any atom was $< 0.05 \text{ eV \AA}^{-1}$ and repeated with lower convergence criteria ($< 0.01 \text{ eV \AA}^{-1}$) to compare the precision of the two calculations and the impact of boundary conditions on the results for both criteria. The spread of energies for these calculations significantly decreased from $\sim 1.3 \text{ kJ mol}^{-1}$ to $< 0.2 \text{ kJ mol}^{-1}$ with stricter convergence criteria and the average DPE values were close to 1570 kJ mol^{-1} (Figure S8). While these tighter convergence criteria did reduce the effects of charge location artifacts and altered DPE values, the effects ($1\text{--}2 \text{ kJ mol}^{-1}$) were still significantly less than the errors inherent in DFT methods ($\sim 5\text{--}10 \text{ kJ mol}^{-1}$).

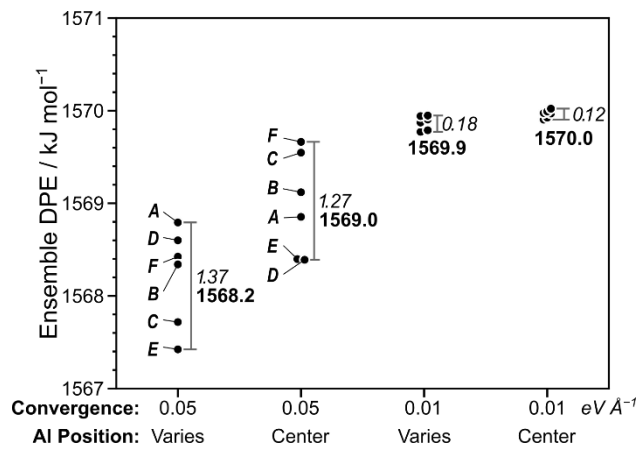


Figure A-9. Effects of varying the location of the Al site in the CHA framework (sites A–F), the position of the framework relative to the unit cell (by shifting those sites to the center of the unit cell), and the convergence criteria for optimizations (both 0.05 and 0.01 eV \AA^{-1} were used as force maxima). The ensemble DPE values are calculated using Eq. 6 for the four O atom locations of the proton for each acid site.

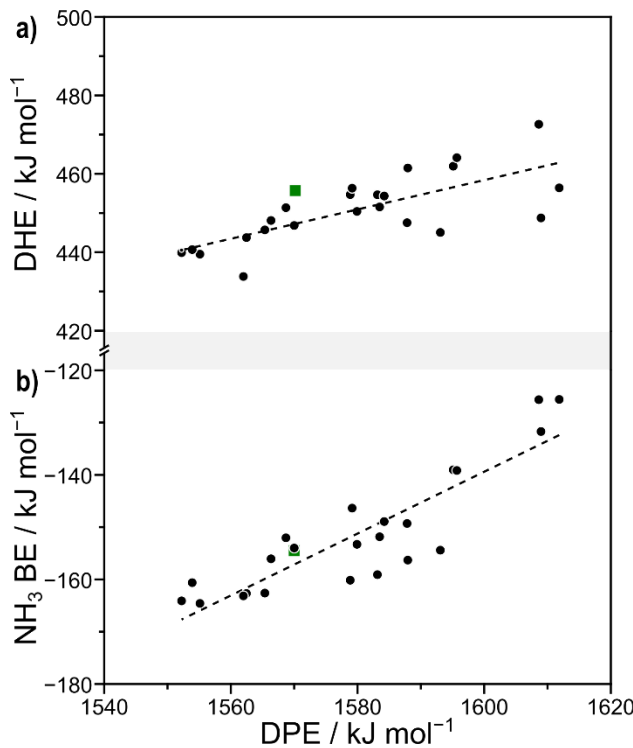


Figure A-10. The relationship between **a)** DPE and DHE and **b)** DPE and NH₃ BE for all site-pairs where the second site has NH₃ adsorbed. Energies shown are ensemble averages for each measurement of acid strength in kJ mol⁻¹. Dashed lines represent linear fits.

A-11. Statistical mechanics approximations for rate and equilibrium constants

Enthalpies (H) and free energies (G) for gas-phase and adsorbed species are calculated as a sum of DFT-calculated electronic energy (E0), zero-point vibrational energy (ZPVE), and vibrational, translational, and rotational enthalpies (Hvib, Htrans, Hrot) and free energies (Gvib, Gtrans, Grot):

$$H = E0 + ZPVE + Hvib + Htrans + Hrot$$

$$G = E0 + ZPVE + Gvib + Gtrans + Grot$$

Motions of adsorbates within the zeolite framework were considered frustrated movements and only contributed to vibrational terms such that translational and rotational H and G were zero. Framework Al atoms and the four O atoms bound to them

were included in normal mode analysis, but all remaining framework Si and O atoms remained static during frequency calculations. Vibrational, rotational, and translational energies were calculated from statistical mechanics⁷:

$$ZPVE = \sum (1/2 i \hbar v_i)$$

$$H_{vib} = \sum (hv_{ie} - h\nu_i k_B T \ln(1/e^{-h\nu_i k_B T}))$$

$$G_{vib} = \sum (-k_B T \ln(1/(1/e^{-h\nu_i k_B T})))$$

Translational and rotational free energies and enthalpies were calculated for all gas-phase species:

$$H_{trans} = 5/2 k_B T$$

$$H_{rot, linear} = k_B T$$

$$H_{rot, nonlinear} = 3/2 k_B T$$

$$G_{trans} = -k_B T \ln((2\pi M k_B T)^{1/2} / (3/2 V))$$

$$G_{rot} = -k_B T \ln(\pi/2 \sigma (T^{3/2} \theta_x \theta_y \theta_z)^{1/2})$$

$$\theta_i = h/2 \cdot 8\pi^2 k_B I_i$$

where I_i is the moment of inertia about each axis and σ is the symmetry number.

Entropies (S) are calculated from H and G :

$$S = H - G/T$$

G values at a wide range of temperatures (300–500 K) were estimated from H and S values calculated at 415 K. Rate constants can be approximated from DFT-calculated enthalpies and free energies at a range of temperatures using statistical mechanics formalisms:

$$k = k_B T / \exp(-\Delta G_f / k_B T)$$

$$K = \exp(-\Delta G_{ads} / k_B T)$$

where k_B is Boltzmann's constant. Rate and equilibrium constants are calculated at standard pressures (1 bar CH₃OH).

A-12. Comparison of dissociative and associative mechanisms without spectating methanol molecules Methanol dehydration, if it proceeds via the dissociative route, can be limited by either of the two steps in that pathway. The relative rates of the two pathways can be assessed by computing rates using a maximum rate or by comparing the forward and reverse reactions possible from a surface methyl group. A surface methyl group during methanol dehydration can either (1) react with water to re-form methanol or (2) react with another methanol to form dimethyl ether (DME). Coefficients of adsorption in the presence of a CH₃-Z species for H₂O (KW-M) and CH₃OH (KM-M) define adsorption steps prior to reaction to form DME ($kD2$) or to re-form methanol ($k-D1$). The possible routes to remove a surface methyl (CH₃-Z) group during methanol dehydration. Based on the paths described, rate equations can be derived to describe the formation of methanol from this surface methyl: $r-D1 = k-D1KW-MPH2O$ or to describe the formation of DME: $rD2 = kD2KM-MPCCH3OH$ The ratios of these rates can be written as a function of conversion (X) to compare the relative rates of these two steps and determine the rate-determining step (RDS) of the dissociative mechanism:

$$r-D1 \ rD2 = k-D1KW-M \ kD2KM-M (X \ 1-X)$$

Using energies calculated from DFT, these rate and equilibrium constants can be calculated from statistical mechanics formalisms (415 K, 1 bar CH₃OH). Ultimately, the ratio of these rate and equilibrium coefficients reflects the difference in energy between the two transition states:

$$k-D1KW-M \ kD2KM-M = \exp (-(\Delta GD1 \pm -\Delta GD2 \pm) kBT)$$

These calculated values

were used to estimate the ratio of rates of methanol formation and DME formation from a CH₃-Z group at different conversions using Eq. A.17. The rate of the second step of the dissociative mechanism exceeds the reverse rate of the first step by at least a factor of 10 at all conversions tested experimentally. This indicates that the first step of the dissociative route can be considered irreversible and is the RDS at all relevant catalytic conditions when spectating methanol species are excluded. Ratio of rates of the two possible rate-determining steps in dissociative methanol dehydration at 415 K. The maximum conversion tested experimentally is marked with a dashed line. The relative rates of the dissociative mechanism (which is limited by its first step at relevant conditions) and the associative mechanism can be compared using maximum rate analysis. DFTcalculated enthalpies and entropies can be used to approximate rate and equilibrium constants at standard conditions, from which rates can be estimated using the appropriate rate equations. The rate equation for the dissociative mechanism without spectators and without considering anything larger than a methanol dimer as a most abundant surface intermediate (MASI) is: $rD1 = kD1KMPM \frac{1}{1+KMPM+KMKDPM} 2$

The rate equation for the associative mechanism with the same assumptions is $rA = kAKMKDPM \frac{2}{1+KMPM+KMKDPM} 2$ The ratio of these two rates, therefore, is $\frac{rD}{rA} = \frac{kD}{kA} \frac{KMPM+KMKDPM}{AKDPM}$ The ratio of these rate coefficients reflects the differences in free energy between the dissociative ($\Delta GD1 \neq 0$) and associative ($\Delta GA \neq 0$) transition states and a methanol dimer structure (ΔGD): $kD/kA = \exp(-(\Delta GD1 \pm \Delta GA \mp \Delta GD)/kBT)$ The dissociative mechanism prevails at low methanol pressures, but the associative mechanism dominates at higher pressures. The pressure at which the prevalent mechanism shifts from dissociative to associative increases with increasing

temperature. This reflects differences in S₈ enthalpic and entropic contributions to relevant free energies; the associative mechanism is enthalpically favored but entropically disfavored as adsorption of additional methanol molecules results in entropic losses. This is consistent with previous work which has found a preference for the dissociative mechanism at elevated reaction temperatures in MFI [5] and on polyoxometalates [6] due to entropic contributions to the free energies for these mechanisms. Figure A-6. (a) DFT-predicted rates of dissociative (dashed lines) and associative (solid lines) methanol dehydration without spectators and excluding intermediates larger than two methanol molecules at 415 K (blue), 433 K (green), 450 K (orange), and 473 K (red). (b) Ratios of the dissociative and associative rates of DME formation at these temperatures, with the pressures at which the prevailing route shifts from dissociative to associative labeled in kPa.

APPENDIX B SUPPORTING INFORMATION FOR CHAPTER 3

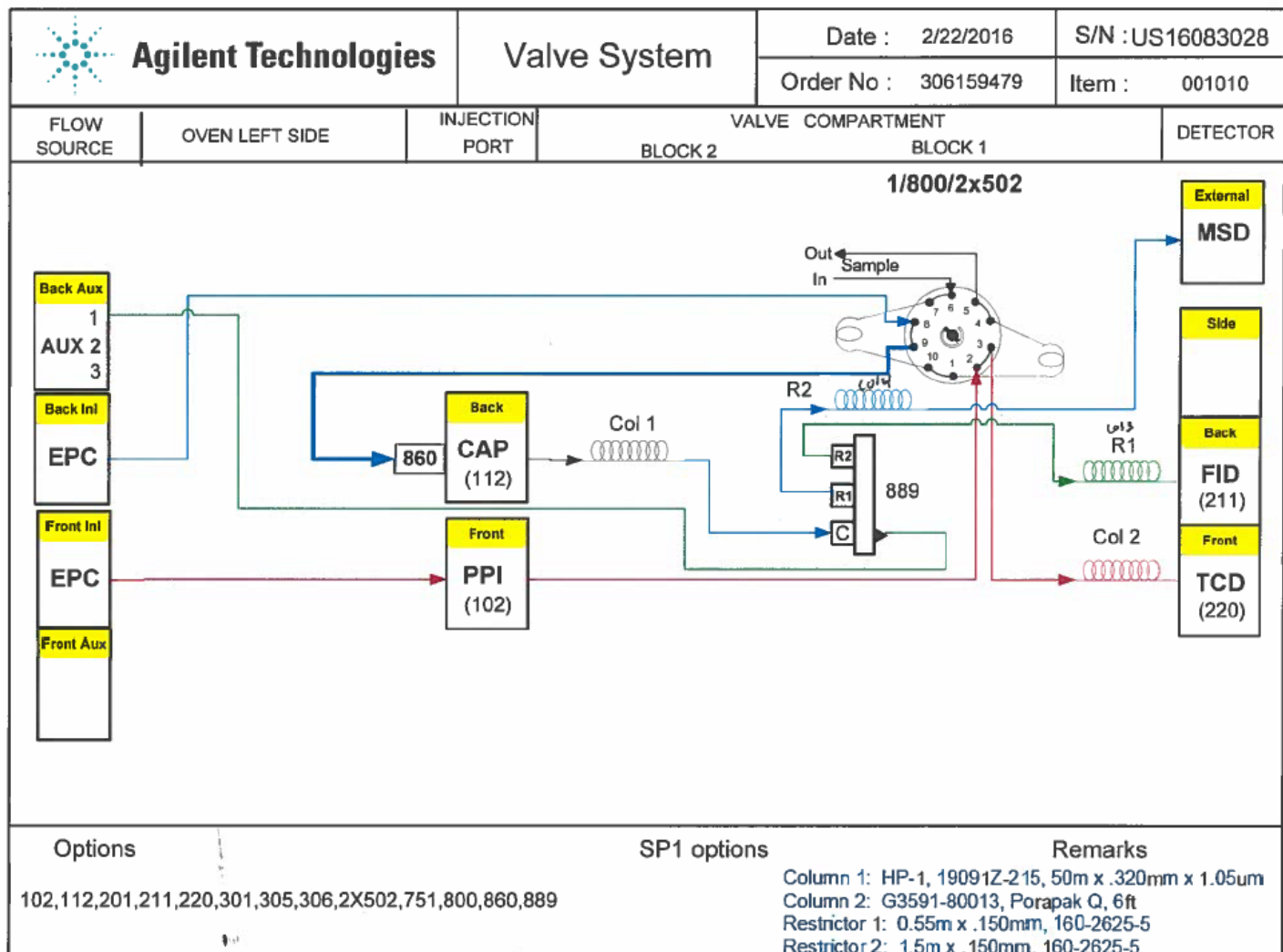


Figure B-1. The flow schematic and instrumentation setup for the GC (7890N) – MS (5788B).

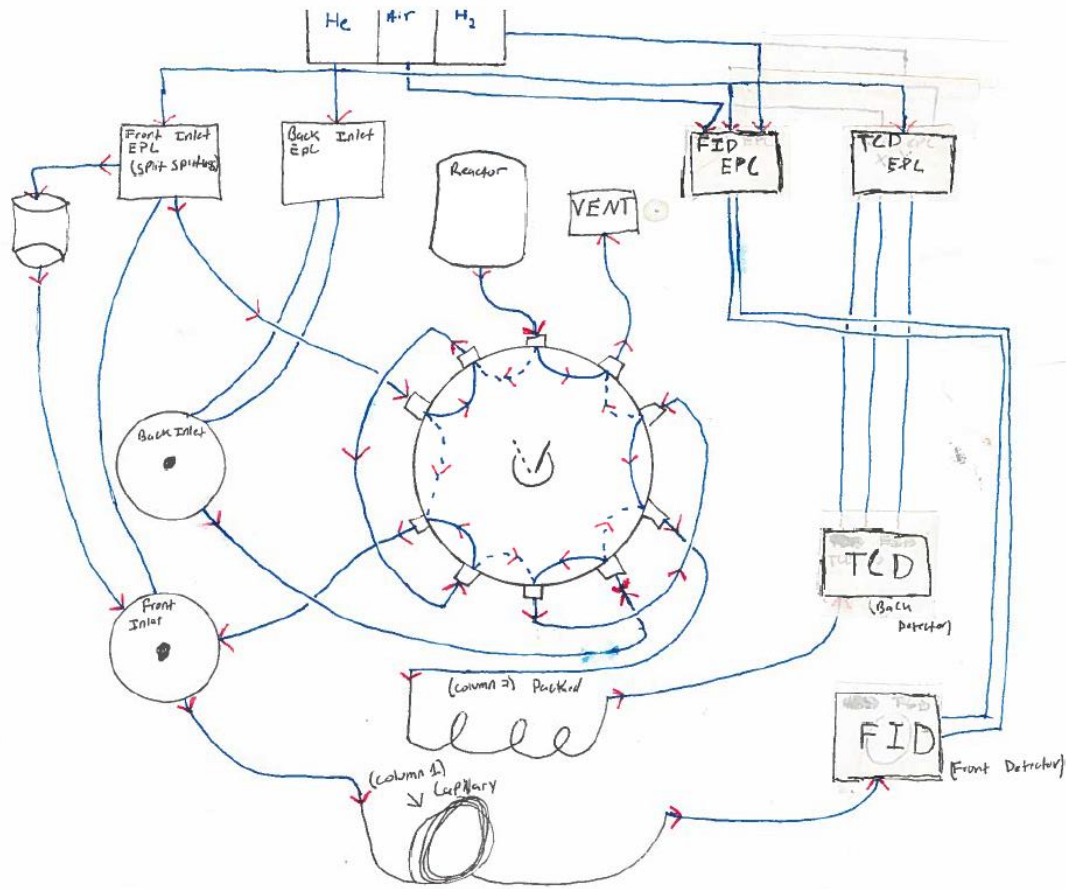


Figure B-2. The flow schematic and instrumentation setup for the GC (6890N).

APPENDIX C
SUPPORTING INFORMATION FOR CHAPTER 4

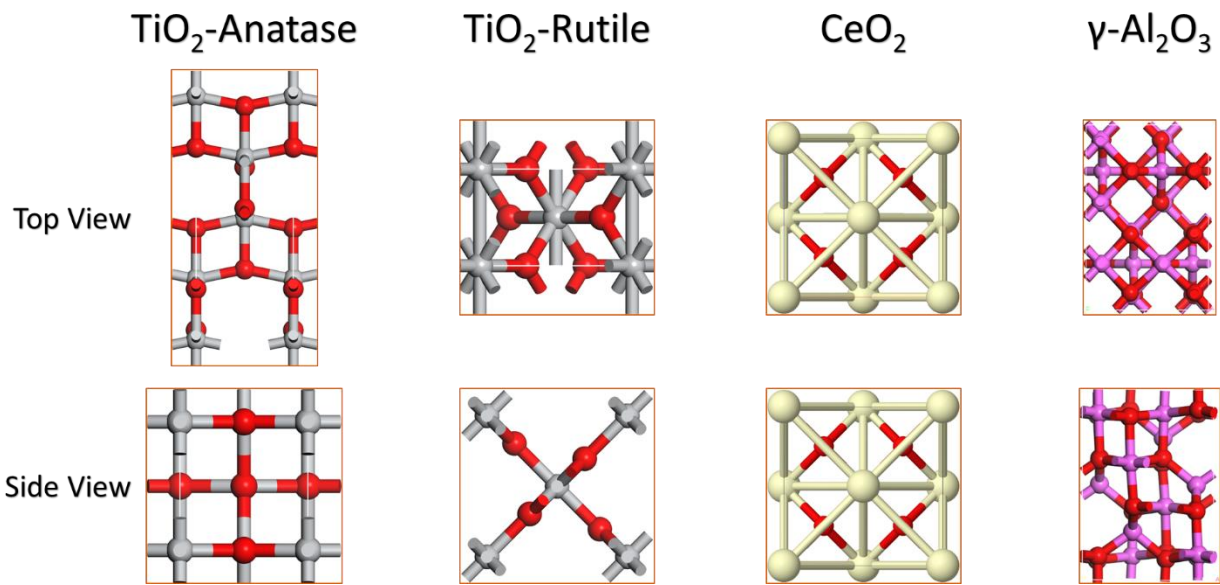


Figure C-1. Bulk structures for TiO₂, CeO₂, and Al₂O₃ after optimizing in VASP

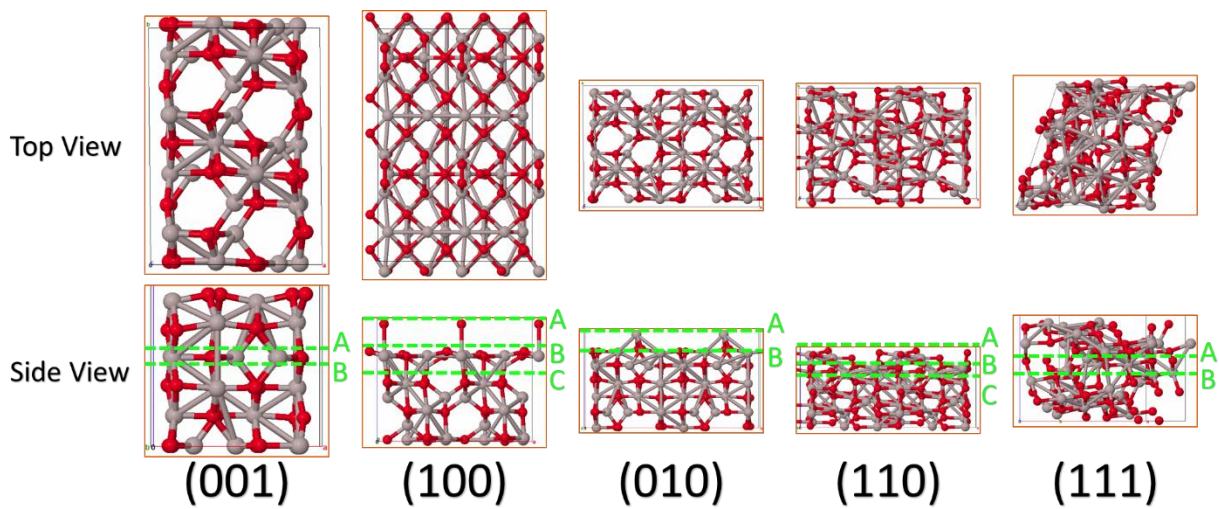


Figure C-2. γ-Al₂O₃ surfaces and terminations before optimization.

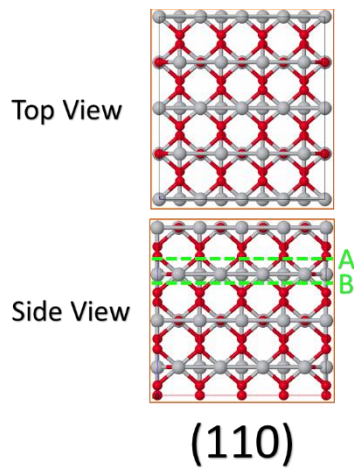


Figure C-3. TiO_2 rutile surface and terminations before optimization.

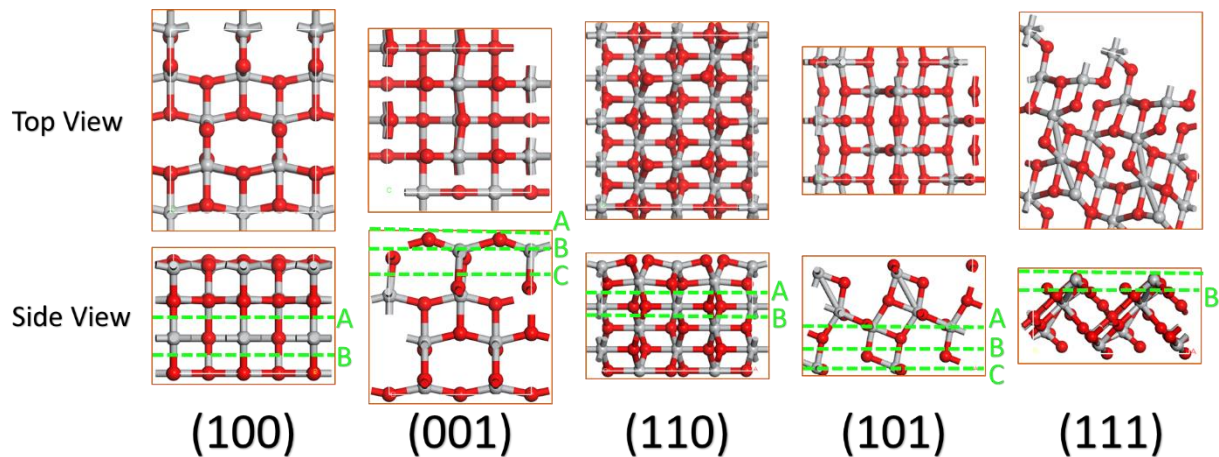


Figure C-4. TiO_2 anatase surfaces and terminations before optimization.

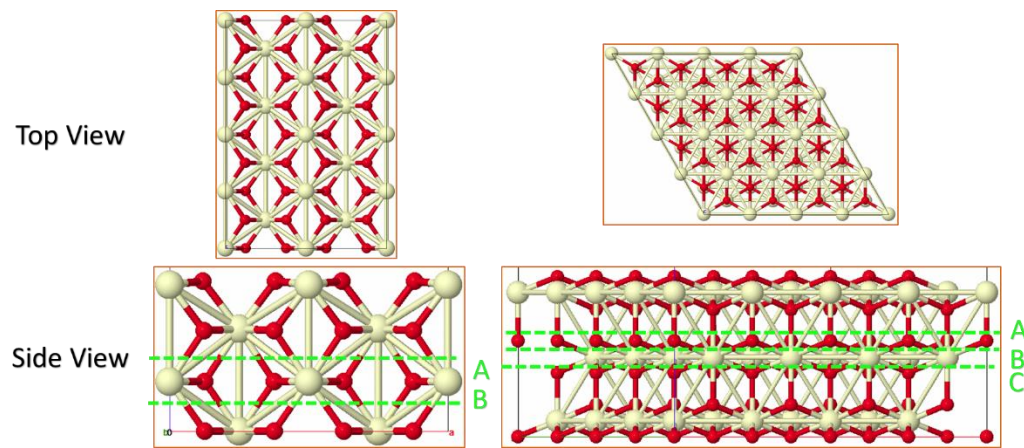


Figure C-5. CeO_2 surfaces and terminations before optimization.

LIST OF REFERENCES

- (1) International Energy Agency. *World Energy Outlook 2019*; World Energy Outlook; OECD, 2019.
- (2) Karl, T. R.; Trenberth, K. E. Modern Global Climate Change. *Science* **2003**, *302*, 1719–1723.
- (3) Demirbas, A. Political, Economic and Environmental Impacts of Biofuels: A Review. *Appl. Energy* **2009**, *86*, S108–S117.
- (4) HABER & BOSCH - Haber-Bosch process
<http://people.idsia.ch/~juergen/haberbosch.html> (accessed Nov 22, 2019).
- (5) de Klerk, A. Fischer-Tropsch Process. In *Kirk-Othmer Encyclopedia of Chemical Technology*; John Wiley & Sons, Inc., Ed.; John Wiley & Sons, Inc.: Hoboken, NJ, USA, 2000.
- (6) Stöcker, M. Methanol-to-hydrocarbons: Catalytic Materials and Their Behavior. *Micropor. Mesopor. Mat.* **1999**, *29*, 3–48.
- (7) Chang, C.; Silvestri, A. The Conversion of Methanol and Other O-compounds to Hydrocarbons over Zeolite Catalysts. *J. Catal.* **1977**, *47*, 249–259.
- (8) Chang, C. D.; Kuo, J. C. W.; Lang, W. H.; Jacob, S. M.; Wise, J. J.; Silvestri, A. J. Process Studies on the Conversion of Methanol to Gasoline. *Ind. Eng. Chem. Proc. Des. Dev.* **1978**, *17*, 255–260.
- (9) Arean, C. O.; Delgado, M. R.; Nachtigall, P.; Thang, H. V.; Rubeš, M.; Bulánek, R.; Chlubná-Eliášová, P. Measuring the Brønsted Acid Strength of Zeolites—does It Correlate with the O-H Frequency Shift Probed by a Weak Base? *Phys. Chem. Chem. Phys.* **2014**, *16*, 10129–10141.
- (10) Schallmoser, S.; Ikuno, T.; Wagenhofer, M. F.; Kolvenbach, R.; Haller, G. L.; Sanchez-Sanchez, M.; Lercher, J. A. Impact of the Local Environment of Brønsted Acid Sites in ZSM-5 on the Catalytic Activity in N-pentane Cracking. *J. Catal.* **2014**, *316*, 93–102.
- (11) Song, C.; Chu, Y.; Wang, M.; Shi, H.; Zhao, L.; Guo, X.; Yang, W.; Shen, J.; Xue, N.; Peng, L.; et al. Cooperativity of Adjacent Brønsted Acid Sites in MFI Zeolite Channel Leads to Enhanced Polarization and Cracking of Alkanes. *J. Catal.* **2017**, *349*, 163–174.
- (12) Wang, S.; Iglesia, E. Mechanism of Isobutanal–isobutene Prins Condensation Reactions on Solid Brønsted Acids. *ACS Catal.* **2016**, *6*, 7664–7684.

- (13) Gounder, R.; Iglesia, E. The Catalytic Diversity of Zeolites: Confinement and Solvation Effects Within Voids of Molecular Dimensions. *Chem. Commun.* **2013**, 49, 3491–3509.
- (14) Jones, A. J.; Zones, S. I.; Iglesia, E. Implications of Transition State Confinement Within Small Voids for Acid Catalysis. *J. Phys. Chem. C* **2014**, 118, 17787–17800.
- (15) Zalazar, M. F.; Cabral, N. D.; Romero Ojeda, G. D.; Alegre, C. I. A.; Peruchena, N. M. Confinement Effects in Protonation Reactions Catalyzed by Zeolites with Large Void Structures. *J. Phys. Chem. C* **2018**, 122, 27350–27359.
- (16) Jones, A. J.; Iglesia, E. The Strength of Brønsted Acid Sites in Microporous Aluminosilicates. *ACS Catal.* **2015**, 5, 5741–5755.
- (17) Gounder, R.; Iglesia, E. The Roles of Entropy and Enthalpy in Stabilizing Ion-pairs at Transition States in Zeolite Acid Catalysis. *Acc. Chem. Res.* **2012**, 45, 229–238.
- (18) Bates, J. S.; Bukowski, B. C.; Harris, J. W.; Greeley, J. P.; Gounder, R. Distinct Catalytic Reactivity of Sn Substituted in Framework Locations and at Defect Grain Boundaries in Sn-Zeolites. *ACS Catal.* **2019**.
- (19) Di Iorio, J. R.; Nimlos, C. T.; Gounder, R. Introducing Catalytic Diversity into Single-Site Chabazite Zeolites of Fixed Composition via Synthetic Control of Active Site Proximity. *ACS Catal.* **2017**, 7, 6663–6674.
- (20) Knott, B. C.; Nimlos, C. T.; Robichaud, D. J.; Nimlos, M. R.; Kim, S.; Gounder, R. Consideration of the Aluminum Distribution in Zeolites in Theoretical and Experimental Catalysis Research. *ACS Catal.* **2017**, 8, 770–784.
- (21) Nystrom, S.; Hoffman, A.; Hibbitts, D. Tuning Brønsted Acid Strength by Altering Site Proximity in CHA Framework Zeolites. *ACS Catal.* **2018**, 8, 7842–7860.
- (22) Hibbitts, D.; Tan, Q.; Neurock, M. Acid Strength and Bifunctional Catalytic Behavior of Alloys Comprised of Noble Metals and Oxophilic Metal Promoters. *J. Catal.* **2014**, 315, 48–58.
- (23) Tomishige, K.; Tamura, M.; Nakagawa, Y. Role of Re Species and Acid Cocatalyst on Ir-ReO_x /SiO₂ in the C-O Hydrogenolysis of Biomass-derived Substrates. *Chem. Rec.* **2014**, 14, 1041–1054.
- (24) Knaeble, W.; Iglesia, E. Acid Strength and Metal-acid Proximity Effects on Methylcyclohexane Ring Contraction Turnover Rates and Selectivities. *J. Catal.* **2016**, 344, 817–830.
- (25) Chia, M.; Pagán-Torres, Y. J.; Hibbitts, D.; Tan, Q.; Pham, H. N.; Datye, A. K.; Neurock, M.; Davis, R. J.; Dumesic, J. A. Selective Hydrogenolysis of Polyols

- and Cyclic Ethers over Bifunctional Surface Sites on Rhodium-rhenium Catalysts. *J. Am. Chem. Soc.* **2011**, *133*, 12675–12689.
- (26) Parikka, M. Global Biomass Fuel Resources. *Biomass and Bioenergy* **2004**, *27*, 613–620.
- (27) Rangarajan, S.; Bhan, A.; Daoutidis, P. Identification and Analysis of Synthesis Routes in Complex Catalytic Reaction Networks for Biomass Upgrading. *Appl. Catal. B* **2014**, *145*, 149–160.
- (28) Joensen, F.; Nielsen, P. E. H.; Palis Sørensen, M. D. Biomass to Green Gasoline and Power. *Biomass Conv. Bioref.* **2011**, *1*, 85–90.
- (29) Nakagawa, Y.; Tomishige, K. Catalyst Development for the Hydrogenolysis of Biomass-Derived Chemicals to Value-Added Ones. *Catal. Surv. Asia* **2011**, *15*, 111–116.
- (30) Shen, H.; Shamim, T.; Sengupta, S. An Investigation of Catalytic Converter Performances During Cold Starts. In *SAE Technical Paper Series*; SAE technical paper series; SAE International: 400 Commonwealth Drive, Warrendale, PA, United States, 1999; Vol. 1.
- (31) Takahashi, N.; Shinjoh, H.; Iijima, T.; Suzuki, T.; Yamazaki, K.; Yokota, K.; Suzuki, H.; Miyoshi, N.; Matsumoto, S.; Tanizawa, T.; et al. The New Concept 3-way Catalyst for Automotive Lean-burn Engine: NO_x Storage and Reduction Catalyst. *Catal. Today* **1996**, *27*, 63–69.
- (32) Matsubu, J. C.; Yang, V. N.; Christopher, P. Isolated Metal Active Site Concentration and Stability Control Catalytic CO₂ Reduction Selectivity. *J. Am. Chem. Soc.* **2015**, *137*, 3076–3084.
- (33) Matsubu, J. C.; Zhang, S.; DeRita, L.; Marinkovic, N. S.; Chen, J. G.; Graham, G. W.; Pan, X.; Christopher, P. Adsorbate-mediated Strong Metal-support Interactions in Oxide-supported Rh Catalysts. *Nat. Chem.* **2017**, *9*, 120–127.
- (34) Resasco, J.; Dai, S.; Graham, G.; Pan, X.; Christopher, P. Combining *In-Situ* Transmission Electron Microscopy and Infrared Spectroscopy for Understanding Dynamic and Atomic-Scale Features of Supported Metal Catalysts. *J. Phys. Chem. C* **2018**, *122*, 25143–25157.
- (35) DeRita, L.; Resasco, J.; Dai, S.; Boubnov, A.; Thang, H. V.; Hoffman, A. S.; Ro, I.; Graham, G. W.; Bare, S. R.; Pacchioni, G.; et al. Structural Evolution of Atomically Dispersed Pt Catalysts Dictates Reactivity. *Nat. Mater.* **2019**, *18*, 746–751.
- (36) DeRita, L.; Dai, S.; Lopez-Zepeda, K.; Pham, N.; Graham, G. W.; Pan, X.; Christopher, P. Catalyst Architecture for Stable Single Atom Dispersion Enables Site-Specific Spectroscopic and Reactivity Measurements of CO Adsorbed to Pt

- Atoms, Oxidized Pt Clusters, and Metallic Pt Clusters on TiO₂. *J. Am. Chem. Soc.* **2017**, *139*, 14150–14165.
- (37) Corma, A. Inorganic Solid Acids and Their Use in Acid-Catalyzed Hydrocarbon Reactions. *Chem. Rev.* **1995**, *95*, 559–614.
- (38) Corma, A.; Orchillés, A. V. Current Views on the Mechanism of Catalytic Cracking. *Micropor. Mesopor. Mat.* **2000**, *35*-36, 21–30.
- (39) Davis, M. E. Design for Sieving. *Nature* **1996**, *382*, 583–585.
- (40) Davis, M. E. Ordered Porous Materials for Emerging Applications. *Nature* **2002**, *417*, 813–821.
- (41) Bein, T. Synthesis and Applications of Molecular Sieve Layers and Membranes. *Chem. Mater.* **1996**, *8*, 1636–1653.
- (42) Haldoupis, E.; Nair, S.; Sholl, D. S. Pore Size Analysis of Aaa503250,000 Hypothetical Zeolites. *Phys. Chem. Chem. Phys.* **2011**, *13*, 5053–5060.
- (43) First, E. L.; Gounaris, C. E.; Wei, J.; Floudas, C. A. Computational Characterization of Zeolite Porous Networks: An Automated Approach. *Phys. Chem. Chem. Phys.* **2011**, *13*, 17339–17358.
- (44) Jones, A. J.; Ostrouchov, C.; Haranczyk, M.; Iglesia, E. From Rays to Structures: Representation and Selection of Void Structures in Zeolites Using Stochastic Methods. *Micropor. Mesopor. Mat.* **2013**, *181*, 208–216.
- (45) Pophale, R.; Cheeseman, P. A.; Deem, M. W. A Database of New Zeolite-like Materials. *Phys. Chem. Chem. Phys.* **2011**, *13*, 12407–12412.
- (46) Deem, M. W.; Pophale, R.; Cheeseman, P. A.; Earl, D. J. Computational Discovery of New Zeolite-Like Materials. *J. Phys. Chem. C* **2009**, *113*, 21353–21360.
- (47) Jones, A. J.; Carr, R. T.; Zones, S. I.; Iglesia, E. Acid Strength and Solvation in Catalysis by MFI Zeolites and Effects of the Identity, Concentration and Location of Framework Heteroatoms. *J. Catal.* **2014**, *312*, 58–68.
- (48) Gounder, R.; Jones, A. J.; Carr, R. T.; Iglesia, E. Solvation and Acid Strength Effects on Catalysis by Faujasite Zeolites. *J. Catal.* **2012**, *286*, 214–223.
- (49) Gounder, R.; Iglesia, E. Catalytic Consequences of Spatial Constraints and Acid Site Location for Monomolecular Alkane Activation on Zeolites. *J. Am. Chem. Soc.* **2009**, *131*, 1958–1971.
- (50) Carr, R. T.; Neurock, M.; Iglesia, E. Catalytic Consequences of Acid Strength in the Conversion of Methanol to Dimethyl Ether. *J. Catal.* **2011**, *278*, 78–93.

- (51) Knaeble, W.; Carr, R. T.; Iglesia, E. Mechanistic Interpretation of the Effects of Acid Strength on Alkane Isomerization Turnover Rates and Selectivity. *J. Catal.* **2014**, *319*, 283–296.
- (52) Knaeble, W.; Iglesia, E. Kinetic and Theoretical Insights into the Mechanism of Alkanol Dehydration on Solid Brønsted Acid Catalysts. *J. Phys. Chem. C* **2016**, *120*, 3371–3389.
- (53) Macht, J.; Janik, M.; Neurock, M.; Iglesia, E. Catalytic Consequences of Composition in Polyoxometalate Clusters with Keggin Structure. *Angew. Chem. Int. Ed. Engl.* **2007**, *119*, 8010–8014.
- (54) Janik, M. J.; Macht, J.; Iglesia, E.; Neurock, M. Correlating Acid Properties and Catalytic Function: A First-Principles Analysis of Alcohol Dehydration Pathways on Polyoxometalates. *J. Phys. Chem. C* **2009**, *113*, 1872–1885.
- (55) Koso, S.; Nakagawa, Y.; Tomishige, K. Mechanism of the Hydrogenolysis of Ethers over Silica-supported Rhodium Catalyst Modified with Rhenium Oxide. *J. Catal.* **2011**, *280*, 221–229.
- (56) Shinmi, Y.; Koso, S.; Kubota, T.; Nakagawa, Y.; Tomishige, K. Modification of Rh/SiO₂ Catalyst for the Hydrogenolysis of Glycerol in Water. *Appl. Catal. B* **2010**, *94*, 318–326.
- (57) Chen, K.; Mori, K.; Watanabe, H.; Nakagawa, Y.; Tomishige, K. C–O Bond Hydrogenolysis of Cyclic Ethers with OH Groups over Rhenium-modified Supported Iridium Catalysts. *J. Catal.* **2012**, *294*, 171–183.
- (58) Koso, S.; Watanabe, H.; Okumura, K.; Nakagawa, Y.; Tomishige, K. Comparative Study of Rh–MoO_x and Rh–ReO_x Supported on SiO₂ for the Hydrogenolysis of Ethers and Polyols. *Appl. Catal. B* **2012**, *111-112*, 27–37.
- (59) Chatterjee, A.; Iwasaki, T.; Ebina, T.; Miyamoto, A. Density Functional Study for Estimating Brønsted Acid Site Strength in Isomorphously Substituted ZSM-5. *Micropor. Mesopor. Mat.* **1998**, *21*, 421–428.
- (60) Bhan, A.; Gounder, R.; Macht, J.; Iglesia, E. Entropy Considerations in Monomolecular Cracking of Alkanes on Acidic Zeolites. *J. Catal.* **2008**, *253*, 221–224.
- (61) Wang, S.; Iglesia, E. Catalytic Diversity Conferred by Confinement of Protons Within Porous Aluminosilicates in Prins Condensation Reactions. *J. Catal.* **2017**, *352*, 415–435.
- (62) Gounder, R.; Iglesia, E. Effects of Partial Confinement on the Specificity of Monomolecular Alkane Reactions for Acid Sites in Side Pockets of Mordenite. *Angew. Chem. Int. Ed. Engl.* **2010**, *49*, 808–811.

- (63) Zalazar, M. F.; Paredes, E. N.; Romero Ojeda, G. D.; Cabral, N. D.; Peruchena, N. M. Study of Confinement and Catalysis Effects of the Reaction of Methylation of Benzene by Methanol in H-Beta and H-ZSM-5 Zeolites by Topological Analysis of Electron Density. *J. Phys. Chem. C* **2018**, 122, 3350–3362.
- (64) Lesthaeghe, D.; Van Speybroeck, V.; Waroquier, M. Theoretical Evaluation of Zeolite Confinement Effects on the Reactivity of Bulky Intermediates. *Phys. Chem. Chem. Phys.* **2009**, 11, 5222–5226.
- (65) Zicovich-Wilson, C. M.; Corma, A.; Viruela, P. Electronic Confinement of Molecules in Microscopic Pores. A New Concept Which Contributes to the Explanation of the Catalytic Activity of Zeolites. *J. Phys. Chem.* **1994**, 98, 10863–10870.
- (66) Di Iorio, J. R.; Gounder, R. Controlling the Isolation and Pairing of Aluminum in Chabazite Zeolites Using Mixtures of Organic and Inorganic Structure-Directing Agents. *Chem. Mater.* **2016**, 28, 2236–2247.
- (67) Paolucci, C.; Parekh, A. A.; Khurana, I.; Di Iorio, J. R.; Li, H.; Albarracin Caballero, J. D.; Shih, A. J.; Anggara, T.; Delgass, W. N.; Miller, J. T.; et al. Catalysis in a Cage: Condition-Dependent Speciation and Dynamics of Exchanged Cu Cations in SSZ-13 Zeolites. *J. Am. Chem. Soc.* **2016**, 138, 6028–6048.
- (68) US20170107114A1 - Methods of synthesizing chabazite zeolites with controlled aluminum distribution and structures made therefrom - Google Patents <https://patents.google.com/patent/US20170107114A1/en> (accessed Jan 22, 2018).
- (69) Dědeček, J.; Sobálik, Z.; Wichterlová, B. Siting and Distribution of Framework Aluminium Atoms in Silicon-Rich Zeolites and Impact on Catalysis. *Catalysis Reviews* **2012**, 54, 135–223.
- (70) Yokoi, T.; Mochizuki, H.; Namba, S.; Kondo, J. N.; Tatsumi, T. Control of the Al Distribution in the Framework of ZSM-5 Zeolite and Its Evaluation by Solid-State NMR Technique and Catalytic Properties. *J. Phys. Chem. C* **2015**, 119, 15303–15315.
- (71) Bates, S. A.; Verma, A. A.; Paolucci, C.; Parekh, A. A.; Anggara, T.; Yezerets, A.; Schneider, W. F.; Miller, J. T.; Delgass, W. N.; Ribeiro, F. H. Identification of the Active Cu Site in Standard Selective Catalytic Reduction with Ammonia on Cu-SSZ-13. *J. Catal.* **2014**, 312, 87–97.
- (72) Jones, A. J.; Iglesia, E. Kinetic, Spectroscopic, and Theoretical Assessment of Associative and Dissociative Methanol Dehydration Routes in Zeolites. *Angew. Chem. Int. Ed. Engl.* **2014**, 53, 12177–12181.

- (73) Paolucci, C.; Khurana, I.; Parekh, A. A.; Li, S.; Shih, A. J.; Li, H.; Di Iorio, J. R.; Albarracin-Caballero, J. D.; Yezerets, A.; Miller, J. T.; et al. Dynamic Multinuclear Sites Formed by Mobilized Copper Ions in NO_x Selective Catalytic Reduction. *Science* **2017**, *357*, 898–903.
- (74) Di Iorio, J. R.; Bates, S. A.; Verma, A. A.; Delgass, W. N.; Ribeiro, F. H.; Miller, J. T.; Gounder, R. The Dynamic Nature of Brønsted Acid Sites in Cu-Zeolites During NO_x Selective Catalytic Reduction: Quantification by Gas-Phase Ammonia Titration. *Top. Catal.* **2015**, *58*, 424–434.
- (75) Paolucci, C.; Verma, A. A.; Bates, S. A.; Kispersky, V. F.; Miller, J. T.; Gounder, R.; Delgass, W. N.; Ribeiro, F. H.; Schneider, W. F. Isolation of the Copper Redox Steps in the Standard Selective Catalytic Reduction on Cu-SSZ-13. *Angew. Chem. Int. Ed. Engl.* **2014**, *53*, 11828–11833.
- (76) Bates, S. A.; Delgass, W. N.; Ribeiro, F. H.; Miller, J. T.; Gounder, R. Methods for NH₃ Titration of Brønsted Acid Sites in Cu-zeolites That Catalyze the Selective Catalytic Reduction of NO_x with NH₃. *J. Catal.* **2014**, *312*, 26–36.
- (77) Freysoldt, C.; Neugebauer, J.; Van de Walle, C. G. Fully Ab Initio Finite-size Corrections for Charged-defect Supercell Calculations. *Phys. Rev. Lett.* **2009**, *102*, 016402.
- (78) Yuan, S. P.; Wang, J. G.; Li, Y. W.; Jiao, H. Brønsted Acidity of Isomorphously Substituted ZSM-5 by B, Al, Ga, and Fe. Density Functional Investigations. *J. Phys. Chem. A* **2002**, *106*, 8167–8172.
- (79) Brand, H. V.; Curtiss, L. A.; Iton, L. E. Computational Studies of Acid Sites in ZSM 5: Dependence on Cluster Size. *J. Phys. Chem.* **1992**, *96*, 7725–7732.
- (80) Strodel, P.; Neyman, K. M.; Knözinger, H.; Rösch, N. Acidic Properties of [Al], [Ga] and [Fe] Isomorphously Substituted Zeolites. Density Functional Model Cluster Study of the Complexes with a Probe CO Molecule. *Chem. Phys. Lett.* **1995**, *240*, 547–552.
- (81) Svelle, S.; Tuma, C.; Rozanska, X.; Kerber, T.; Sauer, J. Quantum Chemical Modeling of Zeolite-catalyzed Methylation Reactions: Toward Chemical Accuracy for Barriers. *J. Am. Chem. Soc.* **2009**, *131*, 816–825.
- (82) Brändle, M.; Sauer, J. Acidity Differences Between Inorganic Solids Induced by Their Framework Structure. A Combined Quantum Mechanics/Molecular Mechanics Ab Initio Study on Zeolites. *J. Am. Chem. Soc.* **1998**, *120*, 1556–1570.
- (83) Mallikarjun Sharada, S.; Zimmerman, P. M.; Bell, A. T.; Head-Gordon, M. Insights into the Kinetics of Cracking and Dehydrogenation Reactions of Light Alkanes in H-MFI. *J. Phys. Chem. C* **2013**, *117*, 12600–12611.

- (84) Van der Mynsbrugge, J.; Janda, A.; Mallikarjun Sharada, S.; Lin, L.-C.; Van Speybroeck, V.; Head-Gordon, M.; Bell, A. T. Theoretical Analysis of the Influence of Pore Geometry on Monomolecular Cracking and Dehydrogenation of *n*-Butane in Brønsted Acidic Zeolites. *ACS Catal.* **2017**, *7*, 2685–2697.
- (85) Janda, A.; Vlaisavljevich, B.; Lin, L.-C.; Mallikarjun Sharada, S.; Smit, B.; Head-Gordon, M.; Bell, A. T. Adsorption Thermodynamics and Intrinsic Activation Parameters for Monomolecular Cracking Ofn -Alkanes on Brønsted Acid Sites in Zeolites. *J. Phys. Chem. C* **2015**, *119*, 10427–10438.
- (86) Grajciar, L.; Areán, C. O.; Pulido, A.; Nachtigall, P. Periodic DFT Investigation of the Effect of Aluminium Content on the Properties of the Acid Zeolite H-FER. *Phys. Chem. Chem. Phys.* **2010**, *12*, 1497–1506.
- (87) Suzuki, K.; Sastre, G.; Katada, N.; Niwa, M. Ammonia IRMS-TPD Measurements and DFT Calculation on Acidic Hydroxyl Groups in CHA-type Zeolites. *Phys. Chem. Chem. Phys.* **2007**, *9*, 5980–5987.
- (88) Lercher, J. A.; Gründling, C.; Eder-Mirth, G. Infrared Studies of the Surface Acidity of Oxides and Zeolites Using Adsorbed Probe Molecules. *Catal. Today* **1996**, *27*, 353–376.
- (89) Katada, N.; Suzuki, K.; Noda, T.; Sastre, G.; Niwa, M. Correlation Between Brønsted Acid Strength and Local Structure in Zeolites. *J. Phys. Chem. C* **2009**, *113*, 19208–19217.
- (90) Parrillo, D. J.; Gorte, R. J. Characterization of Acidity in H-ZSM-5, H-ZSM-12, H-Mordenite, and H-Y Using Microcalorimetry. *J. Phys. Chem.* **1993**, *97*, 8786–8792.
- (91) Gorte, R. J. What Do We Know About the Acidity of Solid Acids? *Catalysis Letters* **1999**, *62*, 1–13.
- (92) Gorte, R. Design Parameters for Temperature Programmed Desorption from Porous Catalysts. *J. Catal.* **1982**, *75*, 164–174.
- (93) Demmin, R.; Gorte, R. J. Design Parameters for Temperature-programmed Desorption from a Packed Bed. *J. Catal.* **1984**, *90*, 32–39.
- (94) Ilias, S.; Bhan, A. Mechanism of the Catalytic Conversion of Methanol to Hydrocarbons. *ACS Catal.* **2013**, *3*, 18–31.
- (95) Olsbye, U.; Svelle, S.; Bjørgen, M.; Beato, P.; Janssens, T. V. W.; Joensen, F.; Bordiga, S.; Lillerud, K. P. Conversion of Methanol to Hydrocarbons: How Zeolite Cavity and Pore Size Controls Product Selectivity. *Angew. Chem. Int. Ed. Engl.* **2012**, *51*, 5810–5831.

- (96) Kang, J. H.; Alshafei, F. H.; Zones, S. I.; Davis, M. E. Cage-defining Ring: A Molecular Sieve Structural Indicator for Light Olefin Product Distribution from the Methanol-to-Olefins Reaction. *ACS Catal.* **2019**.
- (97) Liu, Y.; Kirchberger, F. M.; Müller, S.; Eder, M.; Tonigold, M.; Sanchez-Sanchez, M.; Lercher, J. A. Critical Role of Formaldehyde During Methanol Conversion to Hydrocarbons. *Nat. Commun.* **2019**, *10*, 1462.
- (98) Bollini, P.; Bhan, A. Improving HSAPO-34 Methanol-to-Olefin Turnover Capacity by Seeding the Hydrocarbon Pool. *ChemPhysChem* **2018**, *19*, 479–483.
- (99) Liu, Y.; Müller, S.; Berger, D.; Jelic, J.; Reuter, K.; Tonigold, M.; Sanchez-Sanchez, M.; Lercher, J. A. Formation Mechanism of the First Carbon-Carbon Bond and the First Olefin in the Methanol Conversion into Hydrocarbons. *Angew. Chem. Int. Ed. Engl.* **2016**, *55*, 5723–5726.
- (100) Derouane, E.; Nagy, J.; Dejaifve, P.; van Hooff, J. H. C.; Spekman, B. P.; Védrine, J. C.; Naccache, C. Elucidation of the Mechanism of Conversion of Methanol and Ethanol to Hydrocarbons on a New Type of Synthetic Zeolite. *J. Catal.* **1978**, *53*, 40–55.
- (101) Ghorbanpour, A.; Rimer, J. D.; Grabow, L. C. Computational Assessment of the Dominant Factors Governing the Mechanism of Methanol Dehydration over H-ZSM-5 with Heterogeneous Aluminum Distribution. *ACS Catal.* **2016**, *6*, 2287–2298.
- (102) Chiang, H.; Bhan, A. Catalytic Consequences of Hydroxyl Group Location on the Rate and Mechanism of Parallel Dehydration Reactions of Ethanol over Acidic Zeolites. *J. Catal.* **2010**, *271*, 251–261.
- (103) Zhi, Y.; Shi, H.; Mu, L.; Liu, Y.; Mei, D.; Camaioni, D. M.; Lercher, J. A. Dehydration Pathways of 1-Propanol on HZSM-5 in the Presence and Absence of Water. *J. Am. Chem. Soc.* **2015**, *137*, 15781–15794.
- (104) Macht, J.; Janik, M. J.; Neurock, M.; Iglesia, E. Mechanistic Consequences of Composition in Acid Catalysis by Polyoxometalate Keggin Clusters. *J. Am. Chem. Soc.* **2008**, *130*, 10369–10379.
- (105) Dusselier, M.; Schmidt, J. E.; Moulton, R.; Haymore, B.; Hellums, M.; Davis, M. E. Influence of Organic Structure Directing Agent Isomer Distribution on the Synthesis of SSZ-39. *Chem. Mater.* **2015**, *27*, 2695–2702.
- (106) Albarracín-Caballero, J. D.; Khurana, I.; Di Iorio, J. R.; Shih, A. J.; Schmidt, J. E.; Dusselier, M.; Davis, M. E.; Yezerets, A.; Miller, J. T.; Ribeiro, F. H.; et al. Structural and Kinetic Changes to Small-pore Cu-zeolites after Hydrothermal Aging Treatments and Selective Catalytic Reduction of NO_x with Ammonia. *React. Chem. Eng.* **2017**, *2*, 168–179.

- (107) Shibata, S.; Itakura, M.; Ide, Y.; Sadakane, M.; Sano, T. FAU–LEV Interzeolite Conversion in Fluoride Media. *Micropor. Mesopor. Mat.* **2011**, *138*, 32–39.
- (108) Jo, D.; Ryu, T.; Park, G. T.; Kim, P. S.; Kim, C. H.; Nam, I.-S.; Hong, S. B. Synthesis of High-Silica LTA and UFI Zeolites and NH₃ –SCR Performance of Their Copper-Exchanged Form. *ACS Catal.* **2016**, *6*, 2443–2447.
- (109) Baerlocher, C.; McCusker, L. B. Database of Zeolite Structures: <http://www.iza-structure.org/databases>. <http://www.iza-structure.org/databases> (accessed Jan 5, 2017).
- (110) Cybulskis, V. J.; Harris, J. W.; Zvinevich, Y.; Ribeiro, F. H.; Gounder, R. A Transmission Infrared Cell Design for Temperature-controlled Adsorption and Reactivity Studies on Heterogeneous Catalysts. *Rev. Sci. Instrum.* **2016**, *87*, 103101.
- (111) Kresse, G.; Furthmüller, J. Efficiency of Ab-initio Total Energy Calculations for Metals and Semiconductors Using a Plane-wave Basis Set. *Comp. Mater. Sci.* **1996**, *6*, 15–50.
- (112) Kresse, G.; Furthmüller, J. Efficient Iterative Schemes for Ab Initio Total-energy Calculations Using a Plane-wave Basis Set. *Phys. Rev. B, Condens. Matter* **1996**, *54*, 11169–11186.
- (113) Kresse, G.; Hafner, J. Ab Initio Molecular-dynamics Simulation of the Liquid-metal-amorphous-semiconductor Transition in Germanium. *Phys. Rev. B, Condens. Matter* **1994**, *49*, 14251–14269.
- (114) Kresse, G.; Hafner, J. Ab Initio Molecular Dynamics for Liquid Metals. *Phys. Rev. B* **1993**, *47*, 558–561.
- (115) Blöchl, P. E. Projector Augmented-wave Method. *Phys. Rev. B, Condens. Matter* **1994**, *50*, 17953–17979.
- (116) Kresse, G.; Joubert, D. From Ultrasoft Pseudopotentials to the Projector Augmented-wave Method. *Phys. Rev. B* **1999**, *59*, 1758–1775.
- (117) Hammer, B.; Hansen, L. B.; Nørskov, J. K. Improved Adsorption Energetics Within Density-functional Theory Using Revised Perdew-Burke-Ernzerhof Functionals. *Phys. Rev. B* **1999**, *59*, 7413–7421.
- (118) Lee, J.-H.; Park, J.-H.; Soon, A. Assessing the Influence of van Der Waals Corrected Exchange-correlation Functionals on the Anisotropic Mechanical Properties of Coinage Metals. *Phys. Rev. B* **2016**, *94*, 024108.

- (119) Wellendorff, J.; Lundgaard, K. T.; Møgelhøj, A.; Petzold, V.; Landis, D. D.; Nørskov, J. K.; Bligaard, T.; Jacobsen, K. W. Density Functionals for Surface Science: Exchange-correlation Model Development with Bayesian Error Estimation. *Phys. Rev. B* **2012**, *85*, 235149.
- (120) Brogaard, R. Y.; Moses, P. G.; Nørskov, J. K. Modeling van Der Waals Interactions in Zeolites with Periodic DFT: Physisorption of n-Alkanes in ZSM-22. *Catal. Lett.* **2012**, *142*, 1057–1060.
- (121) Perdew, J. P.; Burke, K.; Ernzerhof, M. Generalized Gradient Approximation Made Simple. *Phys. Rev. Lett.* **1996**, *77*, 3865–3868.
- (122) Baerlocher, C.; McCusker, L. B. Database of Zeolite Structures <http://www.iza-structure.org/>.
- (123) Mirth, G.; Lercher, J. A.; Anderson, M. W.; Klinowski, J. Adsorption Complexes of Methanol on Zeolite ZSM-5. *Faraday Trans.* **1990**, *86*, 3039.
- (124) Ryder, J. A.; Chakraborty, A. K.; Bell, A. T. Density Functional Theory Study of Proton Mobility in Zeolites: Proton Migration and Hydrogen Exchange in ZSM-5. *J. Phys. Chem. B* **2000**, *104*, 6998–7011.
- (125) Farberow, C. A.; Dumesic, J. A.; Mavrikakis, M. Density Functional Theory Calculations and Analysis of Reaction Pathways for Reduction of Nitric Oxide by Hydrogen on Pt(111). *ACS Catal.* **2014**, *4*, 3307–3319.
- (126) Deshlahra, P.; Carr, R. T.; Iglesia, E. Ionic and Covalent Stabilization of Intermediates and Transition States in Catalysis by Solid Acids. *J. Am. Chem. Soc.* **2014**, *136*, 15229–15247.
- (127) Deshlahra, P.; Carr, R. T.; Chai, S.-H.; Iglesia, E. Mechanistic Details and Reactivity Descriptors in Oxidation and Acid Catalysis of Methanol. *ACS Catal.* **2015**, *5*, 666–682.
- (128) DeLuca, M.; Kravchenko, P.; Hoffman, A.; Hibbitts, D. Mechanism and Kinetics of Methylating C₆–C₁₂ Methylbenzenes with Methanol and Dimethyl Ether in H-MFI Zeolites. *ACS Catal.* **2019**, *9*, 6444–6460.
- (129) Löwenstein, W. The Distribution of Aluminum in the Tetrahedra of Silicates and Aluminates. *Am. Mineral* **1954**, *39*, 92–96.
- (130) Hill, I.; Malek, A.; Bhan, A. Kinetics and Mechanism of Benzene, Toluene, and Xylene Methylation over H-MFI. *ACS Catal.* **2013**, *3*, 1992–2001.
- (131) Sarazen, M. L.; Iglesia, E. Stability of Bound Species During Alkene Reactions on Solid Acids. *Proc. Natl. Acad. Sci. USA* **2017**, *114*, E3900–E3908.

- (132) Baerlocher, C.; McCusker, L. B.; Olson, D. H. *Atlas of Zeolite Framework Types*; 6th ed.; Elsevier, 2007.
- (133) Borghard, W. S.; Reischman, P. T.; Sheppard, E. W. Argon Sorption in ZSM-5. *J. Catal.* **1993**, 139, 19–23.
- (134) Wilke, T. J.; Barreau, M. A. Cation Exchange Effects on Methanol Oxidation and Dehydration by Supported Polyoxometalates. *J. Catal.* **2019**, 371, 357–367.
- (135) Rangarajan, S.; Kaminski, T.; Wyk, E. V.; Bhan, A.; Daoutidis, P. Network Generation and Analysis of Complex Biomass Conversion Systems. In *21st european symposium on computer aided process engineering; Computer aided chemical engineering*; Elsevier, 2011; Vol. 29, pp. 1743–1747.
- (136) Rangarajan, S.; Bhan, A.; Daoutidis, P. Rule-Based Generation of Thermochemical Routes to Biomass Conversion. *Ind Eng Chem Res* **2010**, 49, 10459–10470.
- (137) Alonso, D. M.; Bond, J. Q.; Dumesic, J. A. Catalytic Conversion of Biomass to Biofuels. *Green Chem.* **2010**, 12, 1493.
- (138) Climent, M. J.; Corma, A.; Iborra, S. Conversion of Biomass Platform Molecules into Fuel Additives and Liquid Hydrocarbon Fuels. *Green Chem.* **2014**, 16, 516.
- (139) Sun, D.; Yamada, Y.; Sato, S.; Ueda, W. Glycerol Hydrogenolysis into Useful C3 Chemicals. *Appl. Catal. B* **2016**, 193, 75–92.
- (140) Quispe, C. A. G.; Coronado, C. J. R.; Carvalho Jr., J. A. Glycerol: Production, Consumption, Prices, Characterization and New Trends in Combustion. *Renewable and Sustainable Energy Reviews* **2013**, 27, 475–493.
- (141) Corma, A.; Iborra, S.; Velty, A. Chemical Routes for the Transformation of Biomass into Chemicals. *Chem. Rev.* **2007**, 107, 2411–2502.
- (142) Patwardhan, P. R.; Brown, R. C.; Shanks, B. H. Understanding the Fast Pyrolysis of Lignin. *ChemSusChem* **2011**, 4, 1629–1636.
- (143) Bu, Q.; Lei, H.; Zacher, A. H.; Wang, L.; Ren, S.; Liang, J.; Wei, Y.; Liu, Y.; Tang, J.; Zhang, Q.; et al. A Review of Catalytic Hydrodeoxygenation of Lignin-derived Phenols from Biomass Pyrolysis. *Bioresour. Technol.* **2012**, 124, 470–477.
- (144) Tret'yakov, V. F.; Lermontov, A. S.; Makarfi, Y. I.; Yakimova, M. S.; Frantsuzova, N. A.; Koval, L. M.; Erofeev, V. I. Synthesis of Motor Fuels from Bioethanol. *Chem. Technol. Fuels Oils* **2008**, 44, 409–414.

- (145) Nakagawa, Y.; Tamura, M.; Tomishige, K. Perspective on Catalyst Development for Glycerol Reduction to C₃ Chemicals with Molecular Hydrogen. *Res. Chem. Intermed.* **2018**, *44*, 3879–3903.
- (146) Meher, L.; Vidyasagar, D.; Naik, S. Technical Aspects of Biodiesel Production by Transesterification—a Review. *Renewable and Sustainable Energy Reviews* **2006**, *10*, 248–268.
- (147) Soares, R. R.; Simonetti, D. A.; Dumesic, J. A. Glycerol as a Source for Fuels and Chemicals by Low-Temperature Catalytic Processing. *Angew. Chem. Int. Ed. Engl.* **2006**, *118*, 4086–4089.
- (148) Kunkes, E. L.; Simonetti, D. A.; Dumesic, J. A.; Pyrz, W. D.; Murillo, L. E.; Chen, J. G.; Buttrey, D. J. The Role of Rhenium in the Conversion of Glycerol to Synthesis Gas over Carbon Supported Platinum–rhenium Catalysts. *J. Catal.* **2008**, *260*, 164–177.
- (149) Tanksale, A.; Beltramini, J.; Dumesic, J.; Lu, G. Effect of Pt and Pd Promoter on Ni Supported catalysts—A TPR/TPO/TPD and Microcalorimetry Study. *J. Catal.* **2008**, *258*, 366–377.
- (150) BONDIOLI. From Oilseeds to Industrial Products: Present and Near Future of Oleo- Chemistry.
- (151) Pagliaro, M.; Ciriminna, R.; Kimura, H.; Rossi, M.; Della Pina, C. Recent Advances in the Conversion of Bioglycerol into Value-added Products. *Eur. J. Lipid Sci. Technol.* **2009**, *111*, 788–799.
- (152) Maris, E.; Ketchie, W.; Murayama, M.; Davis, R. Glycerol Hydrogenolysis on Carbon-supported PtRu and AuRu Bimetallic Catalysts. *J. Catal.* **2007**, *251*, 281–294.
- (153) Ten Dam, J.; Hanefeld, U. Renewable Chemicals: Dehydroxylation of Glycerol and Polyols. *ChemSusChem* **2011**, *4*, 1017–1034.
- (154) Katryniok, B.; Paul, S.; Dumeignil, F. Recent Developments in the Field of Catalytic Dehydration of Glycerol to Acrolein. *ACS Catal.* **2013**, *3*, 1819–1834.
- (155) Neurock, M.; Tao, Z.; Chemburkar, A.; Hibbitts, D. D.; Iglesia, E. Theoretical Insights into the Sites and Mechanisms for Base Catalyzed Esterification and Aldol Condensation Reactions over Cu. *Faraday Discuss* **2017**, *197*, 59–86.
- (156) Wang, Z.; Wang, L.; Jiang, Y.; Hunger, M.; Huang, J. Cooperativity of Brønsted and Lewis Acid Sites on Zeolite for Glycerol Dehydration. *ACS Catal.* **2014**, *4*, 1144–1147.

- (157) Falcone, D. D.; Hack, J. H.; Klyushin, A. Y.; Knop-Gericke, A.; Schlögl, R.; Davis, R. J. Evidence for the Bifunctional Nature of Pt–Re Catalysts for Selective Glycerol Hydrogenolysis. *ACS Catal.* **2015**, *5*, 5679–5695.
- (158) Nakagawa, Y.; Shinmi, Y.; Koso, S.; Tomishige, K. Direct Hydrogenolysis of Glycerol into 1,3-propanediol over Rhenium-modified Iridium Catalyst. *J. Catal.* **2010**, *272*, 191–194.
- (159) Tamura, M.; Amada, Y.; Liu, S.; Yuan, Z.; Nakagawa, Y.; Tomishige, K. Promoting Effect of Ru on Ir-ReO_x/SiO₂ Catalyst in Hydrogenolysis of Glycerol. *J. Mol. Catal. A: Chem* **2014**, *388-389*, 177–187.
- (160) Amada, Y.; Koso, S.; Nakagawa, Y.; Tomishige, K. Hydrogenolysis of 1,2-propanediol for the Production of Biopropanols from Glycerol. *ChemSusChem* **2010**, *3*, 728–736.
- (161) Huber, G. W.; Shabaker, J. W.; Evans, S. T.; Dumesic, J. A. Aqueous-phase Reforming of Ethylene Glycol over Supported Pt and Pd Bimetallic Catalysts. *Appl. Catal. B* **2006**, *62*, 226–235.
- (162) Chia, M.; O'Neill, B. J.; Alamillo, R.; Dietrich, P. J.; Ribeiro, F. H.; Miller, J. T.; Dumesic, J. A. Bimetallic RhRe/C Catalysts for the Production of Biomass-derived Chemicals. *J. Catal.* **2013**, *308*, 226–236.
- (163) Daniel, O. M.; DeLaRiva, A.; Kunkes, E. L.; Datye, A. K.; Dumesic, J. A.; Davis, R. J. X-ray Absorption Spectroscopy of Bimetallic Pt-Re Catalysts for Hydrogenolysis of Glycerol to Propanediols. *ChemCatChem* **2010**, *2*, 1107–1114.
- (164) Salazar, J. B.; Falcone, D. D.; Pham, H. N.; Datye, A. K.; Passos, F. B.; Davis, R. J. Selective Production of 1,2-propanediol by Hydrogenolysis of Glycerol over Bimetallic Ru–Cu Nanoparticles Supported on TiO₂. *Applied Catalysis A: General* **2014**, *482*, 137–144.
- (165) Montassier, C.; Ménézo, J. C.; Hoang, L. C.; Renaud, C.; Barbier, J. Aqueous Polyol Conversions on Ruthenium and on Sulfur-modified Ruthenium. *Journal of Molecular Catalysis* **1991**, *70*, 99–110.
- (166) Feng, J.; Wang, J.; Zhou, Y.; Fu, H.; Chen, H.; Li, X. Effect of Base Additives on the Selective Hydrogenolysis of Glycerol over Ru/TiO₂ Catalyst. *Chem. Lett.* **2007**, *36*, 1274–1275.
- (167) Nakagawa, Y.; Tomishige, K. Heterogeneous Catalysis of the Glycerol Hydrogenolysis. *Catal. Sci. Technol.* **2011**, *1*, 179.
- (168) Sato, S.; Akiyama, M.; Inui, K.; Yokota, M. Selective Conversion of Glycerol into 1,2-Propanediol at Ambient Hydrogen Pressure. *Chem. Lett.* **2009**, *38*, 560–561.

- (169) Akiyama, M.; Sato, S.; Takahashi, R.; Inui, K.; Yokota, M. Dehydration–hydrogenation of Glycerol into 1,2-propanediol at Ambient Hydrogen Pressure. *Applied Catalysis A: General* **2009**, *371*, 60–66.
- (170) Sato, S.; Sakai, D.; Sato, F.; Yamada, Y. Vapor-phase Dehydration of Glycerol into Hydroxyacetone over Silver Catalyst. *Chem. Lett.* **2012**, *41*, 965–966.
- (171) Sun, D.; Yamada, Y.; Sato, S. Effect of Ag Loading on Cu/Al₂O₃ Catalyst in the Production of 1,2-propanediol from Glycerol. *Applied Catalysis A: General* **2014**, *475*, 63–68.
- (172) Alhanash, A.; Kozhevnikova, E. F.; Kozhevnikov, I. V. Gas-phase Dehydration of Glycerol to Acrolein Catalysed by Caesium Heteropoly Salt. *Applied Catalysis A: General* **2010**, *378*, 11–18.
- (173) Nakaji, Y.; Nakagawa, Y.; Tamura, M.; Tomishige, K. Regioselective Hydrogenolysis of Alga-derived Squalane over Silica-supported Ruthenium-vanadium Catalyst. *Fuel Processing Technology* **2018**, *176*, 249–257.
- (174) Kandoi, S.; Greeley, J.; Simonetti, D.; Shabaker, J.; Dumesic, J. A.; Mavrikakis, M. Reaction Kinetics of Ethylene Glycol Reforming over Platinum in the Vapor Versus Aqueous Phases. *J. Phys. Chem. C* **2011**, *115*, 961–971.
- (175) Prati, L.; Villa, A.; Campione, C.; Spontoni, P. Effect of Gold Addition on Pt and Pd Catalysts in Liquid Phase Oxidations. *Top. Catal.* **2007**, *44*, 319–324.
- (176) Nakagawa, Y.; Tazawa, S.; Wang, T.; Tamura, M.; Hiyoshi, N.; Okumura, K.; Tomishige, K. Mechanistic Study of Hydrogen-Driven Deoxydehydration over Ceria-Supported Rhenium Catalyst Promoted by Au Nanoparticles. *ACS Catal.* **2018**, *8*, 584–595.
- (177) Hirasawa, S.; Nakagawa, Y.; Tomishige, K. Selective Oxidation of Glycerol to Dihydroxyacetone over a Pd–Ag Catalyst. *Catal. Sci. Technol.* **2012**, *2*, 1150.
- (178) Tazawa, S.; Ota, N.; Tamura, M.; Nakagawa, Y.; Okumura, K.; Tomishige, K. Deoxydehydration with Molecular Hydrogen over Ceria-Supported Rhenium Catalyst with Gold Promoter. *ACS Catal.* **2016**, *6*, 6393–6397.
- (179) Ferrin, P.; Simonetti, D.; Kandoi, S.; Kunkes, E.; Dumesic, J. A.; Nørskov, J. K.; Mavrikakis, M. Modeling Ethanol Decomposition on Transition Metals: a Combined Application of Scaling and Brønsted-Evans-Polanyi Relations. *J. Am. Chem. Soc.* **2009**, *131*, 5809–5815.
- (180) Alcala, R. DFT Studies for Cleavage of C-C and C-O Bonds in Surface Species Derived from Ethanol on Pt(111). *J. Catal.* **2003**, *218*, 178–190.

- (181) Alharbi, W.; Brown, E.; Kozhevnikova, E. F.; Kozhevnikov, I. V. Dehydration of Ethanol over Heteropoly Acid Catalysts in the Gas Phase. *J. Catal.* **2014**, *319*, 174–181.
- (182) Tamura, M.; Tokonami, K.; Nakagawa, Y.; Tomishige, K. ChemInform Abstract: Rapid Synthesis of Unsaturated Alcohols Under Mild Conditions by Highly Selective Hydrogenation. *ChemInform* **2013**, *44*, no–no.
- (183) Granger, P.; Parvulescu, V. I. Catalytic NO(x) Abatement Systems for Mobile Sources: From Three-way to Lean Burn After-treatment Technologies. *Chem. Rev.* **2011**, *111*, 3155–3207.
- (184) Kaspar, J.; Deleitenburg, C.; Fornasiero, P.; Trovarelli, A.; Graziani, M. NO Reduction by CO over Rh/Al₂O₃. Effects of Rhodium Dispersion on the Catalytic Properties. *J. Catal.* **1994**, *146*, 136–143.
- (185) Shelef, M.; Graham, G. W. Why Rhodium in Automotive Three-Way Catalysts? *Catalysis Reviews* **1994**, *36*, 433–457.
- (186) Zhdanov, V. P.; Kasemo, B. Mechanism and Kinetics of the NO + CO Reaction on Rh. *Surf. Sci. Rep.* **1997**, *29*, 31–90.
- (187) Environmental Protection Agency.
- (188) Much of the Early R&D on Automotive Catalysts, Prior to Commercialization in the 1975 Time Frame, Was Devoted To.
- (189) Shelef, M.; McCabe, R. W. Twenty-five Years after Introduction of Automotive Catalysts: What Next? *Catal. Today* **2000**, *62*, 35–50.
- (190) Srinivasan, A.; Depcik, C. Review of Chemical Reactions in the NO Reduction by CO on Rhodium/alumina Catalysts. *Catalysis Reviews* **2010**, *52*, 462–493.
- (191) Hendrickx, H. A. C. M.; Nieuwenhuys, B. E. Surface Structure Effects in the Adsorption and Desorption of Nitric Oxide on Rhodium. *Surf Sci* **1986**, *175*, 185–196.
- (192) Loffreda, D. Structure Sensitivity for NO Dissociation on Palladium and Rhodium Surfaces. *J. Catal.* **2003**, *213*, 211–225.
- (193) Mavrikakis, M.; Bäumer, M.; Freund, H. J.; Nørskov, J. K. Structure Sensitivity of CO Dissociation on Rh Surfaces. *Catalysis Letters*.
- (194) Oh, S. Comparative Kinetic Studies of CO₂ + O₂ and CO₂ + NO Reactions over Single Crystal and Supported Rhodium Catalysts. *J. Catal.* **1986**, *100*, 360–376.

- (195) Root, T. W.; Fisher, G. B.; Schmidt, L. D. Electron Energy Loss Characterization of NO on Rh(111). I. NO Coordination and Dissociation. *J. Chem. Phys.* **1986**, *85*, 4679–4686.
- (196) Root, T. W.; Schmidt, L. D.; Fisher, G. B. Adsorption and Reaction of Nitric Oxide and Oxygen on Rh(111). *Surf Sci* **1983**, *134*, 30–45.
- (197) Serna, P.; Gates, B. C. Zeolite-supported Rhodium Complexes and Clusters: Switching Catalytic Selectivity by Controlling Structures of Essentially Molecular Species. *J. Am. Chem. Soc.* **2011**, *133*, 4714–4717.
- (198) Evans, J.; Tromp, M. Interaction of Small Gas Phase Molecules with Alumina Supported Rhodium Nanoparticles: An *in Situ* Spectroscopic Study. *J. Phys.: Condens. Matter* **2008**, *20*, 184020.
- (199) Newton, M. A. Applying Dynamic and Synchronous DRIFTS/EXAFS to the Structural Reactive Behaviour of Dilute (≤ 1 wt%) Supported Rh/Al₂O₃ Catalysts Using Quick and Energy Dispersive EXAFS. *Top. Catal.* **2009**, *52*, 1410–1424.
- (200) Newton, M. A.; Dent, A. J.; Fiddy, S. G.; Jyoti, B.; Evans, J. Particle Size Effects in Rh/Al₂O₃ Catalysts as Viewed from a Structural, Functional, and Reactive Perspective: The Case of the Reactive Adsorption of NO. *J. Mater. Sci.* **2007**, *42*, 3288–3298.
- (201) Newton, M. A.; Jyoti, B.; Dent, A. J.; Fiddy, S. G.; Evans, J. Synchronous, Time Resolved, Diffuse Reflectance FT-IR, Energy Dispersive EXAFS (EDE) and Mass Spectrometric Investigation of the Behaviour of Rh Catalysts During NO Reduction by CO. *Chem. Commun.* **2004**, 2382–2383.
- (202) Kondarides, D. I.; Chafik, T.; Verykios, X. E. Catalytic Reduction of NO by CO over Rhodium Catalysts. *J. Catal.* **2000**, *191*, 147–164.
- (203) Getsoian, A. “Bean; Das, U.; Camacho-Bunquin, J.; Zhang, G.; Gallagher, J. R.; Hu, B.; Cheah, S.; Schaidle, J. A.; Ruddy, D. A.; Hensley, J. E.; et al. Organometallic Model Complexes Elucidate the Active Gallium Species in Alkane Dehydrogenation Catalysts Based on Ligand Effects in Ga K-edge XANES. *Catal. Sci. Technol.* **2016**, *6*, 6339–6353.
- (204) Getsoian, A. B.; Zhai, Z.; Bell, A. T. Band-gap Energy as a Descriptor of Catalytic Activity for Propene Oxidation over Mixed Metal Oxide Catalysts. *J. Am. Chem. Soc.* **2014**, *136*, 13684–13697.
- (205) Hu, B.; Bean“ Getsoian, A.; Schweitzer, N. M.; Das, U.; Kim, H.; Niklas, J.; Poluektov, O.; Curtiss, L. A.; Stair, P. C.; Miller, J. T.; et al. Selective Propane Dehydrogenation with Single-site Coll on SiO₂ by a Non-redox Mechanism. *J. Catal.* **2015**, *322*, 24–37.

- (206) Getsoian, A. G. B.; Hu, B.; Miller, J. T.; Hock, A. S. Silica-Supported, Single-Site Sc and Y Alkyls for Catalytic Hydrogenation of Propylene. *Organometallics* **2017**, *36*, 3677–3685.
- (207) Kumar, A.; Medhekar, V.; Harold, M. P.; Balakotaiah, V. NO Decomposition and Reduction on Pt/Al₂O₃ Powder and Monolith Catalysts Using the TAP Reactor. *Appl. Catal. B* **2009**, *90*, 642–651.
- (208) Hecker, W. Reduction of NO by H₂ over Silica-supported Rhodium: Infrared and Kinetic Studies. *J. Catal.* **1985**, *92*, 247–259.
- (209) Frank, B.; Emig, G.; Renken, A. Kinetics and Mechanism of the Reduction of Nitric Oxides by H₂ Under Lean-burn Conditions on a Pt–Mo–Co/α-Al₂O₃ Catalyst. *Appl. Catal. B* **1998**, *19*, 45–57.
- (210) Dhainaut, F.; Pietrzyk, S.; Granger, P. Kinetics of the NO/H₂ Reaction on Pt/LaCoO₃: A Combined Theoretical and Experimental Study. *J. Catal.* **2008**, *258*, 296–305.
- (211) Dhainaut, F.; Pietrzyk, S.; Granger, P. Kinetic Investigation of the NO Reduction by H₂ over Noble Metal Based Catalysts. *Catal. Today* **2007**, *119*, 94–99.
- (212) Dhainaut, F.; Pietrzyk, S.; Granger, P. Kinetics of the NO+H₂ Reaction over Supported Noble Metal Based Catalysts: Support Effect on Their Adsorption Properties. *Appl. Catal. B* **2007**, *70*, 100–110.
- (213) Shestov; Burch; Sullivan. A Transient Kinetic Study of the Mechanism of the NOCH₂ Reaction over Pt/SiO₂ Catalysts.
- (214) Burch, R.; Millington, P. J.; Walker, A. P. Mechanism of the Selective Reduction of Nitrogen Monoxide on Platinum-based Catalysts in the Presence of Excess Oxygen. *Appl. Catal. B* **1994**, *4*, 65–94.
- (215) Nieuwenhuys, B. E. The Surface Science Approach Toward Understanding Automotive Exhaust Conversion Catalysis at the Atomic Level. In: *Advances in Catalysis*; Elsevier, 1999; Vol. 44, pp. 259–328.
- (216) Hirano, H.; Yamada, T.; Tanaka, K. I.; Siera, J.; Nieuwenhuys, B. E. The Reduction of Nitric Oxide by Hydrogen Over Pt, Rh and Pt-Rh Single Crystal Surfaces. In *New Frontiers in Catalysis - Proceedings of the 10th International Congress on Catalysis, Budapest, 19-24 July 1992*; Studies in surface science and catalysis; Elsevier, 1993; Vol. 75, pp. 345–357.
- (217) Hirano, H.; Yamada, T.; Tanaka, K. I.; Siera, J.; Cobden, P.; Nieuwenhuys, B. E. Mechanisms of the Various Nitric Oxide Reduction Reactions on a Platinum-rhodium (100) Alloy Single Crystal Surface. *Surf Sci* **1992**, *262*, 97–112.

- (218) de Wolf, C. A.; Nieuwenhuys, B. E. Oscillatory Behaviour in the NO–hydrogen Reactions over Pt-group Metal Surfaces. *Catal. Today* **2001**, *70*, 287–300.
- (219) Hibbitts, D. D.; Jiménez, R.; Yoshimura, M.; Weiss, B.; Iglesia, E. Catalytic NO Activation and NO–H₂ Reaction Pathways. *J. Catal.* **2014**, *319*, 95–109.
- (220) Kondarides, D. I.; Chafik, T.; Verykios, X. E. Catalytic Reduction of NO by CO over Rhodium Catalysts. *J. Catal.* **2000**, *193*, 303–307.
- (221) Loschen, C.; Carrasco, J.; Neyman, K. M.; Illas, F. First-principlesandstudy of Cerium Oxides: Dependence on the Effective U Parameter. *Phys. Rev. B* **2007**, *75*, 035115.
- (222) Mino, L.; Ferrari, A. M.; Lacivita, V.; Spoto, G.; Bordiga, S.; Zecchina, A. CO Adsorption on Anatase Nanocrystals: A Combined Experimental and Periodic DFT Study. *J. Phys. Chem. C* **2011**, *115*, 7694–7700.
- (223) Mino, L.; Spoto, G.; Bordiga, S.; Zecchina, A. Particles Morphology and Surface Properties as Investigated by HRTEM, FTIR, and Periodic DFT Calculations: From Pyrogenic TiO₂ (P25) to Nanoanatase. *J. Phys. Chem. C* **2012**, *116*, 17008–17018.
- (224) Qi, J.; Christopher, P. Atomically Dispersed Rh Active Sites on Oxide Supports with Controlled Acidity for Gas-Phase Halide-Free Methanol Carbonylation to Acetic Acid. *Ind Eng Chem Res* **2019**, *58*, 12632–12641.
- (225) Nolan, M.; Grigoleit, S.; Sayle, D. C.; Parker, S. C.; Watson, G. W. Density Functional Theory Studies of the Structure and Electronic Structure of Pure and Defective Low Index Surfaces of Ceria. *Surf Sci* **2005**, *576*, 217–229.
- (226) Raybaud, P.; Digne, M.; Iftimie, R.; Wellens, W.; Euzen, P.; Toulhoat, H. Morphology and Surface Properties of Boehmite (γ -AlOOH): A Density Functional Theory Study. *J. Catal.* **2001**, *201*, 236–246.

BIOGRAPHICAL SKETCH

Steven Nystrom became a ‘Gator’ at a young age while he attended his elementary school, the Avery Alligators. Through middle school and high school his interests in the environment and energy flourished culminating in his decision to become a chemical engineer. Being inspired by both his grand-mother and mom who attended The Ohio State University, he applied and became a buckeye himself. His yearned for understanding the fundamental forces of the universe lead to him minoring in physics, specializing in polymers, and starting undergraduate research under James Coe. Wanting to prod further into the workings of the world he decided to get his PhD at the University of Florida. There he began work in a brand-new lab under Dr. David Hibbitts, where he spent 5 years performing computational chemistry and experimental working attempting to elucidate several processes in energy production. Now the world is his oyster.